ATOMISTIC INSIGHTS INTO SURFACE REACTIVITY VIA DENSITY FUNCTIONAL THEORY

A THESIS SUBMITTED TO
THE GRADUATE SCHOOL OF NATURAL AND APPLIED SCIENCES
OF
MIDDLE EAST TECHNICAL UNIVERSITY

BY

MERVE DEMİRTAŞ

IN PARTIAL FULFILLMENT OF THE REQUIREMENTS
FOR
THE DEGREE OF DOCTOR OF PHILOSOPHY
IN
PHYSICS

SEPTEMBER 2018

Approval of the thesis:

ATOMISTIC INSIGHTS INTO SURFACE REACTIVITY VIA DENSITY FUNCTIONAL THEORY

submitted by **MERVE DEMİRTAŞ** in partial fulfillment of the requirements for the degree of **Doctor of Philosophy in Physics Department, Middle East Technical University** by,

Prof. Dr. Halil Kalıpçılar
Dean, Graduate School of **Natural and Applied Sciences**

Prof. Dr. Altuğ Özpineci
Head of Department, **Physics**

Assoc. Prof. Dr. Hande Toffoli
Supervisor, **Physics Department, METU**

Examining Committee Members:

Assoc. Prof. Dr. Engin Durgun
UNAM, Bilkent University

Assoc. Prof. Dr. Hande Toffoli
Physics Department, METU

Prof. Dr. Şenay Katırcıoğlu
Physics Department, METU

Assoc. Prof. Dr. Alpan Bek
Physics Department, METU

Assoc. Prof. Dr. Emre Taşcı
Physics Engineering Department, Hacettepe University

Date:

I hereby declare that all information in this document has been obtained and presented in accordance with academic rules and ethical conduct. I also declare that, as required by these rules and conduct, I have fully cited and referenced all material and results that are not original to this work.

Name, Last Name: MERVE DEMİRTAŞ

Signature :

ABSTRACT

ATOMISTIC INSIGHTS INTO SURFACE REACTIVITY VIA DENSITY FUNCTIONAL THEORY

Demirtaş, Merve
Ph.D., Department of Physics
Supervisor : Assoc. Prof. Dr. Hande Toffoli

September 2018, 114 pages

In this thesis, three different topics are investigated by using Density Functional Theory. First, an extensive study of the water gas shift reaction on Mo_2C surface is carried out. CO is chosen as a probe molecule in order to understand the structural and electronic effects of the metal additives on the surface. We show that preadsorbed K atom enhences the activation and adsorption of CO molecule on the surface when compared to precious metal additives we consider, which are Pt and Au. Additionally, the presence of Pt and K stabilizes the transition state of the C-O bond scission, lowers the activation energy of this reaction.

In the fourth part, the oxidation of CH_3OH molecule is examined on bare and Pt-doped Au(111) surfaces. With this aim, the adsorption energies of molecules and atoms involved in the reaction of CH_3OH dissociation to CH_3O and H in order to obtain their stable sites. Having defined them, the activation barrier calculations are carried out on the bare Au(111) surface. Additionally, the same calculations are performed on the Pt-doped Au(111) surface in different concentrations in order to see the effect of them on the activation barrier. We show that the activation barriers are notably decreased when the number of Pt dopant atoms on the surfaces increases.

In the fifth part, the interaction between the amorphous SiO_2, crystal Si, oxidized crystal Si surfaces and ions of different types of etchants, which are H,F and Cu, is examined. The interaction between ions and amorphous surface is shown to be weaker than the reconstructed bare and oxydized Si surfaces. The adsorption energies are quite high for H and F ions on the reconstructed Si(001) surface. For Cu ions, the adsorption energy is improved with precovered O atom on the Si surface.

Keywords: Density Functional Theory, Catalysis, Water Gas Shift Reaction, Adsorption Energy, Surface, Methanol, Activation Energy

ÖZ

YÜZEY REAKTİVİTESİNE YÜK YOĞUNLUĞU FONKSİYONELİ TEORİSİ İLE ATOMİSTİK BAKIŞ

Demirtaş, Merve
Doktora, Fizik Bölümü
Tez Yöneticisi : Doç. Dr. Hande Toffoli

Eylül 2018 , 114 sayfa

Bu tezde Yük Yoğunluğu Teorisi kullanılarak üç farklı konu çalışılmıştır. İlk olarak, Mo_2C yüzeyi üzerinde su gaz değişimi reaksiyonu kapsamlı bir şekilde incelenmiştir. Bu yüzeyin elektronik ve yapısal özelliklerini incelemek için CO model molekül olarak secilmiştir ve molekülün parçalanma reaksiyonu bu yüzeylere bağlanan metal katkılarda düşünülerek simule edilmiştir. Bu metal katkılardan K atomunun, CO molekülünün bağlanma enerjisini artırdığı ve aktivasyonunu kolaylaştırdığı gözlenmiştir. Ayrıca Pt ve K atomlarının CO molekülünün parçalanma reaksiyonunu sırasında, geçiş durumunda (transition state) molekülün en kararlı olduğu durumu korumasına yardımcı olmuştur.

4. bölümde, CH_3OH molekülünün oksidasyonu reaksiyonu temiz ve Pt dopantlı Au(111)

yüzeylerinde incelenmiştir. Bu amaç doğrultusunda öncelikle reaksiyona katılan atomların ve moleküllerin bağlanma enerjileri hesaplanarak en kararlı oldukları bağlanma yerleri tespit edilmiştir. Bunlar elde edildikten sonra, CH_3OH molekülünün oksidasyon reaksiyonunun aktivasyon enejisi öncelikle temiz Au(111) yüzeyi üzerinde hesaplanmıştır. Farklı sayısaki Pt atomunun dopant olarak reaksiyonun aktivasyon bariyerine nasıl etki ettiğini görmek için, aynı hesaplamalar bu yüzeylerde de hesaplanmıştır. Pt atomunun dopant olarak yüzeydeki miktarı arttıkça CH_3OH molekülünün parçalanma reaksiyonunun aktivasyon bariyerini düşürmüştür.

5. bölümde, amorf SiO_2, kristal Si ve oksitlenmiş kristal Si yüzeyleri ve aşındırıcı olan H, F ve Cu iyonlarının arasındaki etkileşim çalışılmıştır. Amorf ve aşındırıcı iyonları arasındaki etkileşim, temiz ve oksitlenmiş kristal Si yüzeylerinin etkileşimlerine göre zayıftır. H ve F iyonlarının bağlanma enerjileri temiz Si yüzeyinde oldukça fazladır. Cu iyonlarının bağlanma enerjisi Si yüzeylerine bağlanan O atomuyla artmıştır.

Anahtar Kelimeler: Yük Yoğunluğu Teorisi, Kataliz, Su Gaz Değişimi Reaksiyonu, Bağlanma Enerjisi, Metanol, Aktivasyon Enerjisi

To my family

Güner Demirtaş, Yılmaz Demirtaş, and Gökhan Alkaç

ACKNOWLEDGMENTS

I would first like to thank my supervisor, Dr. Hande Toffoli, for her endless patience and considerable support both in my thesis and my personal life. I would not be able to complete my thesis without her guidence. All her advices will always remain with me throughout my life.

I thank Mustafa, Kamil, Deniz, Özgür, Hikmet, Cihan, Tuğberk and Karaca for all the good and bad times that we have shared and all the *goygoy*s we have had. I am also grateful to Ozan, Nadire, Emel, Selma, Esin and İrem for their friendship.

I also thank my family for their endless love and unconditional support. They always encourage me regardless of my choices and ideas. Without them, I would not be the person who I am now.

Finally, but not the least, I am grateful to my dear fiance, Gökhan Alkaç, who was always with me in my every difficult time. He encouraged and motivated me when I felt hopeless. I am so appreciative for his endless love and understanding. Thank you for enriching my life with your presence. The best hearted man, I love you so much.

TABLE OF CONTENTS

ABSTRACT v

ÖZ vii

ACKNOWLEDGMENTS x

TABLE OF CONTENTS xi

LIST OF TABLES xv

LIST OF FIGURES xvii

LIST OF ABBREVIATIONS xxiii

CHAPTERS

1 INTRODUCTION 1

2 THEORETICAL BACKGROUND 5

  2.1 Solid State Systems and Their Problems 5

  2.2 Many Body Hamiltonian 5

  2.3 Born-Oppenheimer Approximation 6

    2.3.1 Hartree and Hartree-Fock Approximation 7

    2.3.2 Thomas-Fermi Theory 9

    2.3.3 Density Functional Theory 9

    2.3.4 Hohenberg-Kohn Theorems 10

2.3.5 Kohn-Sham Approach 12

2.3.5.1 Total energy in terms of density 12

2.3.6 Functionals for Exchange and Correlations 14

2.3.6.1 The Local Density Approximation . . 14

2.3.6.2 The Generalized Gradient Approximation 15

2.3.7 Kohn-Sham Equations 15

2.3.8 Periodicity and The Bloch's Theorem 16

2.3.9 Planewave Expansion and Technical Issues 17

2.3.9.1 Pseudopotential Approximation 17

2.3.9.2 Integration over K Points 19

2.3.9.3 Smearing 19

2.3.10 Adsorption Energies 20

2.3.11 Calculation of Activation Energies 21

2.3.11.1 Nudged Elastic Band Method 22

3 EFFECT OF PLATINUM, GOLD, AND POTASSIUM ADDITIVES ON THE SURFACE CHEMISTRY OF CDI_2-ANTITYPE MO_2C . . 25

3.1 Introduction 25

3.2 Computational Details 29

3.3 DFT Calculations 29

3.3.1 Bulk Structure 29

3.3.2 Adsorption Energies 32

3.3.2.1 Adsorption Energies of Promoters . . 32

3.3.2.2 Adsorption Energy of Atomic Adsorbates of O, C and H 35

3.3.2.3 Adsorption Energy of Molecular Adsorbates of CO, CO_2 and H_2O 39

3.3.3 Coadsorption Energies of the CO molecule with Pt, Au, K 43

3.3.4 Dissociative adsorption of CO on Mo_2C surface . 49

3.3.5 H_2 formation on Mo_2C surface with and without promoter 52

3.4 CONCLUSION 52

4 EFFECT OF THE PLATINUM AS DOPANTS ON METHANOL DEHYDROGENATION ON THE GOLD SURFACES 57

4.1 Introduction 57

4.2 Computational Details 61

4.3 DFT Calculations 61

4.3.1 Bulk Structure and the (111) Surface of the Au Crystal 61

4.3.2 Adsorption Energy Calculations 62

4.3.2.1 Adsorption Energies of the CH_3OH on the clean and Pt-doped Au (111) surface 63

4.3.2.2 Molecular adsorption on the full Pt top layer and sublayers 67

4.3.3 Coadsorption Energies 72

4.3.3.1 Coadsorption of the CH_3O, and H . . . 72

4.3.3.2 Coadsorption Energies of the CH_3O, and OH 75

4.3.3.3 Coadsorption of the CH_3OH, and O . . 78

4.4 Activation Energies 79

4.4.1 Activation Energies of the CH_3OH oxidation . . . 79

4.4.2 Activation Energies of the Dissociation of CH_3OH on O precovered surfaces 84

4.5 Conclusion 87

5 ULTRAFAST 3D LASER MICROMACHINING FOR SOLAR CELLS 89

5.1 INTRODUCTION 89

5.2 Computational and Structural Details 90

5.3 Interaction of Amorphous Surface with Etchants 92

5.4 Interaction of Si(100) Crystal Surface with Etchants 94

5.5 Interaction of Oxygenated Si(100) Crystal Surface with Etchants 95

5.6 Conclusion 96

6 CONCLUSION 99

REFERENCES 103

CURRICULUM VITAE 113

LIST OF TABLES

TABLES

Table 3.1 Lattice constants of CdI_2 antitype Mo_2C using different methods. . . 30

Table 3.2 Adsorption energies (in eV) and Bader partial charges (in $|e|$) of atomic adsorbates on the two Mo surface terminations and C termination. . 33

Table 3.3 Adsorption energies (in eV) and Bader partial charges (in $|e|$) of atomic adsorbates on the two Mo and C surface terminations. 37

Table 3.4 Adsorption energies (in eV), Bader partial charges (in $|e|$) and bond lengths of CO molecule on the two Mo and C surface terminations.Last column gives the binding energy for the CO molecule in which O atom pointing the surface 39

Table 3.5 Adsorption energies (in eV), Bader partial charges (in $|e|$) and bond lengths of CO_2 molecule on the two Mo and C surface terminations. 43

Table 3.6 Adsorption energies (in eV), Bader partial charges (in $|e|$) and bond lengths of H_2O molecule on the two Mo and C surface terminations. . . . 43

Table 3.7 Coadsorption energies (in eV) for CO molecule on the two Mo and C surface terminations with Pt atom as promoter,respectively. 45

Table 3.8 Coadsorption energies (in eV) for CO molecule on the two Mo and C surface terminations with Au atom as promoter, respectively. 47

Table 3.9 Coadsorption energies (in eV) for CO molecule on the two Mo and C surface terminations with K atom as promoter, respectively. 47

Table 4.1 Adsorption energies (in eV) of molecular adsorption of the CH_3OH on bare Au(111) and surface and Au(111) surface with different magnitude of dopant atoms of Pt. 63

Table 4.2 Adsorption energies (in eV) of molecular adsorption of the CH_3O and H atom on bare Au(111) and Au(111) surface with different concentrations of dopant atoms of Pt. 65

Table 4.3 Adsorption energies (in eV) of O atom and OH molecule on bare Au(111) and surface and Au(111) surface with different magnitude of dopant atoms of Pt. 66

Table 4.4 Adsorption energies (in eV) of the CH_3OH (the left one) and CH_3O (the right one) molecules on Au/9Pt type of slab. 68

Table 4.5 Adsorption energies (in eV) of the OH moecule (the left panel), O (the middle panel) and H (the right panel) atoms on Au/9Pt type of slab. . 70

Table 4.6 Adsorption energies (in eV) of the CH_3OH (the left one) and CH_3O (the right one) molecules on Au/sub type of slab. 70

Table 4.7 Adsorption energies (in eV) of the OH molecule (the left panel), O (the middle panel) and H (the right panel) atoms on Au/sub type of slab. . 70

Table 4.8 Coadsorption energies (in eV) of molecular adsorption of the CH_3O with H on bare Au(111) and doped surfaces. 73

Table 4.9 Coadsorption energies (in eV) of CH_3O molecule with OH molecule on bare Au(111) and doped surfaces Au(111) surfaces. 76

Table 4.10 Coadsorption energies (in eV) of CH_3OH molecule with O on bare Au(111) and doped surfaces. 78

Table 4.11 The all activation barrier results on the surfaces in eV. 81

Table 4.12 The all activation barrier results (in eV) on surfaces both with O add atoms and dopant atoms. 85

LIST OF FIGURES

FIGURES

Figure 2.1 Illustration of the oscillatory wavefunction of nucleus corresponding to blue one, and the red one represents the pseudo wavefunction which is smoother. These two coincide at the radius of rc [25]. 18

Figure 2.2 Scheme of the slab model for the adsorption. 20

Figure 2.3 Illustration of reactants, transition state and producst. 21

Figure 2.4 The left one represents the two dimensional potential energy landscape. A and B points are the local minimas and the line connected between them is MEP. The right one represents the energy profile of the MEP.[28] 22

Figure 3.1 The top panel shows the side view of the 2×2×n (where n=5,6,7) surface slabs, bottom panel corresponds to top views of the mentioned slabs with labeled their adsorption sites. Mo atoms are in blue and C atoms are in grey. 31

Figure 3.2 PDOS profiles of the 2×2× n where n is 5,6 and,7 respectively. . . 32

Figure 3.3 The first, second and third columns show the top views of Pt adsorption on different adsorption sites namely h1, h2, t and b on the 2×2× n (where n=5,6,7) surface slabs, respectively. The PDOS plotting only corresponds to most stable sites. In the figures, Mo atoms are in blue, C atoms are in grey and Pt atoms are in navy. 34

Figure 3.4 The top panel shows the top view of the 2×2× n (where n=5,6,7) surface slabs with O atom corresponding to most stable sites, and second row shows their PDOS profiles. Third row represents the top view of the H adsorption on three different terminations with their energetically favourable sites and bottommost panel gives the PDOS profiles of the H adsorption. Mo atoms are in blue, C atoms are in grey, O atoms are in red and H atoms are in turquoise. 36

Figure 3.5 The first row shows the top view of the most stable sites of the C atom adsorption on the 2×2× n (where n=5,6,7) surface slabs with their PDOS profiles given in the bottom panel. Mo atoms are in blue, C atoms are in grey. 38

Figure 3.6 The top panel shows the side top view of the 2×2× n (where n=5,6,7) surface slabs with CO molecule corresponding to stable sites, middle panel shows their top views of the mentioned slabs and the bottom panel shows the PDOS profiles. Mo atoms are in blue, C atoms are in grey, O atoms are in red. 41

Figure 3.7 The top panel shows the side of the CO_2 molecule on the 2×2× n (where n=5,6,7) surface slabs ,only considered their most stable places. Second row gives the top view of them. Bottommost one corresponds to PDOS profiles. Mo atoms are in blue, C atoms are in grey, O atoms are in red. 42

Figure 3.8 The top and middle panel show the side and top views of the H_2O adsorption on 2×2× n (where n=5,6,7) surface slabs with their most stable sites. Bottom panel corresponds to the PDOS profiles. Mo atoms are in blue, C atoms are in grey, O atoms are in red and H atoms are in turquoise. 44

Figure 3.9 First and second rows give the side and top views of the most stable adsorption sites of the CO molecule with coadsorbed Pt atom on Mo1, Mo2 and C terminated slabs, respectively. The last one shows PDOS profiles of them. Mo atoms are in blue, C atoms are in grey, O atoms are in red and Pt atoms are in navy. 46

Figure 3.10 First and second rows give the side and top views of the most stable adsorption sites of the CO molecule with coadsorbed Au atom on Mo1, Mo2 and C terminated slabs, respectively. The last one shows PDOS profiles of them. Mo atoms are in blue, C atoms are in grey, O atoms are in red and Au atoms are in yellow. 48

Figure 3.11 CO dissociation profile for bare surface and Pt promoted surface. The first and second rows are initial, transition, final states of the reaction the bare surface and PDOS profile of the reaction in transition state. The third and fourth rows are initial, transition, final states of the reaction the Pt promoted surface and PDOS profile of the reaction in transition state. Mo atoms are in blue, C atoms are in grey, O atoms are in red and Pt atoms are in navy 49

Figure 3.12 CO dissociation profile for Au and K promoted surface. The first and second rows are initial, transition, final states of the reaction Au promoted surface and PDOS profile of the reaction in transition state. The third and fourth rows are initial, transition, final states of the reaction the K promoted surface and PDOS profile of the reaction in transition state.Mo atoms are in blue, C atoms are in grey, O atoms are in red, Au atoms are in yellow and K atoms are in violet. 51

Figure 3.13 H_2-formation first and second steps without using promoter and dopands 53

Figure 3.14 H_2-formation fist and second steps with promoter 54

Figure 3.15 H_2-formation fist and second steps without using promoter and dopant 54

Figure 4.1 The side view (a) and the top view (b) of the 3x3x4 surface slab of the Au. The labels on the right figure represents the different adsorption sites on the Au surface. 62

Figure 4.2 The first row represents the side view of the adsorption of CH_3OH molecule on bare, Au/Pt, Au/2Pt and Au/3Pt surfaces. The second row shows same for ontop views. The last row represents the corresponding PDOS profiles. In the figures, Au atoms are in yellow,H atoms are in turquoise, C are in grey and O atoms are in red. 64

Figure 4.3 The first row represents the ontop views of most stable sites of the adsorption of CH_3O molecule on bare, Au/Pt, Au/2Pt and Au/3Pt surface, respectively. The second row shows the corresponding PDOS profiles for them . The third row represents the those for the H atom adsorption with most stable configurations. The last row displays the PDOS profiles for the adsorption of H . In the figures, Au atoms are in yellow, H atoms are in turquoise, C are in grey and O atoms are in red. 66

Figure 4.4 The first row represents the ontop views of most stable sites of the adsorption of O atom on bare, Au/Pt, Au/2Pt and Au/3Pt surface. The second row shows the corresponding PDOS profiles for O . The third row represents the those for the OH atom adsorption with most stable configurations. The last row displays the PDOS profiles for the adsorption of OH. In the figures, Au atoms are in yellow,H atoms are in turquoise,C are in grey and O atoms are in red. 67

Figure 4.5 The first row represents the side views of most stable sites of the adsorption of CH_3OH, CH_3O, and H with corresponding PDOS profiles given in second row. The third row shows the same for the O atom and OH molecule along with corresponding PDOS profiles given in fourth row. In the figures, Au atoms are in yellow,H atoms are in turquoise,C are in grey, Pt atoms are in navy and O atoms are in red. 69

Figure 4.6 The first row represents the side views of most stable sites of the adsorption of CH_3OH, CH_3O, and H with corresponding PDOS profiles given in second row. The third row shows the same for the O atom and OH molecule along with corresponding PDOS profiles given in fourth row. In the figures, Au atoms are in yellow,H atoms are in turquoise,C are in grey, Pt atoms are in navy and O atoms are in red. 71

Figure 4.7 The top, middle and bottom panels show the geometry optimized structures of CH_3O adsorption on the bare, Au/Pt, Au/2Pt slabs with H atom and first, second, third and fourth columns represent the H at hcp, fcc, bridge and ontop positions on the mentioned slabs, respectively. In the figures, Au atoms are in yellow,H atoms are in turquoise,C are in grey, O atoms are in red and Pt atoms are in navy. 74

Figure 4.8 The top and bottom panels show the geometry optimized structures of CH_3O adsorption on the Au/3Pt, Au/9Pt slabs with H atom and first, second, third and fourth columns represent the H at hcp, fcc, bridge and ontop positions on the mentioned slabs, respectively. In the figures, Au atoms are in yellow,H atoms are in turquoise,C are in grey, O atoms are in red and Pt atoms are in navy. 75

Figure 4.9 The first panel shows the geometry optimized structures of CH_3O adsorption on the bare, Au/Pt, Au/2Pt slabs with OH atom and second one represents the same for Au/3Pt and Au/9Pt , respectively. In the figures, Au atoms are in yellow,H atoms are in turquoise,C are in grey, O atoms are in red and Pt atoms are in navy. 77

Figure 4.10 The first panel shows the geometry optimized structures of CH_3OH adsorption on the bare, Au/Pt, Au/2Pt slabs with O atom and second one represents the same for Au/3Pt and Au/9Pt , respectively. In the figures, Au atoms are in yellow,H atoms are in turquoise,C are in grey, O atoms are in red and Pt atoms are in navy. 79

Figure 4.11 The dissociation of CH_3OH molecule to CH_3O and H on the clean Au(111) surface along with PDOS profiles of initial, transition and final configurations. In the figures, Au atoms are in yellow,H atoms are in turquoise,C are in grey and O atoms are in red. 80

Figure 4.12 The first and second rows represent the dissociation of CH_3OH molecule to CH_3O and H on the Au/Pt (111) surface along with PDOS profiles of initial, transition and final configurations. The third and fourth rows represent the those for Au/2Pt (111) surface. In the figures, Au atoms are in yellow, Pt atoms are in blue, H atoms are in turquoise, H atoms are in turquoise, C are in grey and O atoms are in red. 82

Figure 4.13 The first and second rows show the dissociation of CH_3OH molecule to CH_3O and H on the Au/3Pt (111) surface along with PDOS profiles of initial, transition and final configurations.The third and fourth rows represent the those for last layer doping of Au (111) surface. In the figures, Au atoms are in yellow, Pt atoms are in blue, H atoms are in turquoise, C are in grey and O atoms are in red. 83

Figure 4.14 The figures represent the initial, transition and final stages of the dissociation of CH_3OH on Au/sub type of slab . In these figures, Au atoms are in yellow, H atoms are in turquoise, C are in grey, Pt are in navy and O atoms are in red. 84

Figure 4.15 The figures represent the initial, transition and final stages of the dissociation of CH_3OH on Au(111) surface with the precovered O atom. In these figures, Au atoms are in yellow, H atoms are in turquoise, C are in grey and O atoms are in red. 85

Figure 4.16 The figures represent the initial, transition and final stages of the dissociation of CH_3OH on Au/Pt and Au/2Pt surfaces with the precovered O atom. In these figures, Au atoms are in yellow, H atoms are in turquoise, C are in grey and O atoms are in red. 86

Figure 4.17 The figures represent the initial, transition and final stages of the dissociation of CH_3OH on Au/3Pt surface with the precovered O atom. In these figures, Au atoms are in yellow, H atoms are in turquoise, C are in grey and O atoms are in red. 87

Figure 5.1 Lazer processing of Si films (a) and the chemichal etchant treatment (b). 90

Figure 5.2 Illustration of the amorphous silica (in a) with their pair distribution (in b). Red spheres refer to O atoms, white ones refer Si. 92

Figure 5.3 Illustration of the 010 surface of SiO_2. Red spheres refer to O atoms, white ones refer Si. 93

Figure 5.4 Illustration of the H and F ions on 010 surface of SiO_2. Red spheres refer to O atoms, white ones refer Si and blue ones refer H. 93

Figure 5.5 Illustration of the Cu on amorphous surface of SiO_2 (010). (a) represents the Cu atom on Si atom with coordination number 3, (b) represents Cu atom on Si atom with coordination number 2 and (c) represents Cu atom on top of the O atom which is located between the two Si atoms. Red spheres refer to O atoms, white ones refer Si and navy ones refer Cu. 94

Figure 5.6 llustration of the interaction between the reconstructed Si surfaces with H, and F ions. In this figure, Si atoms are light, blue H atoms are navy and F atoms are grey. 95

Figure 5.7 Illustration of the interaction between the reconstructed Si surfaces with Cu atoms. In this figure, Si atoms are light and blue Cu atoms are brown. 95

Figure 5.8 Illustration of the interaction between the reconstructed oxidized Si surfaces with H and F ions, Cu atoms. In this figure, Si atoms are light and blue Cu atoms are brown. 96

LIST OF ABBREVIATIONS

DFT	Density Functional Theory
LDA	Local Density Approximation
GGA	Generalized Gradient Approximation
NEB	Nudged Elastic Band
MEP	Minimum Energy Path
CI-NEB	Climbing Image Nudged Elastic Band
WGS	Water Gas Shift

CHAPTER 1

INTRODUCTION

In order to accurately investigate the principles behind the chemical reactions, efficient quantum mechanical models are needed. In this thesis, we use the Density Functional Theory (DFT), which is one of the most used methods in material science in the last two decades. This method gives results which are remarkably close to experimental values in both determination of adsorption energies and reaction mechanisms. Chapter 2 is devoted to the theoretical background of the DFT.

The environmental problems of carbon-based energy sources are rapidly increasing day by day. Therefore, the development of the hydrogen-based economy has many advantages because of its lower environmental impact and higher efficiency of energy conversion when used in fuel cells. The water gas shift (WGS) reaction is one of the primary reactions in industry in order to produce hydrogen. This reaction is employed in industrial applications with the usage of catalysts. However, the conditions under which industrial applications proceed are not appropriate at smaller scales, such as portable fuel cells used in transportation. An active field of research has been developed to identify materials that could be used as catalysts in small scale applications with the goal of reducing the cost, bringing down the optimal ambient temperature and obtaining high-grade H_2. Traditional WGS catalysts which are developed for fuel cell applications comprise two components. An oxide such as Al_2O_3, CeO_2 or TiO_2 provides support while a noble metal such as Pt or Au catalyze the various reaction steps [1, 2, 3]. Promoters such as alkali and alkaline earth metals are also often added to the system as a means of further boosting the performance [4, 5, 6]. While this combination of materials makes the small-scale applications of WGS possible, the use of noble metals render it costly and potentially harmful to the environment. In addition, the high impurity levels of the H_2 that is produced is detrimental [7].

Among the myriad of materials suggested for the WGS reaction,transition metal carbides (TMCs) stand out due to their high reactivity [8], extreme hardness [9], high melting point [10], and high electrical/thermal conductivity [11]. Mo_2C is one of the TMCs proposed for the WGS reaction [12].In particular, several reports have been made regarding their higher activity and durability for the WGS reaction when compared to the commercial Cu–Zn WGS catalysts [13, 8]. In Chapter 3, the Mo_2C surface is explored as a catalyst for WGS reaction. With this aim, the adsorption energies are studied for the species involved in the relevant reaction on this surface and activation barriers are calculated for CO molecule, which is our probe molecule. Finally, the effect of the precious metals such as Au, Pt atoms and K atoms as an alkali promoter are discussed in detail.

Chapter 4 aims to study the oxidation of methanol molecule on Au(111) surface. This molecule is used in industrial applications enormously. During the oxidation process of methanol, industrially valuable chemicals are produced. These chemicals can be used in food, polymer and pharmaceutical industries. The size and variety of such products is highly dependent on the environment and the catalyst used. It was experimentally demonstrated that selective oxidation process is catalyzed by metal surfaces. The adsorption and decomposition of the CH_3OH molecule on coinage metals have been studied in great depth due to its enormous use in industry. This method can be utilized in internal combustion engines when CH_3OH is mixed with petrolium source. It has a great potential as hydrogen source for fuel cells. Additionally, it is used as a feed stock for the production of many chemicals. Therefore, the study of its adsorption, its decomposition process and its reaction with catalysts has become important. In this chapter, we calculate the adsorption energies of the molecules and atoms involving in the dissociation process through O-H bond breaking on Au(111) surface, then activation energies for this reaction are examined. This decomposition process is easier on the Au surface with O-add atom . However, obtaining O-atom on the Au surface is not an easy task since it requires many industrial processes. The other goal of this chapter is to perform similar calculations on the Pt-doped surfaces without using O-add atom on the surface.

Solar energy seems to be the most promising energy source to meet rising energy demand. Silicon-based materials are the most suitable materials for producing solar cells. However, there are many difficulties in the production of the silicon-based wafers, one of them being related to the thickness. Standard thin film production methods is not suitable for the silicon wafers. Chapter 5 presents a new technique to produce thinner wafers, where some of the regions of the wafers interacts with the etchant solution much more than the other regions do. The etchant solution consist of HF acid and Cu ions. Therefore, we calculate the interaction between the amorphous silica, crystal silica and oxidized crystal Si surfaces and ions of HF and Cu in order to develop a better understanding of this technique by calculating their adsorption energies on these surfaces.

CHAPTER 2

THEORETICAL BACKGROUND

2.1 Solid State Systems and Their Problems

In order to study any quantum mechanical system, as a first step, the Schrödinger equation is written down with a corresponding Hamiltonian

$$i\hbar\frac{\partial}{\partial t}\Psi = H\Psi. \tag{2.1}$$

Solving this equation with appropriate boundary conditions (2.1) gives the wave function Ψ, which contains all information about the system. Once the wavefunction Ψ is known , some physical properties of the system can be determined.

The exact solution of this equation can be obtained for a few simple systems such as particle in a box, whereas it is not an easy task even for the systems containing more than one electron such as helium. Therefore, solid state systems, which are much more complicated compared to helium, can be studied by employing some approximation methods.

2.2 Many Body Hamiltonian

Solid state systems consist of many electrons interacting with each other and heavy nuclei through electrostatic forces. The behaviour of the system is governed by the non-relativistic Hamiltonian N electrons and N nuclei

$$H = -\frac{\hbar^2}{2m_e}\sum_{i=1}^{N_e}\nabla_i^2 - \frac{\hbar^2}{2m_I}\sum_{I=1}^{N_n}\nabla_I^2 + \frac{1}{2}\frac{e^2}{4\pi\epsilon_0}\sum_{i=1}^{N_e}\sum_{j\neq i}^{N_e}\frac{1}{|\vec{r_i}-\vec{r_j}|}$$

$$-\frac{e^2}{4\pi\epsilon_0}\sum_{i=1}^{N_e}\sum_{I=1}^{N_n}\frac{Z_I}{|\vec{r_i}-\vec{R_I}|}+\frac{1}{2}\frac{e^2}{4\pi\epsilon_0}\sum_{I=1}^{N_n}\sum_{J\neq I}^{N_n}\frac{Z_I Z_J}{|\vec{R_I}-\vec{R_J}|} \tag{2.2}$$

where we use i and j for the electronic coordinates, I and J for the nuclear coordinates. Z and m denote the electric charge and the mass of nuclei respectively. The first two terms in equation (2.2) are kinetic energy of the electrons and nuclei. The 3^{th} term describes the interaction between electron-electron. The remaining terms are interactions between nuclei- electrons , and nucleus-nucleus, respectively.

2.3 Born-Oppenheimer Approximation

As mentioned before, dealing with the many body Hamiltonian in its full form (2.2) is practically not possible. One approach to this problem is an approximation scheme due to Born-Oppenheimer [14]. Since electrons are much lighter than the nuclei, nuclei react to any change not as quickly as electrons. The nuclei are much more localized in space, almost static, which makes it possible to considered them as classical particles. As a result of this, the full wavefunction is written as the product of the electronic wavefunction and the nuclei wavefunction,

$$\chi(r,R)=\Psi(\vec{r},\vec{R})\Phi(\vec{R}) \tag{2.3}$$

where $\Psi(r,R)$ represents the electronic wavefunction depending parametrically on nuclear coordinates R and $\Phi(R)$ represents the nuclear wavefunction. With this picture, the second term in equation (2.3) can be neglected and the potential energy between nuclei-nuclei interaction can be taken as constant for a fixed nuclei configuration. Therefore, the new Hamiltonian, which depends only on the electronic variables, is given in terms of atomic units as

$$\begin{aligned} H &= T_e+V_{en}(\vec{r},\vec{R})+V_{ee}(\vec{r}) \\ &= -\sum_{i=1}^{N_e}\nabla_i^2+\frac{1}{2}\sum_{i}^{N_e}\sum_{j\neq i}^{N_e}\frac{1}{|\vec{r_i}-\vec{r_j}|}-\sum_{i}^{N_e}\sum_{I}^{N_n}\frac{Z_I}{|\vec{r_i}-\vec{R_I}|} \end{aligned} \tag{2.4}$$

We search for the ground state wavefunction Ψ of this Hamiltonian which satisfy

$$H\Psi=E\Psi \tag{2.5}$$

The true wavefunction of electrons not only depends on the electronic coordinates but also depends on spin degrees of freedom assigned as σ. The total variables are denoted as

$$x = \{r, \sigma\} \tag{2.6}$$

and the full antisymmetric wavefunction for N-electron system is given by

$$\Psi = \Psi(x_1, x_2, x_3, ...x_N) \tag{2.7}$$

With the help of this approximation, the Hamiltonian in equation (2.4) becomes easier to handle but it is still a difficult task to solve this equation. The electron-electron interaction, because of the motion of the electrons, makes the problem so complicated that we can not consider their contribution to the energy as that of single particles. Therefore, scientists have been trying to search new approaches to the many body problem.

2.3.1 Hartree and Hartree-Fock Approximation

The idea behind the Hartree approximation is that the electrons are considered to occupy different orbitals in which only one electron can be present [15]. This approach reduces the many body Schrödinger equation to a single particle equation. Every orbital is represented by a function $\phi_i(x_i)$ and the approximate wavefunction is written as the product of the single orbitals

$$\Phi = \prod_{i}^{N} \phi_i(x_i), \tag{2.8}$$

each of them satisfies the single particle Schrödinger equation

$$(\frac{-\hbar^2}{2m}\nabla^2 + V_{eff}^i(r))\phi_i(r) = \varepsilon_i \phi_i(r), \tag{2.9}$$

with the effective potential $V_{eff}^i(r)$ defined as

$$V_{eff}^i(r) = V_{ext} + \int \frac{\sum_{j \neq i} |\phi_i(r')|^2}{|r - r'|} dr'. \tag{2.10}$$

The effective potential V_{eff} is the sum of the potentials which describe the nuclei-electron interaction and the electron-electron interaction. The second term in equation

(2.10) is called Hartree potential, where $|\phi_i(r)|^2$ denotes the charge density. Then, the energy is

$$E_H = \sum_i^N \varepsilon_i - \frac{1}{2}\int\int \frac{n(r)n(r')}{|r-r'|} dr dr'. \tag{2.11}$$

Since the solutions of Hartree equations depend on the orbitals, they are solved by self-consistency . As a first step, an initial orbital is guessed and the effective potential V_{eff} is constructed in terms of it. Then the equation is solved. We employ this procedure until we accomplish to get a wavefunction sufficiently close to the real solution. This procedure is called Hartree self consistency. However, the Hartree approximate-wavefunction or the Hartree product in equation (2.8) fails to represent the true nature of the electrons. This approach treat electrons as distinguishable particles. However, they are indistinguishable fermionic particles and the wavefunction of electrons must satisfy the antisymmetry requirement which can be expressed through the exchange operator P defined as

$$\begin{aligned} P_{ij}\Phi(x_1, x_2, x_3, ..x_i, ..x_j, ...x_N) &= \Phi(x_1, x_2, x_3, ..x_j, ..x_i, ...x_N) \\ &= -\Phi(x_1, x_2, x_3, ..x_i, ..x_j, ...x_N). \end{aligned} \tag{2.12}$$

This is an operator which exchanges the positions of particles equation (2.12), which is a manifestation of the Pauli exclusion principle. If one applies this operator on a fermionic wavefunction, the wavefunction does change its sign. The Hartree approximation does not possess this crucial property and that is why the model is unsuccessful.

In order to satisfy the antisymmetric property of the fermionic wavefunction, a new approximate wavefunction is proposed by Hartree-Fock [16, 17], where the N-electron wavefunction is written as Slater determinant,

$$\Phi = \frac{1}{\sqrt{N!}} \begin{pmatrix} \phi_1(x_1) & \phi_2(x_1) & . & . & . & \phi_N(x_1) \\ \phi_1(x_2) & \phi_2(x_2) & . & . & . & \phi_N(x_2) \\ . & . & . & . & . & . \\ . & . & . & . & . & . \\ . & . & . & . & . & . \\ \phi_1(x_N) & \phi_2(x_N) & . & . & . & \phi_N(x_N) \end{pmatrix} \tag{2.13}$$

$$\Phi_{HF} = \frac{1}{\sqrt{N!}} \sum_{i=1}^{N!} (-1)^{P(i)} \phi_{i1}(x_1)\phi_{i2}(x_2)......\phi_{iN}(x_N). \tag{2.14}$$

The factor $\frac{1}{\sqrt{N!}}$ in equations (2.13) and (2.14) arises as a result of the normalization condition. The Hartree method is essentially the application of the variational principle with Hartree wavefunction (2.8. Hartree-Fock method extends the Hartree method by including the quantum mechanical demands such as exchange properties of electrons and indistinguishability. However, it is still insufficient to include the correlation effects due to the interactions between electrons.

2.3.2 Thomas-Fermi Theory

It was proposed by Thomas and Fermi to use the electron density as a variable instead of the wavefunction [18, 19] . In this approach, a simple expression is obtained for the kinetic energy by using homogeneous electron gas, while the exchange and correlation effects are completely neglected. However, these effects due to interactions are treated classically. The density of the homogeneous electron gas ρ in terms of the Fermi energy ϵ_F is

$$\rho = \frac{1}{3\pi^2} (\frac{2m}{\hbar^2})^{3/2} \epsilon_F^{3/2}, \tag{2.15}$$

and the kinetic energy is given by

$$T(n) = C_F \int n(\vec{r})^{5/3} d\vec{r} \tag{2.16}$$

where $C_F = 2.871$. The total energy is given in terms density as

$$E(n) = C_F \int n(\vec{r})^{5/3} d\vec{r} + \frac{1}{2} \int \int \frac{n(\vec{r}_1) n(\vec{r}_2)}{|\vec{r}_1 - \vec{r}_2|} d\vec{r}_1 d\vec{r}_2 - Z \int \frac{n(\vec{r})}{|\vec{r}|} d\vec{r}. \tag{2.17}$$

The performance of Thomas-Fermi approach is not very good due to the fact that it ignores the exchange and correlation effects which play a crucial role in Density Functional Theory (DFT).

2.3.3 Density Functional Theory

DFT is the most commonly used method for obtaining electronic properties of condensed matter systems. The idea behind it is that writing the total energy in terms of ground state electron density offers a great simplification by reducing the number of degrees of freedom. The theory is applied in systems ranging from atom, molecules, solids to quantum fluids.

The ground state electron density is the fundamental variable and the total energy is a unique functional of electron density. For many particle systems, the density can be obtained by finding the expectation value of the density operator for many body wavefunction. The density operator is defined as

$$\hat{n}(\vec{r}) = \sum_{i=1}^{N_e} \delta(\vec{r_i} - \vec{r}), \tag{2.18}$$

where $\vec{r_i}$ is the position of the ith electron, $\delta(\vec{r_i} - \vec{r})$ is the density of the ith electron and N_e is the total number of electrons. The electron density is given by

$$\begin{aligned} n(\vec{r}) &= <\Psi|\hat{n}(\vec{r})|\Psi> \\ &= \int \Psi^*(r_1, r_2, r_3, ..r_{N_e}) \sum_{i=1}^{N_e} \delta(\vec{r_i} - \vec{r}) \Psi(r_1, r_2, r_3, ...r_{N_e}) d\vec{r_1} d\vec{r_2} ... d\vec{r_{N_e}} \\ &= \int |\Psi(r, r_2, r_3, ...r_N)|^2 d\vec{r_2} d\vec{r_3} .... d\vec{r_N} + \int |\Psi(r_1, r, r_3, ...r_N)|^2 d\vec{r_1} d\vec{r_3} ... d\vec{r_N} + \\ &\quad .... \end{aligned} \tag{2.19}$$

This equation has N$_e$ numbers of integration, and changing the dummy indices gives the integration of the number density as

$$\int n(\vec{r}) d\vec{r} = N_e. \tag{2.20}$$

2.3.4 Hohenberg-Kohn Theorems

The ground state properties is studied by DFT, in which we change our attention from wavefunction to electron density. The energy,

$$H = T + V_{ee} + V_{en} \tag{2.21}$$

where the first and second terms are kinetic energy and Colombic energy between electrons, respectively and they are universal for all electronic systems. The remaining term describes the electron-nuclei interaction, which is again Colombic, but not universal and depends on the configuration of the system. Therefore, the total system is defined by this term uniquely. It is also called the external potential since it includes the effects of external fields such as electric and magnetic fields. We will now state two important theorems which DFT is based on [20].

Theorem 1: The external potential V$_{ext}$ is uniquely determined by the ground state density n$_0(\vec{r})$ up to an additive constant. In other words, there is a one-to-one correspondence between the ground state density and the external potential V.

Proof: Assume that there are two different external potentials resulting in the same ground state density. The corresponding Hamiltonians are given as

$$\hat{H}_1 = \hat{T} + \hat{V}_{ee} + \hat{V}_{ext}^{(1)}, \tag{2.22}$$

$$\hat{H}_2 = \hat{T} + \hat{V}_{ee} + \hat{V}_{ext}^{(2)}. \tag{2.23}$$

from which one can get

$$E_1 < \left\langle \Psi_2 | \hat{H}_1 + \hat{H}_2 - \hat{H}_2 | \Psi_2 \right\rangle \tag{2.24}$$

$$E_1 < \int d\vec{r} n_o(\vec{r})(\hat{V}_{ext}^{(1)} - \hat{V}_{ext}^{(2)}) + E_2 \tag{2.25}$$

Changing the indices in equations (2.24) and (2.25) and doing the same for E$_2$ give

$$E_2 < \int d\vec{r} n_o(\vec{r})(\hat{V}_{ext}^{(2)} - \hat{V}_{ext}^{(1)}) + E_1. \tag{2.26}$$

Then, the sum of equations (2.25) and (2.26) yields

$$E_1 + E_2 < E_1 + E_2, \tag{2.27}$$

which is a contradiction. Therefore, we conclude that it is impossible to find two different external potential corresponding to the same ground state.

Theorem 2: The second theorem shows the variational nature of the problem. It states that the energy corresponding to a certain density takes its minimum value , if this density is the true ground state density.

Proof 2: The energy in terms of density is

$$\begin{aligned} E(n) &= T(n) + V_{ee}(n) + \int V_{ext}(\vec{r}) n(\vec{r}) d\vec{r} \\ &= \mathcal{F}\left[n(r)\right] + \int V_{ext}(\vec{r}) n(\vec{r}) d\vec{r} \end{aligned} \tag{2.28}$$

where $\mathcal{F}\left[n(r)\right]$ is the universal functional which is identical for all electronic systems. The ground state energy is in terms of the actual ground state density $n_0(\overrightarrow{r})$ is given by the variational principle,

$$E_0\left[n_o\right] \;=\; \left\langle \Psi_0[n_0]|\hat{H}|\Psi_0[n_0]\right\rangle \leq < \Psi_0[n_0]|\hat{H}|\Psi_0[n_0] >= E_k[n'] \qquad (2.29)$$

when $n_0 = n'$, the equality is satisfied.

2.3.5 Kohn-Sham Approach

2.3.5.1 Total energy in terms of density

The material properties are investigated by DFT for interacting electron system with an external potential. As mentioned above, the wavefunction of the full system is 3N-variable, one can reduce the number of variables by writing every terms electron density. We can find the observables corresponding to the Hamiltonian by taking the expectation value of it as follows.

$$\hat{H} \;=\; -\frac{1}{2}\sum_i \nabla_i^2 - \sum_i^{N_e}\sum_j^{N_n}\frac{Z_j}{|\vec{r}_i-\vec{r}_j|} + \frac{1}{2}\sum_{i\neq j=1}^{N_e}\frac{1}{|\vec{r}_i-\vec{r}_j|}. \qquad (2.30)$$

The total energy of the system is obtained by

$$E = \left\langle \Psi|\hat{H}|\Psi\right\rangle. \qquad (2.31)$$

The second term in equation (2.30) is the nuclei-electron interaction also called external potential which represents the effects of the other fields. It is a single particle operator and it is assumed that this term does not include any derivative. Therefore this calculation can be performed easily. The expectation value of that operator is given as,

$$\begin{aligned}
&\left\langle \Psi(\vec{r}_1,\vec{r}_2,...,\vec{r}_N)|\vec{V}_{ext}|\Psi(\vec{r}_1,\vec{r}_2,...,\vec{r}_{N_e})\right\rangle \\
=\;& -\sum_i^{N_e}\sum_j^{N_n}\int \Psi(\vec{r}_1,\vec{r}_2,...,\vec{r}_{N_e})\frac{Z_j}{|\vec{r}_i-\vec{R}_j|}\Psi(\vec{r}_1,\vec{r}_2,...,\vec{r}_N)d\vec{r}_1 d\vec{r}_2...d\vec{r}_{N_e} \\
=\;& -\sum_j^{N_n}[\int \frac{Z_j}{|r_1-R_j|}d\vec{r}_1\int |\Psi(\vec{r}_1,\vec{r}_2,...,\vec{r}_{N_e})|^2 d\vec{r}_2 d\vec{r}_3...d\vec{r}_N] \\
& +\int \frac{Z_j}{|r_2-R_j|}d\vec{r}_2\int |\Psi(\vec{r}_1,\vec{r}_2,...,\vec{r}_{N_e})|^2 d\vec{r}_1 d\vec{r}_3...d\vec{r}_N] + ...].
\end{aligned} \qquad (2.32)$$

There are N$_e$ identical terms in equation (2.32). By using the definition of the density in equations (2.19) and (2.20), each term in the second integral can be shown to be equal to $\frac{n(r_i)}{N_e}$, which yields

$$E_{ext} = \int V_{ext}(\vec{r})n(\vec{r})d\vec{r}. \tag{2.33}$$

This is the expectation value of the external potential in terms of density.

We will now do the same calculation for the electron-electron interaction term. However, it is not as easy as the external potential since it can not be written in terms of single particle density directly. First, we define this interaction in terms of single particle operators and all the other effects are included in the correlation term. The expectation value for the electron-electron interaction V$_{ee}$ is given by

$$\begin{aligned}
E_{ee} &= \Big\langle \Psi(\vec{r}_1,\vec{r}_2,...,\vec{r}_N)|\vec{V}_{ee}|\Psi(\vec{r}_1,\vec{r}_2,...,\vec{r}_N)\Big\rangle \\
&= \frac{1}{2}\sum_{i\neq j=1}^{N}\int \Psi(\vec{r}_1,\vec{r}_2,...,\vec{r}_N)\frac{1}{|\vec{r}_i-\vec{r}_j|}\Psi(\vec{r}_1,\vec{r}_2,...,\vec{r}_N)d\vec{r}_1 d\vec{r}_2....d\vec{r}_N \\
&= \frac{1}{2}\sum_{i\neq j=1}^{N}\int \frac{d\vec{r}_i d\vec{r}_j}{|\vec{r}_i-\vec{r}_j|}\int |\Psi(\vec{r}_1,\vec{r}_2,..,\vec{r}_i,..,\vec{r}_j,..,\vec{r}_N)|^2 d\vec{r}_1 d\vec{r}_2....dr_N
\end{aligned} \tag{2.34}$$

Renaming dummy indices ($\vec{r}_i,\vec{r}_j \longrightarrow \vec{r},\vec{r}\,'$) and using the definition of density for two particles

$$n(\vec{r}_1,\vec{r}_2) = N(N-1)\int d\vec{r}_3 d\vec{r}_4...dr_N|\Psi(\vec{r}_1,\vec{r}_2,...\vec{r}_N)|^2, \tag{2.35}$$

give the electron-electron interaction energy as

$$\begin{aligned}
E_{ee} &= \frac{1}{2}N(N-1)\int \frac{d\vec{r}d\vec{r}\,'}{|\vec{r}-\vec{r}\,'|}\int |\Psi(\vec{r}_1,\vec{r}_2,..,\vec{r},..,\vec{r}\,',..,\vec{r}_N)|^2, \\
E_{ee} &= \frac{1}{2}\int \frac{d\vec{r}d\vec{r}\,' n^2(\vec{r},\vec{r}\,')}{|\vec{r}-\vec{r}\,'|},
\end{aligned} \tag{2.36}$$

where $n^2(\vec{r},\vec{r}\,')$ is the probability density of finding an electron at $\vec{r}$ and the other one at $\vec{r}\,'$. This term assumes that there is no correlation between two electrons. It is purely classical, which ignores the fermionic nature of the electrons. Therefore, the quantum behavior comes as a correction term tothe two particle density term

$$n^2(\vec{r},\vec{r}\,') = n(\vec{r})n(\vec{r}\,') + \triangle n^2(\vec{r},\vec{r}\,'), \tag{2.37}$$

where $\triangle n^2(\vec{r},\vec{r'})$ is the correction term which represents the correlation effects (purely quantum mechanical). The resulting energy due to the interactions between electrons is also called Hartree energy. Since the kinetic energy term contains derivative, it is difficult to find everything in terms of explicit functional of the density. Therefore, Kohn and Sham introduced a method for computing the kinetic energy functional for a better accuracy [21]. The idea behind their method is that they replace the kinetic energy of N-interacting particle system with an equivalent non-interacting one. With this assumption, the ground state density of the fictitious non-interacting system is the same as that of the real system. The density can be written as the norm squared of the single particle orbitals called Kohn-Sham orbitals

$$n(\vec{r}) \;=\; \sum_{n=1}^{N_e} |\phi_n(\vec{r})|^2. \tag{2.38}$$

Therefore, the kinetic energy in terms of the single particle orbitals is given by

$$T \;=\; -\frac{1}{2}\sum_{n}^{N_n}\int d\vec{r}\phi_n^*(\vec{r})\nabla^2\phi_n + \triangle T. \tag{2.39}$$

This kinetic energy term is not the true kinetic energy, because it ignores the interacting effects. In order to capture them, a correction term is added to the kinetic energy as in the equation (2.39). Then, all terms add up to the total energy as

$$\begin{aligned} E \;=\; & -\frac{1}{2}\sum_{n}^{N_n}\int d\vec{r}\phi_n^*(\vec{r})\nabla^2\phi_n + \int V_{ext}(\vec{r})n(\vec{r})d\vec{r} + \frac{1}{2}\int \frac{d\vec{r}d\vec{r'}n^2(\vec{r},\vec{r'})}{|\vec{r}-\vec{r'}|} \\ & + \triangle T + \triangle E_{ee}. \end{aligned} \tag{2.40}$$

Here, the terms $\triangle T + \triangle E_{ee}$ are called the exchange-correlation energy, originated from the difference between interacting and non-interacting system.

2.3.6 Functionals for Exchange and Correlations

2.3.6.1 The Local Density Approximation

Every energy term in the many body Hamiltonian is defined by Kohn-Sham orbitals. However, writing the exchange-correlation term in terms of the density is still a challenging task because this term is not exactly known. Therefore, it must be approximated in such a way that the exchange and correlation effects are captured exactly to make the computation more accurate. Among many possible approximations, the most easiest and most commonly used method is Local Density Approximation (LDA) [22]. In this approximation, the non-homogeneous system is divided into volume elements d$^3\vec{r}$. Then, the system is treated with the assumption that there is homogeneous electron gas at density n($\vec{r}$) in every volume element instead of the non-homogeneous gas. The exchange and energy functional are taken as

$$E_{xc}[n] \approx E_{xc}^{LDA} = \int d^3\vec{r}n(\vec{r})\varepsilon_{xc}(n(\vec{r})), \tag{2.41}$$

where $\varepsilon_{xc}(n(\vec{r}))$ is the energy per electron in a homogeneous electron gas at density n(r).

The performance of the LDA is quite satisfying for systems where the electron density is uniform or slowly changing. However, it fails to predict some properties of materials in which the density oscillates very rapidly. Therefore, LDA should be improved for better accuracy.

2.3.6.2 The Generalized Gradient Approximation

Besides LDA, there are methods developed for approximating the exchange-correlation energy to make the computation more accurate such as Generalized GradientApproximation (GGA) [23]. The main idea behind this approximation is that the ε_{xc} term takes into account not only the electron density at $\vec{r}$ but also consider the density gradient at that point $\nabla n(\vec{r})$. Therefore, the functional is given by

$$E_{xc}^{GGA} = \int d^3\vec{r}n(\vec{r})\epsilon_{xc}(n(\vec{r}), |\nabla n(\vec{r})|) \tag{2.42}$$

This method estimates binding energies and atomic energies more accurately when compared to the LDA. It also recovers the bonding angles and bond lengths.

2.3.7 Kohn-Sham Equations

Once a proper exchange-correlation functional is chosen, the remaining work is a minimization procedure by using variational principle with respect to Kohn-Sham orbitals to obtain ground state energy, density and wavefunctions. The total energy is given by

$$
\begin{aligned}
E[n] &= -\frac{1}{2}\sum_{n}^{N_n}\int d\vec{r}\phi_n^*(\vec{r})\nabla^2\phi_n + \int V_{ext}(\vec{r})n(\vec{r})d\vec{r} + \frac{1}{2}\int \frac{d\vec{r}d\vec{r}' n^2(\vec{r},\vec{r}')}{|\vec{r}-\vec{r}'|} \\
&\quad + \int d^3\vec{r} n(\vec{r})\varepsilon_{xc}(n(\vec{r})) \\
\frac{E[n]}{\delta\phi_i^*} &= \varepsilon_i\phi_i(\vec{r}) \\
&= \Big[-\frac{1}{2}\nabla^2 + V_{ext} + \int \frac{d\vec{r}' n(\vec{r}')}{|\vec{r}-\vec{r}'|} + \epsilon_{xc}[n] + n(\vec{r})\frac{\delta\epsilon_{xc}[n(\vec{r})]}{\delta n(\vec{r})}\Big]\phi_i, \qquad (2.43)
\end{aligned}
$$

and, with LDA for exchange and correlation energy, one can get

$$
(\hat{T} + V_{eff})\phi_i = \varepsilon_i\phi_i \qquad (2.44)
$$

The Kohn-Sham equations (2.44) represent the solution of N-single particle Schrödinger-like equations for interacting electrons under the effect of the potential V$_{eff}$. ϕ_i and ε_i are the wavefunctions and energies, respectively. However, it is not easy to calculate the energies and orbitals. Hartree term and exchange operator directly depend on the density itself, while the other operators in the Hamiltonian depend on the Kohn-Sham orbitals. There is an interrelation between density, Kohn-Sham orbitals and Hamiltonian. Therefore, the solutions of Kohn-Sham equations are accomplished by self-consistency. In this method an initial density is chosen and the equation (2.44) is solved in order to find the Kohn-Sham orbitals and energies. By using this Kohn-Sham orbitals, new density is written and again above equation is solved to find the new orbitals and energies. This process continues iteratively until there is a small difference between the densities obtained in consecutive iterations. After having obtained the density, one can calculate the energy of the system, forces and stresses etc..

2.3.8 Periodicity and The Bloch's Theorem

The crucial property of crystals for ab-initio calculations is that they are composed of orderly arranged atoms, which causes a long range periodicity in crystals. Therefore, a crystal remains unchanged when it is translated by a lattice vector $\vec{R}$, which leads us to conclude that the crystal potential seen by electrons is also periodic under such a translation

$$U(\vec{r}) \;=\; U(\vec{r}+\vec{R}), \tag{2.45}$$

where $U(\vec{r})$ is the crystal potential seen by electrons and $\vec{R}$ is the direct lattice vector.

Bloch's theorem states that the eigenfuntions of such periodic potentials corresponding to a single particle Hamiltonian in equation (2.44) can be written as [24],

$$\Psi_{\vec{k}}(\vec{r}) \;=\; e^{i\vec{k}.\vec{r}}\,U_{\vec{k}}(\vec{r}). \tag{2.46}$$

This wavefuntion, which is also called Blochs' state, is translated by a lattice vector as follows

$$\Psi_{\vec{k}}(\vec{r}+\vec{R}) \;=\; e^{i\vec{k}.\vec{R}}\Psi(\vec{r}), \tag{2.47}$$

where $\vec{k}$ is called crystal momentum, which is originated from the translational symmetry. The equation (2.47) is the alternative form of the Bloch's theorem.

Bloch's wavefunction has some important properties. The planewave form of the Bloch's wavefunction emphasizes that the electron travels in a crystal like a free particle modulated by a periodic crystal potential. This wavefunction also shows the non-localized character of the electron on a particular atom. The electron is shared by the whole crystal.

2.3.9 Planewave Expansion and Technical Issues

Solving Kohn-Sham equations 2.44 directly is still an impossible task, and as mentioned previously it is reasonable choice to expand wave functions in terms of planewaves. The usage of planewaves as a basis gives us to opportunity to turn the real space equations into momentum space matrix equations. To work with matrix equations is much easier than to work with real space ones.

2.3.9.1 Pseudopotential Approximation

The fact that a solid state system possesses many electrons requires the usage of many planewaves as basis to expand Kohn-Sham orbitals, which makes the problem more challenging from the computational point of view.

We know that the core electrons are more localized and do not contribute the bonding process whereas valance electrons, which are more delocalized and play a dominant role in bonding. The core electrons are also more oscillatory around nucleus, resulting in the usage of more planewaves to resolve these oscillations by spending more computational power. In order to handle this problem, one must make pseudopotential approximation. The idea behind this method that we use only valance electrons instead of using core electrons by replacing the oscillatory Coulomb potential by a smoother and weaker one, called pseudopotential. This gives us to opportunity to work with a smaller system by reducing the number of planewave base. We also eliminate the relativistic effects which are due to the core region.

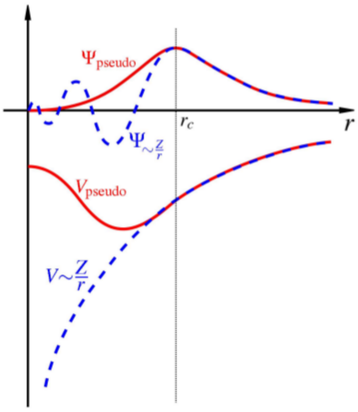

Figure 2.1: Illustration of the oscillatory wavefunction of nucleus corresponding to blue one, and the red one represents the pseudo wavefunction which is smoother. These two coincide at the radius of rc [25].

Assume that we have an isolated atom with its Hamiltonian $\hat{H}$ and valance state $|\phi\rangle$. This true valance state $|\psi\rangle$ is replaced by a smooth pseudo-function $|\phi\rangle$, and the remaining part is expanded in terms of the core states $|\chi_n\rangle$ as the equation (2.48). The Hamiltonian $\hat{H}$ and the valance state ψ satisfy the below (2.49)

$$|\psi\rangle = |\phi\rangle + \sum_{n}^{core} C_n |\chi_n\rangle \tag{2.48}$$

$$\hat{H}|\psi\rangle = E|\psi\rangle \tag{2.49}$$

and core states satisfying the eigenvalue equation of

$$\hat{H}|\chi_n\rangle = E_n|\chi_n\rangle \tag{2.50}$$

One can multiply (2.48) with $\langle \chi_m |$ and obtain that

$$C_m \; = \; - \langle \chi_m | \phi \rangle \, , \tag{2.51}$$

whose substitution into equation (2.48) yields

$$|\psi\rangle \; = \; |\phi\rangle - \sum_{n}^{core} |\chi_n\rangle \langle \chi_m | \phi \rangle \tag{2.52}$$

Then, applying the $\hat{H}$ Hamiltonian operator on the equation (2.52) results in

$$(\hat{H} + \textstyle\sum_n^{core} (E - E_n) |\chi_n\rangle \langle \chi_n |) |\phi\rangle \; = \; E |\phi\rangle \, , \tag{2.53}$$

where the term $(\hat{H} + \sum_n^{core} (E - E_n) |\chi_n\rangle \langle \chi_n |)$ is treated as new Hamiltonian which gives exactly same energy over the pseudo-function. Also, $(E - E_n)$ is more repulsive term that cancels the effect of the attractive nature of the Coulomb potential.

2.3.9.2 Integration over K Points

In DFT calculations, the electron density can be evaluated by integration over k points appearing in Bloch's state (2.46). Therefore choosing of sufficient number of k points is important in DFT calculations. There are two commonly used methods of choosing k points, which are Monkhorst-Pack scheme [26] and tetrahedral method [27]. In this thesis, Monkhorst-Pack scheme is used for integration where k points are homogeneously distributed in Brillouin zone.

The number of k points depends on the crystal shape, size and crystal symmetry. The bigger the unit cell used in real space, the number of k points for integration is less.

2.3.9.3 Smearing

For insulators and semiconductors, the charge density smoothly goes to zero before the band gap. The integration over k points, therefore, has no problem. On the other hand, for metals, the charge density sharply drops and goes to zero. The function to be integrated over k points is multiplied by a sharp delta function which makes the resolution very difficult with planewaves. In order to handle this problem, this sharp Fermi function is replaced by a smoother one called smearing function, which makes the integrand smoother.

2.3.10 Adsorption Energies

In order to study the adsorption of atoms and molecules, an appropriate surface is constructed. The adsorption energy is a crucial observable between surface and atoms or molecules. The adsorption process takes place on a surface which is called adsorbent. Adsorbate is defined as that any chemical species which get adsorbed by surface. These definitions are depicted in the given Figure 2.2. Adsorption energy is defined as

$$E_{ads} = E_{slab/adsorbate} - (E_{slab} + E_{adsorbate}) \tag{2.54}$$

where $E_{slab/adsorbate}$ is the total energy of the slab with adsorbed molecule or atom, E_{slab} is the total energy of the slab without adsorbate and the last term is the total energy of the adsorbate alone.

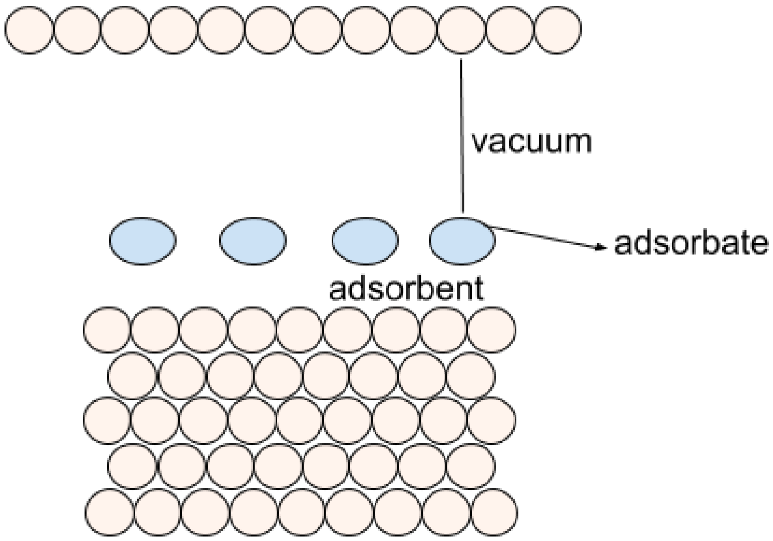

Figure 2.2: Scheme of the slab model for the adsorption.

2.3.11 Calculation of Activation Energies

The activation energy is defined as the minimum energy that is required for a reaction to take place. A reaction starts with reactants that change into products by breaking the bonds in the reactants. The all species during this process pass through an highest energy state which is called transition state. This is an unstable state therefore reactants do not stay longer times, they proceed another reaction steps. All these definitions are depicted in the Figure 2.3.

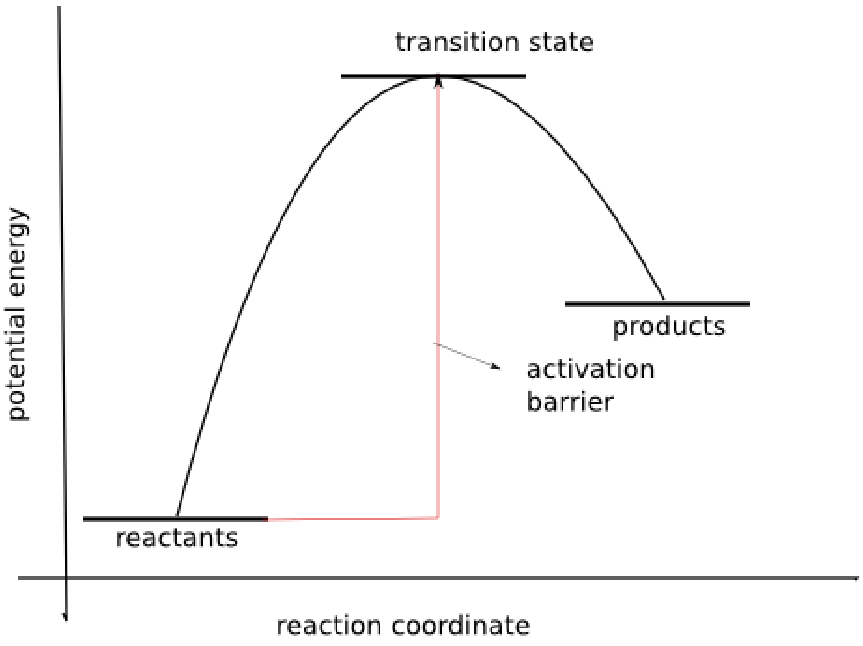

Figure 2.3: Illustration of reactants, transition state and producst.

As discussed previously, DFT calculations can be utilized to find equilibrium positions of reactants on the surface and corresponding minimum energy states. However, in order to estimate the activation energy, we need information about intermediate steps, which requires new tools. In this section, we will first introduce the concept of transition state and minimum energy path. Then, we will present a widely used method to find them, Nudged Elastic Band Method (NEB) and an improved version of it Climbing Image NEB (CI-NEB).

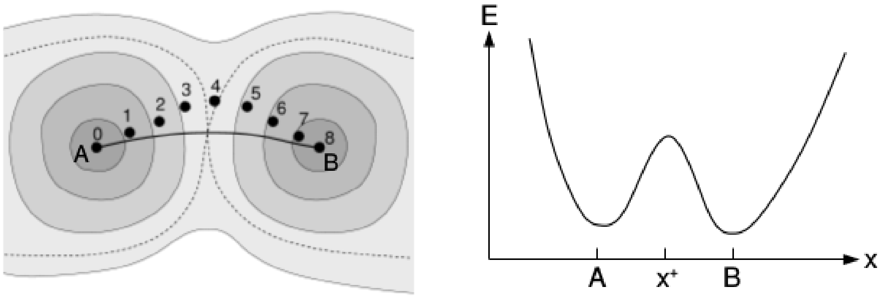

Figure 2.4: The left one represents the two dimensional potential energy landscape. A and B points are the local minimas and the line connected between them is MEP. The right one represents the energy profile of the MEP.[28]

When dealing with chemical processes, it is often useful to consider the system in terms of the overall energy $E(\vec{R}_1, \vec{R}_2, ..., \vec{R}_N)$ where $\vec{R}_i$ is the position of ith atom. Then, a chemical process can be thought of as a transition of atoms from one local minima to another. The initial configuration for reactants and the final configuration for products correspond to local minimas. There are infinitely many paths on the surface for this process to occur, but we have to find the one for which the required energy is minimum. This specific path connecting the two local minimas is called the minimum energy path (MEP). Through a MEP, the system undergoes an energy barrier which can be visualized if we imagine a line connecting the local minimas and use the so called " reaction coordinate ” as in figure. The saddle point between the two minima is called the transition state.

2.3.11.1 Nudged Elastic Band Method

NEB is a method to find the MEP between the initial and final states along with the saddle points[29]. In this method initial and final stages are connected to each other by springs and n number of images are inserted between them along the MEP. For every image, methods find the minimum energies to control the equal spacing with the help of these springs. The forces acting on the every image i has to two components.

$$F_i^{NEB} = F_i^{\perp} + (F_i^s)^{\parallel}$$

where $F_i^{\perp}$ is component of the true force which is perpendicular to the unit tangent of the path for image i, and $(F_i^s)^{\shortparallel}$ is the parallel component of the spring force.

The perpendicular force along the path can written as true force minus parallel component of the true force.

$$F_i^{\perp} \;=\; -\left\{\overrightarrow{\nabla}E(\overrightarrow{R}_i) - \overrightarrow{\nabla}E(\overrightarrow{R}_i).\hat{\tau}_i\hat{\tau}_i\right\}$$

where E is the energy of the i th state which is a function of the atomic coordinates. This perpendicular component of the true force drives to nudge all images around the MEP.

$$(F_i^s)^{\shortparallel} \;=\; k((\overrightarrow{R}_{i+1} - \overrightarrow{R}_i) - (\overrightarrow{R_i} - \overrightarrow{R}_{i-1})).\hat{\tau}_i$$

$(\overrightarrow{R}_{i+1} - \overrightarrow{R}_i)$ is the distance between i+1 state and i state,$(\overrightarrow{R_i} - \overrightarrow{R}_{i-1})$ is the distance between i state and i-1 state and k is the spring constant. This spring force makes the images equally spaced, otherwise the images tend to fall down their initial and final stages. When the images are on the MEP, the perpendicular component is equal to zero. In NEB method, it is difficult to find the exact transition states . Therefore, accurate activation barrier is not found. CI-NEB is an improved version of NEB which finds the true transition states and accurate value for the activation barrier[30].

CHAPTER 3

EFFECT OF PLATINUM, GOLD, AND POTASSIUM ADDITIVES ON THE SURFACE CHEMISTRY OF CDI$_2$-ANTITYPE MO$_2$C

3.1 Introduction

With the industrialization and the growth of population, the energy demand of humanity has increased steadily in the last few decades. This energy need is met mainly by fossil fuels which are unsustainable and, additionally, harmful for the environment. When the fossil fuels are burned, they emit toxic gases such as CO_2. These gases result in a gradual increase of the surface temperature of the earth, resulting in global warming. The effects of this heating are serious and ubiquitous. The heat is melting the land ice, causing rise of the sea levels and flooding. It forces animals to search new areas to live, which is seriously threatening some species. It affects the climate as well leading to extreme weather conditions, affecting the agriculture system which makes people to confront many additional problems. In order to mitigate these problems, an extensive search has been launched for clean and renewable energy sources.

Hydrogen is a good alternative energy carrier due to the low level of pollution that it causes. In addition, it is the most abundant element in the universe. Despite its abundance, it has to be manufactured via a reforming process to extract it from the compounds like water and hydrocarbons. The water gas shift reaction (WGS) 3.1,

$$\mathrm{CO} + \mathrm{H_2O} \longleftrightarrow \mathrm{CO_2} + \mathrm{H_2}, \tag{3.1}$$

is employed extensively in industry as a means of simultaneously reducing the harmful CO gas content and producing H_2 as a clean energy alternative [31]. This reaction is exothermic ($\triangle$H = -41 kJ/mol) and realized in industrial applications in two stages with the help of catalysts. At the high temperature stage (300-450 °C) Cu-promoted Fe_3O_4 catalysts are used [32] while the low-temperature stage (200-240 °C) is facilitated by Cu-promoted ZnO catalysts [33]. There has been much research on this reaction; however, the exact reaction mechanism is not known [34]. Two multi-step reaction mechanisms have been proposed for the WGS reaction, namely the redox mechanism and associative mechanism [4]. In the redox mechanism, oxidation of the CO molecule with absorbed O coming from the dissociation of the water molecule is involved [35, 36]. For the case of the associative mechanism, formate species are produced by the reaction between absorbed CO molecule and OH molecule coming from the dissociation of water [37].

However, the conditions under which industrial applications proceed are not appropriate at smaller scales, such as portable fuel cells used in transportation. An active field of research has been developed to identify materials that could be used as catalysts in small scale applications with the goal of reducing the cost, bringing down the optimal ambient temperature and obtaining high-grade H_2. Traditional WGS catalysts which are developed for fuel cell applications comprise two components. An oxide such as Al_2O_3, CeO_2 or TiO_2 provides support while a noble metal such as Pt or Au catalyze the various reaction steps [1, 2, 3]. Promoters such as alkali and alkaline earth metals are also often added to the system as a means of further boosting the performance [4, 5, 6]. While this combination of materials makes the small-scale applications of WGS possible, the use of noble metals render it costly and potentially harmful to the environment. In addition, the high impurity levels of the H_2 that is produced is detrimental [7].

Among the myriad of materials suggested for the WGS reaction, transition metal carbides (TMCs) stand out due to their high reactivity [8], extreme hardness [9], high melting point [10], and high electrical/thermal conductivity [11]. It has been observed that they display high catalytic performance as catalysts in many industrial processes such as hydrodenitrogenation [38], hydrodesulfurization [39], hydrogenation of CO [40].

Mo_2C is one of the TMCs proposed for the WGS reaction [12]. In particular, several reports have been made regarding their higher activity and durability for the

WGS reaction when compared to the commercial Cu–Zn WGS catalysts [13, 8]. In spite of the experimental interest, there have been relatively few theoretical studies on Mo_2C for use in the WGS reaction. Binding geometries and adsorption energies of reactants, products and intermediates is an important step in understanding reaction mechanisms. Therefore, considerable effort has been spent in studying adsorption of molecules on several Mo_2C surfaces with the help of the DFT.

The species of H, O, CO, NO and CO_2 are involved in many catalytic reactions, and therefore much research has been devoted to their study on Mo_2C. Shi *et al.* performed a detailed DFT investigation on CO and NO adsorption at active sites of β-Mo_2C (001) surface [41] within the Generalized Gradient Approximation. In this study, C-terminated and Mo-terminated Mo_2C surfaces were studied. The binding energies were compared and it was found that for the C-terminated surface the binding energies are relatively small and NO adsorption is stronger than CO adsorption. Additionally, atomic adsorptions of C, O and N were examined and, for both terminations in the range between 5 eV and 7.7 eV, which are quite large. A similar study was conducted by Ren and co-workers who scrutinized the adsorption of O and CO on the α-Mo_2C (001) surface with different terminations by using DFT calculations [42]. Again, they compared the adsorption energies. The general result for these and similar studies is that the species attach to the surfaces through strong covalent bonds or Coulombic interactions.

Moreover, the promoter effects on the adsorption and co-adsorption energies of the species involving the reaction have been investigated. Pistonesi et al. examined the effect of K effect as a promoter on the CO adsorption on the Mo-termination of the Mo_2C(001) surface [43]. They observed that the adsorption energies are more favorable for the K-promoted surface. Furthermore, an increase was reported in binding energies when the concentration of K atoms on surface was increased. Both situations were accompanied by charge transition of charge from the surface to the CO molecule. Han et al. examined the adsorption of H and CO with K and Rb on the α-Mo_2C

In addition to the adsorption studies, activation energy calculations are performed for the energetics of the reaction of WGS and other reactions. Tominaga et al. studied the

WGS reaction on β- Mo_2C (001) slab and examined some reaction steps such as CO adsorption and decomposition of the H_2O [44]. The rate limiting steps were determined to be reaction between CO and O to form CO_2. Another recent study by Wang et al. examined CO dissociation with high coverage on the C and Mo terminations of orthorhombic Mo_2C [45]. They aimed to probe how coverage level effects the CO adsorption and energetics. They observed that there was a decrease in the binding energies with increasing coverage, similar trends were also noted for the case of the C-terminated surface. Finally, they concluded by calculating the energy barriers that at higher coverage levels (n=9-16), the molecular adsorption of CO was observed, whereas only for the case of the lower coverage levels the dissociative CO adsorption become feasible. The only molecular adsorption of the CO for all coverages was reported on C-terminated surface, although the dissociative adsorption did not occur. The same group also examined CO and H_2 adsorption and co-adsorption on Mo_2C(001) by calculating the activation barrier for dissociation to be 2.01 eV [46]. This larger dissociation energy was attributed to the fact that CO dissociation was difficult on a metallic Mo-terminated surface. Besides, the H_2 dissociation energy was computed to be 0.08 eV indicating that dissociation was favorable on the surface.

There is a wide-spread belief that in contrast to the generic materials used in WGS reactions, Mo_2C does not necessitate the use of a precious metal component to catalyze some of the reaction steps. Due to the lack of a well-established theoretical background, the conditions under which this prediction applies to Mo_2C surfaces have yet to be understood. In this context, we explore the catalytic performance of several Mo_2C (001) surfaces with and without precious metals. The aim of this chapter is to tackle this problem in three stages. First, we explore the binding energies of atomic and molecular species that are relevant in the WGS reaction. In particular, we present calculated binding energies of H, O, C, Pt, Au and K atoms and OH, H_2O, CO and CO_2. Our extensive adsorption characteristics study reveals interesting trends for the different surfaces. Next, we study the effect of the precious metals (Pt and Au) and the promoter (K) on the adsorption properties by means of selecting a benchmark molecule, namely CO, and calculating its adsorption energy in the presence of these three helper species. Finally, we calculate the activation energies of the two reactions belonging to the long reaction mechanism of the WGS process, CO dissociation and

H_2 formation.

3.2 Computational Details

In this work, all DFT calculations were performed using the Quantum Espresso suite [47]. GGA exchange correlation functional with the Perdew-Wang parametrization (PW91) was employed to threat the atomic cores [23]. The programs XCrysden [48] and Jmol [49] were used to visualize and to produce the figures. During the geometry optimizations, the force tolerance per atom was set to 0.001 eV/Å. In order to truncate the planewave basis kinetic energy cutoff and density cutoff were chosen as 40 Ry and , 400 Ry, respectively. The Monkhorst-Pack scheme [26] was used for numerical integration in BZ with k point mesh of $8 \times 8 \times 1$. For surface calculations, a vacuum layer of at least 14 Å was used in order to minimize interaction between periodic copies of the slabs.

Projected density of states (PDOS) were performed to obtain insight into the contribution to the density of states coming from the different orbitals. In order to analyze e charge transfer between adsorbate and surface, Bader charge [50, 51] analysis was also performed. Finally, Climbing-Image Nudged Elastic Band (CI-NEB) method [30] was employed to determine the transition states and activation barriers for reactions.

3.3 DFT Calculations

3.3.1 Bulk Structure

Among the several unambigiously identified polymorphs of Mo_2C, three structures have been studied the most often. The α-Mo_2C phase has an orthorhombic structure [52] where the Mo atoms are organized on a hexagonal sub-lattice with C atoms on every other layer along the (0001) direction. The β-Mo_2C polymorph, on the other hand, has a hexagonal structure [53] with a similar underlying hexagonal Mo network but with C atoms on every third layer. Finally, a recently identified phase

[54], the so-called eclipsed orthogonal configuration, is a reconstructed α phase [55]. As both the α and β phases are constructed based on the hexagonal Mo network, there appears to be some confusion concerning nomenclature. α and β are used in literature interchangeably to refer to either polymorph [56, 57]. In order to avoid this confusion, we adopt the explicit naming convention, CdI_2 antitype, recently used by Tominaga *et al.* [58] and Wang *et al.* [59] for the polymorph studied in the present work, which corresponds to hexagonal Mo_2C.

β-Mo_2C has a hexagonal structure with a unit cell of 3 atoms, and an experimental c/a ratio of 1.58 [60]. While determining the lattice constant several methods were employed. First *a* was varied and *c* was kept constant to find the (a,c) pair that gives the minimum energy. Within this method *a* value was found to be as 3.06 Å with an error 1.76% with respect to the experimental value given Table 3.1. Next, a calculation was conducted where *c* was varied and *a* was kept constant. The value 'c' is found as 4.96 A° with error 3.96%. With the expectation of a more accurate result, variable cell relaxiation was performed, however it yielded results with high error. The values finally used for *a* and *c*, to construct the surface slabs are 3.06 A° and 4.61 A° with errors of 1.58 % and 3.43 % with respect to the experimental values respectively. These results were obtained through a constant volume calculations where the volume of the unit cell was fixed to its experimental value. This result is in agreement both with previous theoretical studies [54]. All the results are recapitulated in Table 3.1

Table 3.1: Lattice constants of CdI_2 antitype Mo_2C using different methods.

	a [Å]	c [Å]
Experimental	3.01	4.77
Fixed a/variable c	3.01	4.96
Fixed c/variable a	3.06	4.77
Variable cell relaxation	3.10	4.67
Constant volume calculation	3.05	4.61

The (001) surface of the CdI_2 antitype phase of Mo_2C has an ABCABC... repeating pattern of non-stoichiometric layers. Two consecutive Mo terminated surfaces are followed by a C terminated surface, making it possible to terminate the structure with three distinct surfaces. The (001) surface was studied using a 2×2 slab with 5, 6 or 7 layers depending on the particular termination being modelled. The two bottommost layers were fixed to mimic the bulk behaviour for all slab calculations. The adequacy of our slabs are confirmed by a study reported by Shi at al. [41] in which the adsorption energies of CO molecule differ about 0.1 eV from the those found in our calculations. The first of the two Mo-terminations is represented by a five-layer slab which terminates with Mo (Mo1-Mo$_2$C) atoms, followed by six-layers slab of Mo-terminated (Mo2-Mo$_2$C) and C-terminated (C-Mo$_2$C) β-Mo$_2$C are also examined. The geometry optimized surfaces shown in Figure 3.1 will be referred to as Mo1, Mo2 and C-terminated surfaces in the rest of this work. No significant surface reconstruction was observed during the geometry optimization. For all calculations, we consider the adsorption sites depicted in the Figure 3.1 namely h1, h2, b and t sites and investigate the adsorption energies with other atoms and molecules. Here h1 and h2 refer to hexagonal sites, where h1 has a ... site underneath and h2 has a ... site.

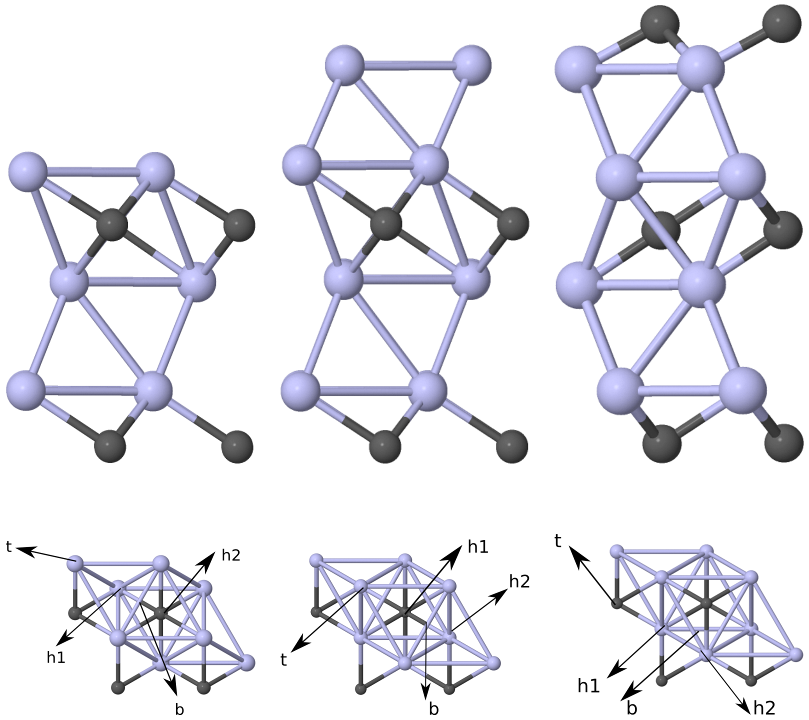

(a) (b) (c)

Figure 3.1: The top panel shows the side view of the 2×2×n (where n=5,6,7) surface slabs, bottom panel corresponds to top views of the mentioned slabs with labeled their adsorption sites. Mo atoms are in blue and C atoms are in grey.

b and t refer to bridge and on=top sites, respectively. In all calculations presented in this chapter, a vacuum layer of at least 14 Å was used in order to minimize interaction between periodic copies of the slabs.

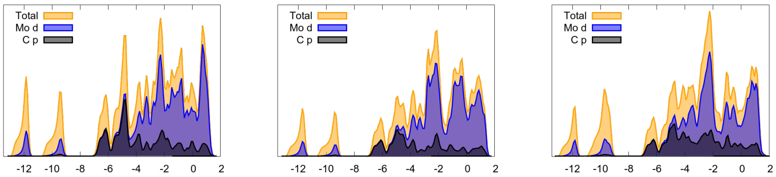

(a) (b) (c)

Figure 3.2: PDOS profiles of the 2×2× n where n is 5,6 and,7 respectively.

The PDOS plots are also shown in Figure 3.2, where the contributions around the Fermi level (zero energy on the x-axis) come from the Mo d and C p orbitals. These slabs do not show noticeable differences in PDOS plotting. Since the Fermi level coincides with nonzero density, all three models are metallic.

3.3.2 Adsorption Energies

The molecular and atomic adsorption energies are calculated on the Mo1, Mo2 and C terminated surface of Mo_2C slab by using the the formula

$$E_{ads} = E_{Mo_2C+adsorbate} - (E_{Mo_2C} + E_{adsorbate}), \tag{3.2}$$

where the first term in the given formula (3.2) represents the total energy of the Mo_2C surface with adsorbate, E_{Mo_2C} term gives the total energy of the clean surface, and $E_{adsorbate}$ is the total energy of the molecule or atom on the surface. With this definition, the stable adsorption energies are negative, thus the higher magnitude is the more stable the configuration is according to our definition.

3.3.2.1 Adsorption Energies of Promoters

In this part, Au, Pt and K atom adsorption is investigated. Binding energy results are used to characterize stable sites on the surface. As the starting configuration, the atoms are placed at a distance of 2 Å on every symmetry site on all three different surfaces namely Mo1, Mo2 and C. In order to obtain the energy of the isolated molecules or atoms for use in (3.2) , a large simulation box is used with cutoff energies as same as the bulk one by choosing the gamma point in BZ.

Table 3.2: Adsorption energies (in eV) and Bader partial charges (in $|e|$) of atomic adsorbates on the two Mo surface terminations and C termination.

	Pt		K		Au	
	E_{ads}	q	E_{ads}	q	E_{ads}	q
Mo1 h1	-5.76	-0.9	-2.18	+0.7	-3.75	-0.6
Mo1 h2	-5.85	-0.9	-2.16	+0.7	-3.80	-0.6
Mo1 t	-4.55	-0.8	-2.12	+0.7	-3.04	-0.5
Mo1 b	-5.85(h2)	-0.9	-2.16	+0.7	-3.80(h2)	-0.6
Mo2 h1	-6.67	-1.1	-2.05	+0.7	-4.32	-0.8
Mo2 h2	-6.53	-1.0	-2.04	+0.7	-3.99	-0.8
Mo2 t	-6.85	-1.1	-2.00	+0.7	-4.39	-0.8
Mo2 b	-6.58	-1.1	-2.05(h2)	+0.7	-4.33	-0.8
C h1	-5.95	+0.3	-3.23	+0.8	-2.48	+0.3
C h2	-4.97	+0.4	-3.05	+0.9	-2.19	+0.3
C t	-3.62	+0.3	-2.80	+0.8	-1.97	+0.3
C b	-5.95(h1)	+0.3	-3.22	+0.9	-2.25	+0.2

The calculated adsorption energies, and the Bader charges for atoms are reported in Table 3.2. First we discuss the Mo terminations. As seen in Table 3.2, for adsorption of Au atom, the most favourable site for the Mo1 termination is the h2 site with an adsorption energy of -3.80 eV, while for the same adsorbate on Mo2 termination, the t site is the most stable site with an energy of -4.39 eV. The binding energies for the Mo2 termination are higher than the case of the Mo1 termination indicating higher stability. A correlation between adsorption energies and the charges on the atoms is observed. The larger the charge transfer from the surface to adsorbate, the higher the adsorption energy is. An interesting observation can be made for Mo1 termination, where during the geometry optimization the bridge configuration tends to go the h1 configuration. Overall, the binding energies for the C terminated slabs are smaller than the Mo type of terminations. Since carbon has higher electronegativity than the Au atom, a charge transfer from adsorbate to surface is expected. As a result, the partial charges on Au atom become positive, enhancing the adsorption energies.

For Pt atom adsorption on the Mo1 termination, the most stable adsorption site is the h2 and the bridge site sharing the same binding energy of 5.85 eV. During the geometry optimization, the initial bridge adsorption sites transforms into another high

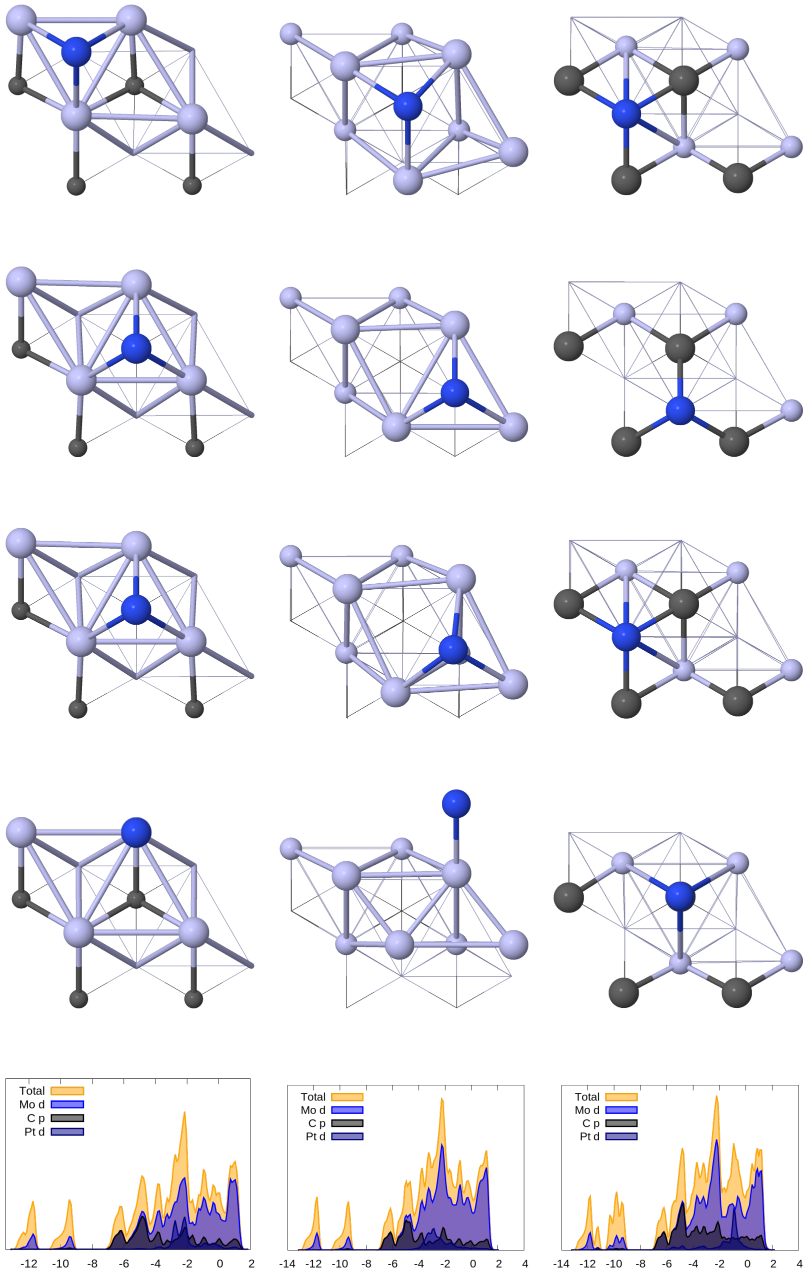
Total
Mo d
C p
Pt d
-12 -10 -8 -6 -4 -2 0 2
Total
Mo d
C p
Pt d
-14 -12 -10 -8 -6 -4 -2 0 2 4
Total
Mo d
C p
Pt d
-14 -12 -10 -8 -6 -4 -2 0 2 4

(a) (b) (c)

Figure 3.3: The first, second and third columns show the top views of Pt adsorption on different adsorption sites namely h1, h2, t and b on the 2×2× n (where n=5,6,7) surface slabs, respectively. The PDOS plotting only corresponds to most stable sites. In the figures, Mo atoms are in blue, C atoms are in grey and Pt atoms are in navy.

symmetry site of h2 as seen in the given Figure 3.3 [1] . The charge transfer from the surface to adsorbate is almost independent of the adsorption sites. The Mo2 termination tends to higher adsorption energy values in line with larger charge transfer from the surface to the Pt atom. The t site is the most preferred site on Mo2 termination with a binding energy of -6.85 eV. The binding energies on C terminated slabs vary between -3.62 eV to -5.95 eV. The most stable sites correspond to h1 and b sites with equal binding energy value. Charge transfer from the adsorbate to surface is observed.

K atom is found to display the most stable configuration on the Mo1 termination in contrast to Pt and Au atoms (Mo2 termination has higher adsorption energies for these atoms.). The most stable site for the Mo1 termination is h1, whereas h1 and b sites are preferred for the K atom on the Mo2 termination. The result is surprising for K atom for the C-terminated slab on which the K atom has higher binding energies when compared to those of Pt and Au atoms. The charge donation from adsorbate to surface is noted in Table 3.2 which is supported by the work of Pistonesi et al. [52]. Additionally, the magnitude of the charge transfer is almost equivalent the that of this study.

3.3.2.2 Adsorption Energy of Atomic Adsorbates of O, C and H

In this part, the adsorption energies of O,C and H atoms are discussed. These atomic species are involved in WGS reaction, therefore to define their binding energies and favourable sites is an important task. These adsorbates are placed above the surface with a distance of 2 Å by using the high symmetry sites on Mo1, Mo2 and C terminations then geometry relaxation is executed. In order to find the energy of the isolated adsorbates in the gas phase, a large simulation cell is employed. All binding energies given in the Table of 3.3 are calculated by using the formula 3.2. The Bader charges on the adsorbates are also given in the same table.

The study of O adsorption reveals that h2 is the most stable site for all different types of termination that we consider. The adsorption energy takes its highest value of -7.85 eV for the case of Mo2 termination and its lowest value -2.57 eV. for the case of C termination with h1 site. As a result of our geometry optimized calculations, we find that the O atom at the bridge site has a tendency to move to the h1 site. For all terminations, the charge transfer direction is from the surface to the adsorbate and their magnitude varies between -0.9 |e| and -1.9 |e|. The maximum charge transfer is computed for C terminated slab with h2, t and b sites.

---

[1] The adsorption energies are higher for Pt atom on Mo_2C surface when compared to the Au and K atoms, therefore the geometry optimized figures are considered only for Pt adsorption.

As seen from the Table 3.3 for H adsorption, the most stable site is site b with an

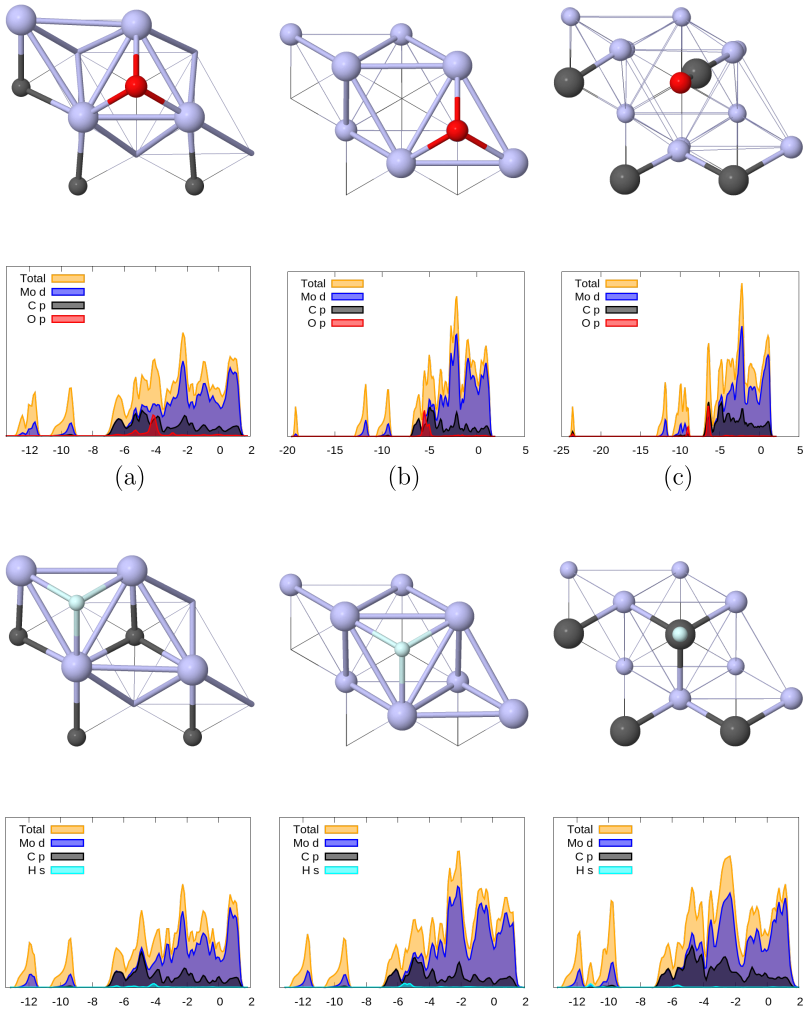

(a) (b) (c)

(d) (e) (f)

Figure 3.4: The top panel shows the top view of the 2×2× n (where n=5,6,7) surface slabs with O atom corresponding to most stable sites, and second row shows their PDOS profiles. Third row represents the top view of the H adsorption on three different terminations with their energetically favourable sites and bottommost panel gives the PDOS profiles of the H adsorption. Mo atoms are in blue, C atoms are in grey, O atoms are in red and H atoms are in turquoise.

adsorption energy of -3.17 eV. for Mo1 type of termination. During the geometry optimization the H atom at site of b tends to go h1 site yielding the approximately same binding energy. The Mo2 terminated slab gives larger binding energies when compared the those of Mo1 type of termination. The most stable geometry is h1 site with binding energy of -3.46 eV. for Mo2 termination.

Table 3.3: Adsorption energies (in eV) and Bader partial charges (in $|e|$) of atomic adsorbates on the two Mo and C surface terminations.

	O		H		C	
	E_{ads}	q	E_{ads}	q	E_{ads}	q
Mo1 h1	-6.52	-1.2	-3.16	-0.6	-7.12	-1.6
Mo1 h2	-6.71	-1.2	-3.02	-0.6	-6.89	-1.6
Mo1 t	-5.41	-1.0	-2.63	-0.5	-4.74	-0.9
Mo1 b	h1	-1.3	-3.17	-0.6	h1	-1.6
Mo2 h1	-7.61	-1.3	-3.46	-0.7	-8.37	-1.7
Mo2 h2	-7.85	-1.3	-3.34	-0.7	-8.22	-1.7
Mo2 t	-6.09	-1.0	-2.11	-0.5	-5.04	-0.9
Mo2 b	-7.79	-1.2	h2	-0.6	-8.42	-1.7
C h1	-2.57	-0.9	-3.15	+0.1	-6.89	-0.1
C h2	-6.48	-1.9	-1.83	0.0	-7.62	-0.1
C t	-4.56	-1.9	-4.15	+0.2	-7.64	+1.8
C b	-4.56	-1.9	h1	+0.1	-7.64	-4.1

There is a charge donation from surface to adsorbate observed generally and the magnitude of the charge transfer is almost equal in between -0.7 eV and -0.5 eV for both Mo1 and Mo2 type terminations. For the C terminated surface, the most stable site is site t yielding the adsorption energy -4.15 eV corresponding also higher charge transfer from adsorbate to surface. This top site geometry on C terminated surface is the most preferred site between the other type of terminations.

Carbon adsorption on Mo1, Mo2 and C terminated surfaces was also examined. The binding energy values for this atomic adsorbate is higher than the values for the other atomic adsorbates, namely O and H. The adsorption of C atom on Mo1 type of termination is vary between the -7.12 eV. and -4.74 eV. The most stable adsorption sites correspond to h1 and b sites sharing the same binding energy value. During the geometry optimization the C atom at bridge sites tends to move towards h1 sites, resulting in identical binding energy. The less stable site is the top site with a binding energy value of -4.74 eV.. The charge transfer direction is always from the surface to adsorbate for Mo1 termination. For the Mo2 type termination, the adsorption energies increases for the sites of h1, h2 and t. The h1 site is found as the most stable site. Again charge transfer is observed from the surface to adsorbate. Except the site t, the C atom on the other three adsorption sites have the same partial charges in magnitude with a value of -1.7 |e|. The adsorption of C atom on C terminated surface is also studied. The t and b sites are most preferential, but the C atom adsorbed at the h2 site also has a binding energy value very close to the t and b sites, which makes this h2 site another preferential adsorption site. The charge transfer from adsorbate to surface is observed only for t site, while the opposite direction for charge transfer happens for the h1,h2 and b sites. One important point for b site is that the charge transfer is very high when compared to the other terminations with different type of symmetrical adsorption sites.

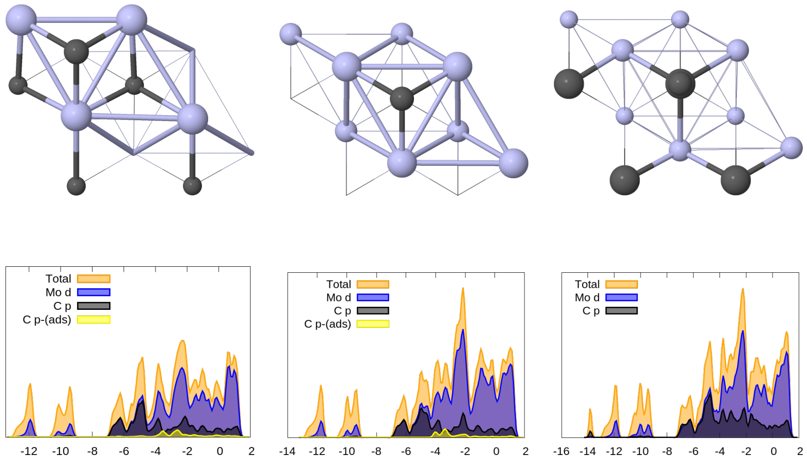

(a) (b) (c)

Figure 3.5: The first row shows the top view of the most stable sites of the C atom adsorption on the 2×2× n (where n=5,6,7) surface slabs with their PDOS profiles given in the bottom panel. Mo atoms are in blue, C atoms are in grey.

The study of O adsorption reveals that h2 is the most stable site for all different types of termination that we consider. The adsorption energy takes its highest value of -7.85 eV. for the case of Mo2 termination and its lowest value -2.57 eV. for the case of C termination with h1 site. As a result of our geometry optimized calculations, we find that O atom at the bridge site has a tendency to move to the h1 site. For all terminations, the charge transfer direction is from the surface to adsorbate and the magnitude of them varies between the -0.9 |e| and -1.9 |e|. The maximum charge transfer is computed for C terminated slab with h2, t and b sites.

3.3.2.3 Adsorption Energy of Molecular Adsorbates of CO, CO_2 and H_2O

CO is an important molecule in WGS reaction, therefore it is crucial to understand that the adsorption energies and partial charges for it on Mo_2C surface. The geometry optimized bond length of free CO molecule is found by using a large cubic cell, which is 1.14 Å. The adsorption energies are examined for all different terminations for all possible adsorption sites towards as was done in the proceeding sections. The CO molecule is placed with the C atom pointing the surface and in a perpendicular orientation.The opposite case is also considered in which O atom pointing the surface. The binding energies are tabulated in Table 3.4 in the last column.

Table 3.4: Adsorption energies (in eV), Bader partial charges (in $|e|$) and bond lengths of CO molecule on the two Mo and C surface terminations.Last column gives the binding energy for the CO molecule in which O atom pointing the surface

	E_{ads}	q	d_{C-O}	E_{ads}
Mo1 h1	-1.86	-0.1	1.20	-0.01
Mo1 h2	-1.50	-0.9	1.19	-0.01
Mo1 t	-2.11	-0.6	1.18	-0.01
Mo1 b	-2.00	-0.8	1.16	-0.01
Mo2 h1	-2.54	-1.1	1.21	-0.01
Mo2 h2	-2.32	-1.1	1.21	-0.02
Mo2 t	-1.90	-0.5	1.21	-0.02
Mo2 b	-2.54	-1.1	1.17	-0.15
C h1	-3.36	-1.4	1.17	-0.03
C h2	-0.13	-0.1	1.16	-0.03
C t	-2.04	-1.4	1.17	-0.03
C b	-0.79	0.0	1.21	-0.03

As seen from the Table 3.4 the adsorption energies are generally larger in magnitude for the Mo2 termination which makes it the most stable termination of CO molecule. The energetically favourable sites are h1 and b sites with the same adsorption energies. For C terminated slabs, the binding energies are considerably decreases all the way -0.79 eV. For both Mo1 and Mo2 terminations, the C-O bond length is slightly elongated when compared to the gas phase value. The values for the bond lengths depend on the adsorption sites for Mo1 terminated surface between 1.16 A° and 1.20 A°. Except for t-adsorption site, the length of the bond on Mo2 termination is larger with values of about 1.21 A°. The elongation of the bonds indicates a weakening of the bond strength and the possible activation of the dissociation of the molecule. The geometry optimized structures of the molecule is presented in the Figure 3.6. As seen in the figure, for h1, h2 and t sites on the Mo1 termination, the CO molecule remains unaltered with making an angle perpendicular to the surface, however the molecule at b site on the same termination is tilted by an angle of 59 A° with respect to the surface plane. The most energetically preferential site is h1 site on the C terminated slab for the CO molecule.The binding energy corresponding this site for the C terminated slab has the highest value between the all sites with different terminations. One noteworthy observation for the CO molecule at h1 site is that it hops to t site during the geometry optimization. The secondary stable site corresponds to t site with a larger adsorption energy of -2.04 eV. The other values for h2 and b sites are significantly lower. The charge transfer direction is always from surface to adsorbates. Additionally, the CO adsorption results are in good agreement with the previous theoretical studies with minor differences [42, 41]. Table 3.4 also shows the adsorption energies for the CO molecule with O-down configuration on Mo_2C surface. There is a significant decrease in adsorption energies that are less than -0.04 eV. The charge transfer is negligible. The bond length remains unchanged after geometry optimization for this type of configuration. We see that the CO molecule initially at b site on Mo2 termination then it drifts to h1 site subjected to geometry optimization process.

The adsorption behaviour of triatomic molecules reveals more complex structure such that their bond length bond angles change with respect to their gas phase. The CO_2 molecule is linear, and both C-O bonds in molecule is 1.17 A° in the gas phase. However, geometry optimized structure of CO_2 molecule on Mo1 and Mo2 terminations is bent as seen in the given Figure 3.7 with bond angles of 136° and 132° respectively. Additionally, the C-O lengths for the case on Mo1 and Mo2 terminations are slightly elongated with values between 1.18 A° and 1.27A °. We do not observe any change in the bond lengths and bond angles for this molecule on C terminated slabs.

According to Table 3.5 the most stable surface is Mo2 type of surface with larger adsorption energies when compared to the other type of terminations. For this stable surface, the most favourable site is h1 with binding a energy value of -1.86 eV and it shares the same adsorption energy with h2 site. During the geometry optimization, b site geometry prefers to move to the place of h1 site. It is worth noticing that CO_2 at top site of Mo1 type of termination unexpectedly dissociates into CO and O as in the Figure 3.7 during the adsorption process. Table 3.5 shows that the contribution of charge transfer from Mo2 terminated surface to CO_2 molecule is much higher than the other type of terminations. The CO_2 molecule on C terminated slabs are also examined, but the binding energies are much smaller. No significant charge transfer is observed for this type of termination.

H_2O is an important absorbent used in the WGS reaction. For the free case of this

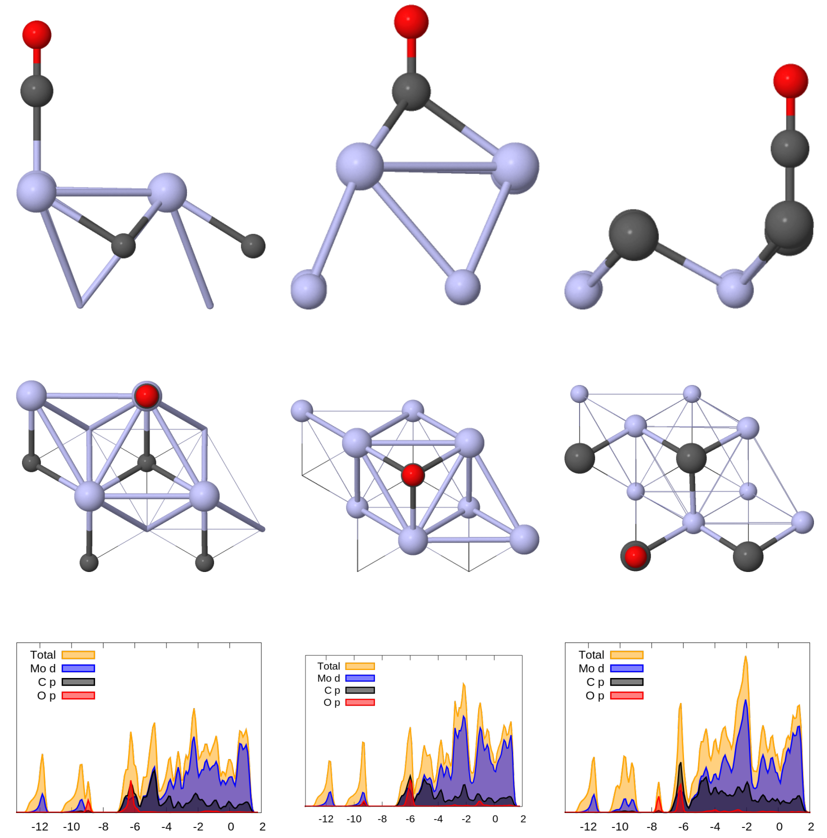

(a) (b) (c)

Figure 3.6: The top panel shows the side top view of the 2×2× n (where n=5,6,7) surface slabs with CO molecule corresponding to stable sites, middle panel shows their top views of the mentioned slabs and the bottom panel shows the PDOS profiles. Mo atoms are in blue, C atoms are in grey, O atoms are in red.

molecule, the optimized bond length between O-H is 0.97 A° and the bond angle is 104.55°. In order to define the energetically favourable sites the H_2O molecule is placed in a parallel orientation over the Mo_2C surface by using the four distinct adsorption sites. Table 3.6 reports the calculated adsorption energies, Bader charges, bond lengths and bond angles. In comparing the binding energies of the Mo1, Mo2 and C terminated surfaces, the Mo2 termination appears to be more favourable. For this termination h2 site is the preferential adsorption site with a binding energy of -0.95 eV C terminated surface is the energetically least favourable termination. As shown in Table 3.6, the H-O-H bonding angle slightly increases for the Mo1 and Mo2 termination and the distance between O-H is almost remains the same, only differing by 0.01 Å. Except for the C terminated surface in which there is no charge transfer observed, all charge transfer direction is from surface to adsorbate.

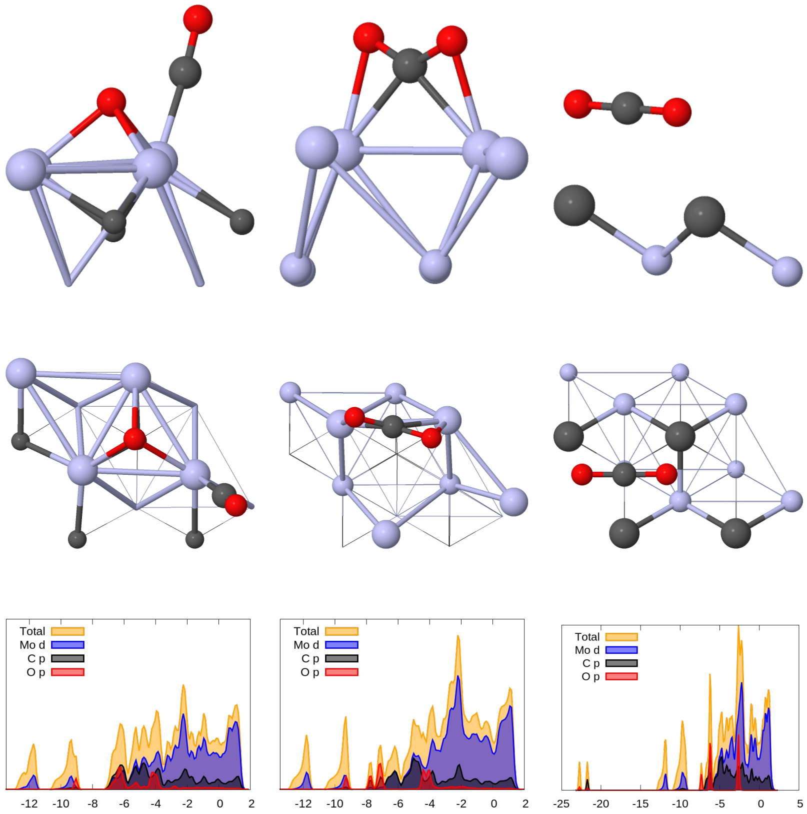

(a) (b) (c)

Figure 3.7: The top panel shows the side of the CO_2 molecule on the 2×2× n (where n=5,6,7) surface slabs ,only considered their most stable places. Second row gives the top view of them. Bottommost one corresponds to PDOS profiles. Mo atoms are in blue, C atoms are in grey, O atoms are in red.

Table 3.5: Adsorption energies (in eV), Bader partial charges (in $|e|$) and bond lengths of CO_2 molecule on the two Mo and C surface terminations.

	E_{ads}	q	d_{C-O}	E_{ads}
Mo1 h1	-1.12	-1.06	1.26 / 1.26	135.6
Mo1 h2	-1.12	-1.06	1.26 / 1.26	135.6
Mo1 t	-1.77	-	1.17 / -	
Mo1 b	-1.12	-1.06	1.26 / 1.26	135.6
Mo2 h1	-1.86	-1.20	1.27 / 1.27	132.6
Mo2 h2	-1.86	-1.19	1.27 / 1.27	132.6
Mo2 t	-1.81	-1.19	1.27 / 1.27	132.6
Mo2 b	-1.85	-1.20	1.27 / 1.27	132.6
C h1	-0.05	-0.01	1.18 / 1.18	180
C h2	-0.05	-0.01	1.18 / 1.18	180
C t	-0.05	-0.01	1.18 / 1.18	180
C b	-0.05	-0.01	1.18 / 1.18	180

Table 3.6: Adsorption energies (in eV), Bader partial charges (in $|e|$) and bond lengths of H_2O molecule on the two Mo and C surface terminations.

	E_{ads}	q	d_{C-O}	E_{ads}
Mo1 h1	-0.81	-0.07	0.98 / 0.98	106.0
Mo1 h2	-0.16	-0.06	0.98 / 0.98	104.3
Mo1 t	-0.81	-0.07	0.98 / 0.98	106.1
Mo1 b	-0.46	-0.11	0.99 / 0.99	110.1
Mo2 h1	-0.89	-0.05	0.98 / 0.98	106.9
Mo2 h2	-0.95	-0.07	0.99 / 0.98	105.6
Mo2 t	-0.80	-0.06	0.98 / 0.99	106.0
Mo2 b	-0.84	-0.11	0.99 / 0.99	112.1
C h1	-0.06	0.00	0.97 / 0.97	104.1
C h2	-0.06	0.00	0.97 / 0.97	104.2
C t	-0.06	0.00	0.98 / 0.98	104.3
C b	-0.06	0.00	0.97 / 0.98	104.3

3.3.3 Coadsorption Energies of the CO molecule with Pt, Au, K

In order to analyze the influence of the alkali promoters and noble metals, coadsorption of CO molecule with these species is investigated. We choose CO as probe molecule, due to its usage in important industrial applications [41]. In order to calculate the binding energies of the CO molecule with these promoter species, we fix the

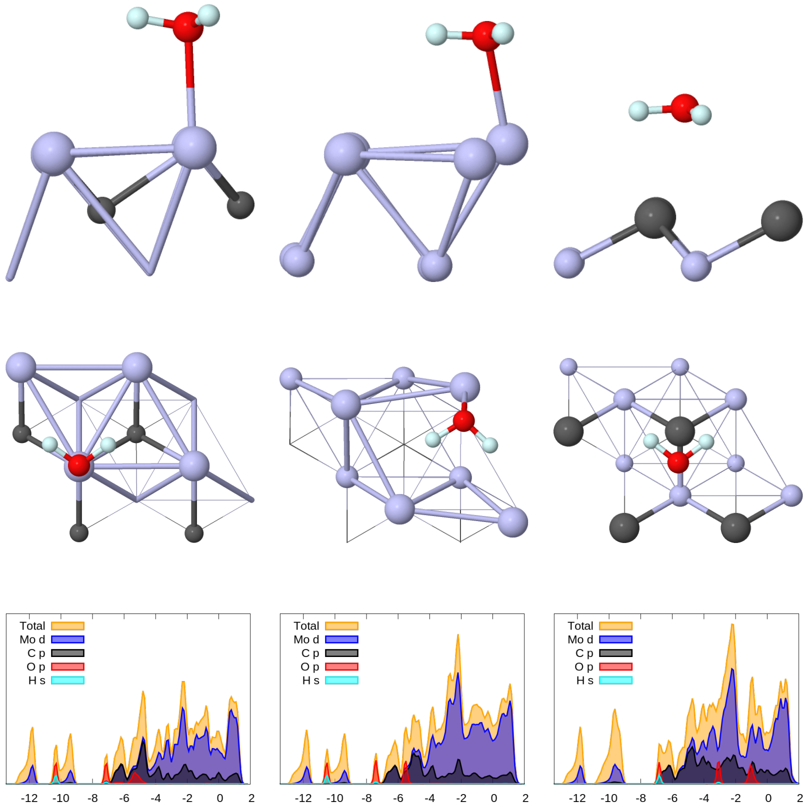

(a) (b) (c)

Figure 3.8: The top and middle panel show the side and top views of the H_2O adsorption on 2×2× n (where n=5,6,7) surface slabs with their most stable sites. Bottom panel corresponds to the PDOS profiles. Mo atoms are in blue, C atoms are in grey, O atoms are in red and H atoms are in turquoise.

location of the Pt, Au, K atoms to their most stable adsorption sites and CO molecule is placed at the neighboring sites by considering the three distinct terminations. We use a different convention in order to distinguish the coadsorption sites. In Tables 3.7, 3.8 and 3.9 the notation is that the slab type is given first with the place of the CO molecule on this slab and the preadsorbed atom in its most stable site on this slab is written to the end with a slash as a separator. As an example, Mo1-h1/Pt-h2 represents the CO molecule at h1 site on Mo1 termination with Pt atom at h2 site which represents the most stable site on Mo1 termination. Mo1-Pt-t/Pt-h2 corresponds to CO molecule at top of the preadsorbed Pt atom on Mo1 termination with Pt atom at h2 site.

The coadsorption energies are evaluated by using the formula,

$$E_{ads} = E_{tot}^{(Mo_2C+Promt+CO)} - (E^{(Mo_2C+Promt)} + E^{CO}) \tag{3.3}$$

where $E_{tot}^{(Mo_2C+Promt+CO)}$ is the total energy of the Mo_2C surface with CO molecule and promoter/alkali atom, $E^{(Mo_2C+Promt)}$ gives the total energy of the Mo_2C surface with promoter/alkali atom which is calculated in previous parts, and the last term defines the total energy of the CO molecule itself. The coadsorption energies for the CO molecule with the Pt atom are given in the Table 3.7. As seen from this Table 3.7, the CO molecule on the h1 site and top site of the Mo atom on the Mo1 terminated surface with Pt atom as promoter gives the largest adsorption energy value. Except for the CO molecule placed on top of the Pt atom, the configurations tends to move towards the top of the Mo atoms which is the most energetically favourable site for this molecule with unpromoted Mo1 terminated slab obtained previously.

Table 3.7: Coadsorption energies (in eV) for CO molecule on the two Mo and C surface terminations with Pt atom as promoter,respectively.

	E_{ads}		E_{ads}		E_{ads}
Mo1-h1/Pt-h2	-2.05	Mo2-h1/Pt-b	-1.92	C-h1/Pt-h1	-1.77
Mo1-h2/Pt-h2	-1.86	Mo2-h2/Pt-b	-1.38	C-h2/Pt-h1	-1.77
Mo1-t /Pt-h2	-2.05	Mo2-t/Pt-b	-1.93	C-t/Pt-h1	-1.75
Mo1-Pt-t/Pt-h2	-1.29	Mo2-Pt-t/Pt-b	-1.04	C-Pt-t/Pt-h1	-1.78

For Mo2 terminated surface with Pt, the largest value of CO adsorption is found for the configuration in which the molecule is on the Mo atom corresponding to a binding energy value of -1.93 eV. The CO molecule at the h1 site also gives approximately same binding energy value of -1.92 eV. In this configuration, CO prefers to reside on the Mo atoms during the minimization procedure. Again CO molecule on the Pt atom gives the smallest binding energy for Mo2 terminated slabs. Carbon termination gives almost same binding energies for the all sites for CO . When comparing the Tables 3.7 and 3.4 which shows the CO molecule adsorption on bare Mo1, Mo2 and C terminated surfaces, binding energies are improved significantly only for the CO molecule on h1, and h2 sites with preadsorbed Pt atom on Mo1 terminated slab. Again considering the same tables, results obtained by using the Pt atom as promoter on Mo2 termination are much lower. However, for C terminated slab with Pt enhances the binding energy of the CO molecule at h2 and CO on Pt atom.

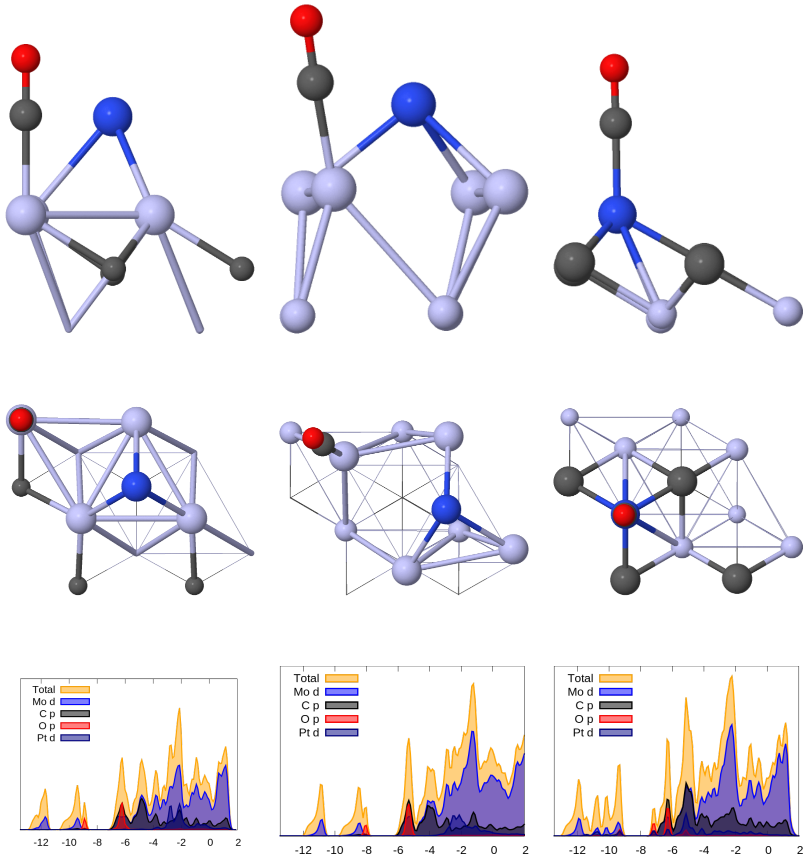

(a) (b) (c)

Figure 3.9: First and second rows give the side and top views of the most stable adsorption sites of the CO molecule with coadsorbed Pt atom on Mo1, Mo2 and C terminated slabs, respectively. The last one shows PDOS profiles of them. Mo atoms are in blue, C atoms are in grey, O atoms are in red and Pt atoms are in navy.

The same calculations were performed for Au atom as promoter which is readily on the on three distinct surface and CO adsorption is examined. The h2 and b sites are the most stable site for Au on atom on Mo1 termination with same binding energy and geometry, therefore we can choose any of the two as a starting point for the Au atom and then place the CO molecule at neighboring sites of it. The Table 3.8 presents the results.

According to Table 3.8 the CO molecule on the Mo1 termination with Au yields similar adsorption energy values. H1 site and atop Mo atom are found as the most preferential sites corresponding to same energy. Additionally these two sites are structurally similar to their configurations during the geometry optimization procedure in which the CO at the h1 site is unstable and migrates to the top of the Mo atom at the

Table 3.8: Coadsorption energies (in eV) for CO molecule on the two Mo and C surface terminations with Au atom as promoter, respectively.

	E_{ads}		E_{ads}		E_{ads}
Mo1-h1/Au-h2	-2.05	Mo2-h1/Au-t	-1.58	C-h1/Au-h1	-1.71
Mo1-h2/Au-h2	-2.02	Mo2-h2/Au-t	-1.74	C-h2/Au-h1	-1.71
Mo1-t /Au-h2	-2.05	Mo2-t/Au-t	-1.69	C-t/Au-h1	-1.74
Mo1-Au-t/Au-h2	-0.50	Mo2-Au-t/Au-t	-0.34	C-Au-t/Au-h1	-1.71

Mo1 termination as seen in Figure 3.10. For the Mo2 termination with Au atom, the adsorption energies of CO molecule are different for each of the sites. The molecule at site h2 has the largest adsorption value that corresponds to the most favourable site, while CO molecule on the Au atom gives the least adsorption energy value. The presence of preadsorbed Au atom on Mo1 termination favors the binding energies of our probe molecule at h1 and h2 sites when comparing the results obtained for bare Mo1 termination presented in Table 3.4. However, Mo2 terminated slab with Au atom leads to decrease in adsorption energies of CO molecule for all binding sites. For the C terminated surface, the binding energy values are improved only for h2 and CO molecule on top of Au atom.

Table 3.9: Coadsorption energies (in eV) for CO molecule on the two Mo and C surface terminations with K atom as promoter, respectively.

	E_{ads}		E_{ads}		E_{ads}
Mo1-h1/K-h1	-2.37	Mo2-h1/K-h1	-2.84	C-h1/K-h1	-2.02
Mo1-h2/K-h1	-2.39	Mo2-h2/K-h1	-2.80	C-h2/K-h1	-0.27
Mo1-t /K-h1	-2.37	Mo2-t/K-h1	-2.89	C-t/K-h1	-2.03
Mo1-Au-t/K-h1	-2.09	Mo2-K-t/K-h1	-0.09	C-K-t/K-h1	-0.08

The coadsorption energy calculations of the CO molecule on Mo1, Mo2 and C terminated slabs with K atom are also studied. The values are depicted in the Table 3.9. According to these results, CO molecule at h2 site gives the largest adsorption value of -2.39 eV on Mo1 termination. Additionally, the configurations of CO on h1 and t sites share the same binding energies which is very close to the value obtained for the h1 site, indicating that these places can be considered as the secondary favourable sites. Same table also gives the adsorption energies for Mo2 terminated slab with preadsorbed K atom. The results show that the molecule at t site yields the largest

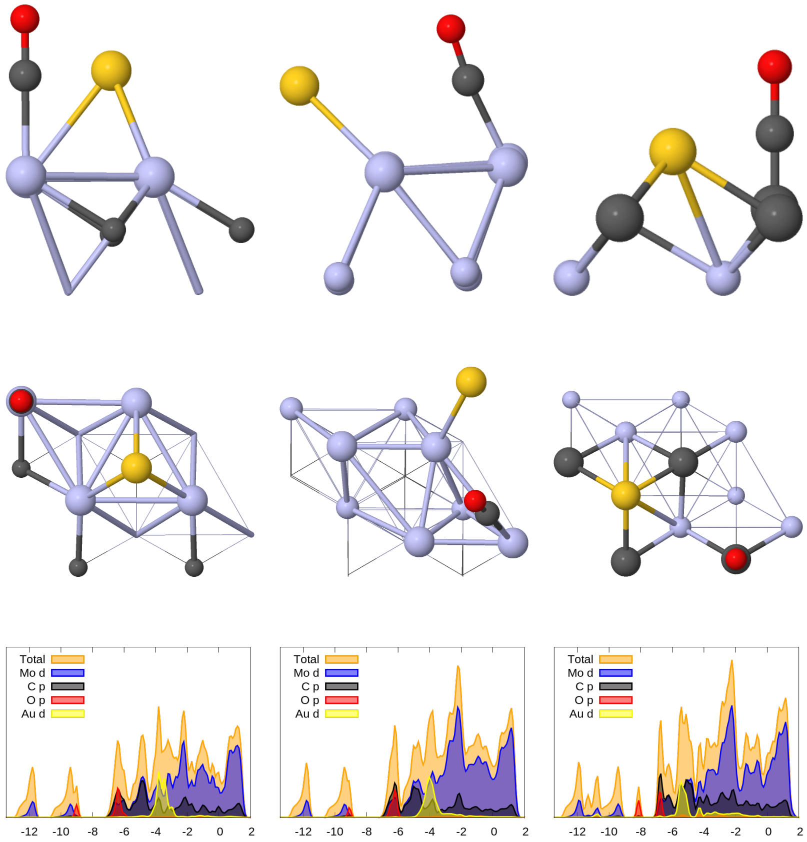

(a) (b) (c)

Figure 3.10: First and second rows give the side and top views of the most stable adsorption sites of the CO molecule with coadsorbed Au atom on Mo1, Mo2 and C terminated slabs, respectively. The last one shows PDOS profiles of them. Mo atoms are in blue, C atoms are in grey, O atoms are in red and Au atoms are in yellow.

binding energy value. The configuration of CO molecule at t site of K atom on the same termination produces the lowest adsorption value of -0.09 eV when compared to other sites. For C terminated slabs, the energetically favourable site corresponds to CO molecule at t site with adsorption energy value of -2.03 eV that is almost equivalent result to that computed for the h1 site. K atom as promoter improved the binding energies of the CO molecule when comparing the two Tables 3.9 and 3.4 for all binding sites at Mo1 termination. Similar results are observed for Mo2 terminated surfaces.

It is worth noting that the adsorption energy values with K atom as an alkali promoter are much larger than the values calculated for Pt and Au atoms.

3.3.4 Dissociative adsorption of CO on Mo_2C surface

In this section, the effects of the promoters and noble metals on the activation barriers of the CO dissociation is examined. This reaction is only considered for the Mo1 terminated slab due to higher co-adsorption energies for species in the presence of Pt, Au and K. The common thought related to transition metal carbides is that they are active catalysts for many chemical reactions without the need of any promoters stated in the introduction part. In order to see the effects, we try to test it through the NEB calculations.

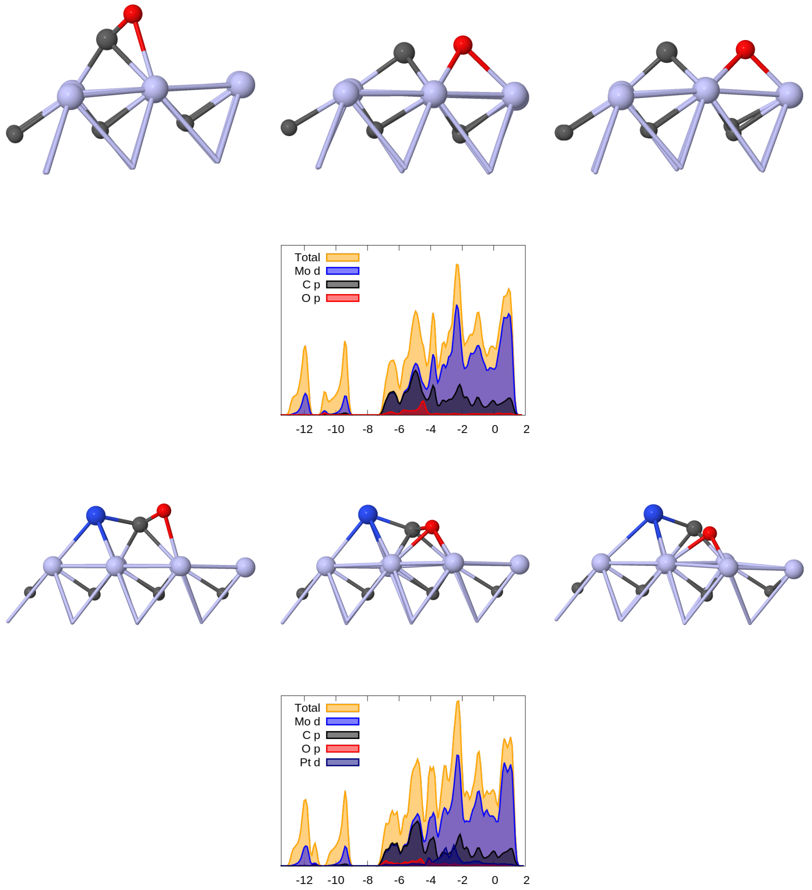

initial transition final

Figure 3.11: CO dissociation profile for bare surface and Pt promoted surface. The first and second rows are initial, transition, final states of the reaction the bare surface and PDOS profile of the reaction in transition state. The third and fourth rows are initial, transition, final states of the reaction the Pt promoted surface and PDOS profile of the reaction in transition state. Mo atoms are in blue, C atoms are in grey, O atoms are in red and Pt atoms are in navy

We use 2x3x5 slab geometry which has a large surface area for the adsorbates to bind for studying the dissociation mechanism properly. Table 3.4 shows that the CO molecule strongly binds at the t site on the Mo1 termination with the value of -2.11 eV. This molecule dissociates to C and O atoms and, their favourable adsorption sites are considered during the NEB calculation. The dissociation starts with the CO molecule in a tilted position on the clean unpromoted surface as in the given Figure 3.11 and the activation barrier of this reaction is found as 2.01 eV. This result is good agreement with a study of Wang et al. [46]. In the transition state as depicted in the Figure 3.11, CO molecule remains almost parallel to the slab, and the bond length is 1.80 Å, which is larger than the value of the gas phase. The C and O atoms reside at their energetically favourable sites at the final state on the Mo1 termination. In order to observe the effect of the promoters on the catalytic activity, the CO dissociation is studied on the same terminated slab with Pt atom as promoter. The activation barrier is 1.74 eV with Pt atom indicating that it enhances the dissociation. The PDOS analysis and Bader charge calculations are investigated for transition states to understand the decrease in the activation barrier. According to PDOS analysis given in the Figure 3.11 , the d-states of the Pt atom hybridized with d-states of the Mo atom around the -2 eV and -4 eV weakens the bonding between the CO and Mo terminated surface, which is attributed to the decrease in activation barrier. Additionally, the CO molecule has a total of -2.10 |e| charge without promoter atom during dissociation, while in the presence of a promoter atom, a decrease is observed for the electronic charge of CO molecule giving -0.26 to Pt atom, which favors the dissociation process. The same calculations are considered for CO dissociation with Au and K atoms.

An interesting observation for K is that the activation barrier for dissociation of CO is calculated as 1.57 eV which is lower than both bare and Pt promoted surface. This result is attributed to the better stabilization of the transition state of reaction with K as promoter when compared to the others given in the Figure 3.12. The PDOS profile of the transition state again in the same Figure 3.12 for the reaction with K does not show any strong hybridization of K orbitals with the other atoms therefore hybridization is not the reason of the lower value of the reaction energies. During the dissociation process , K atom starts to make bonds with C and O atoms when these atoms reside at their stable sites on the surface. The bond lengths for C-K and O-K are 2.97 A° and 2.63 A°,respectively, whereas the C-O bond is elongated to the value of 1.91 A° which is larger than the gas phase value. The elongation of the C-O bond is characteristic of the transition state of both K and Pt promoted surfaces. .The effect of the Au atom as promoter is also examined but the reaction energy is 2.07 eV which is larger than the other promoted surfaces. In the final state, in the case of K and Pt promoted surfaces; the C and O atoms are sit their stable sites. However for the Au-promoted surface, C and O atoms do not reside at their stable sites, which can be attributed to larger value in reaction barrier.

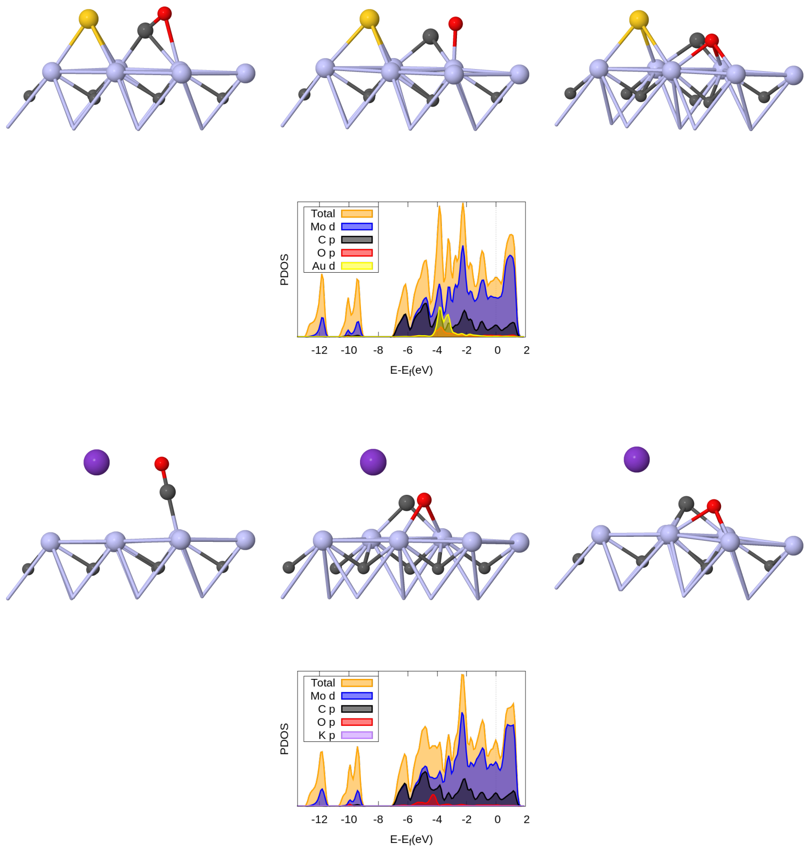

initial transition final

Figure 3.12: CO dissociation profile for Au and K promoted surface. The first and second rows are initial, transition, final states of the reaction Au promoted surface and PDOS profile of the reaction in transition state. The third and fourth rows are initial, transition, final states of the reaction the K promoted surface and PDOS profile of the reaction in transition state.Mo atoms are in blue, C atoms are in grey, O atoms are in red, Au atoms are in yellow and K atoms are in violet.

3.3.5 H_2 formation on Mo_2C surface with and without promoter

In order to evaluate the activation barrier and corresponding transition states for the reaction of

$$H + H \longleftrightarrow H_2 \ (1.2)$$

on the Mo1 type of termination, the NEB method is applied by using the most stable sites for reactants and products obtained from previous parts. This reaction proceeds in two stages on Mo1-terminated surface. We first observe that H atoms make bonds with a Mo atom as in the Figure 3.13, then a scission of these bonds occurs and the reaction ends with production of H_2. The activation barrier for the first step of the reaction is found as 1.04 eV whereas for the second is 0.83 eV. The former, having a higher activation barrier, limits the reaction rate. The influence of the Pt atom as promoter on the reaction is also examined by placing it on the surface and by using it as a dopant. When Pt atom is placed on the surface, the reaction again takes place in the same two steps and we observe a significant decrease in the activation energy of the first step by 0.83 eV, which is the limiting step for the case without promoter. However, the activation energy of the second step increases slightly to 0.81 eV with the usage of Pt on the surface and the two activation energies for the steps of the reactions become comparable. When Pt atom is used as a dopant in which one of the Mo atom is extracted and it is replaced with Pt atom; we do not observe a two-step mechanism and H_2 molecule is formed directly out of two atoms with the activation energy of 1.29 eV. Therefore, we conclude that our results favor the usage of Pt as a dopant for H_2 molecule formation.

3.4 CONCLUSION

In this section, the binding energies of the atomic adsorbents of O, C, H, Pt, Au, K and molecular ones of CO, CO_2, and H_2O are examined by using the three distinct terminations namely Mo1, Mo2, C terminations of the Mo_2C. Moreover, the calculation of partial charges on these species are computed.

The Mo2 termination is found as most stable termination for CO molecule. The bond length of CO molecule is elongated upon adsorption for all terminations indicating

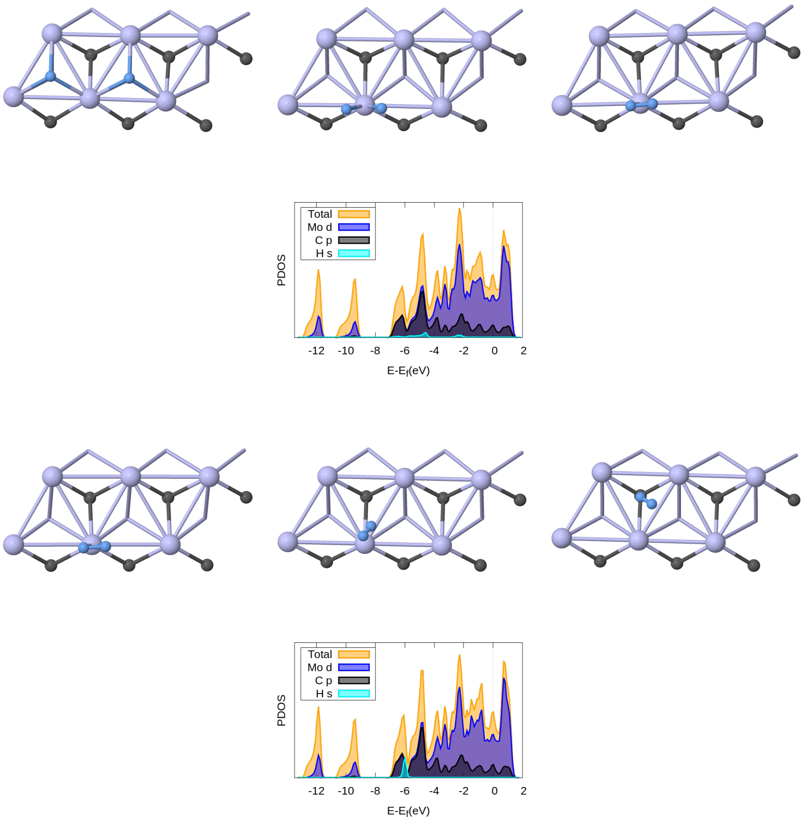

initial transition final

Figure 3.13: H_2-formation first and second steps without using promoter and dopands

a weakening of the bond strength. The adsorption of of CO_2 molecule reveals more complex structure. The gas phase of CO_2 molecule is linear therefore, it is placed as parallel on top of the surfaces. However, the geometry optimized structure of CO_2 molecules are bended and the all bonds in the molecule are lengthened for Mo1 and Mo2 terminated slabs. On the other hand, no change is observed for C terminated surfaces in the bonding length and bond angle. The binding energies for this adsorbent on C terminations are much smaller when compared to the other terminations. The Mo2 termination appears to be more favourable for H_2O adsorption. The bonding angles are slightly opened on Mo1, Mo2 terminations whereas the bonding lengths remain same. For all atomic and molecular adsorbents gain electron from the Mo_2C substrate except K atom.

In addition to these, the CO molecule is chosen as a probe molecule and the coadsorption energies of it with preadsorbed Pt, Au, K atoms are studied. After having

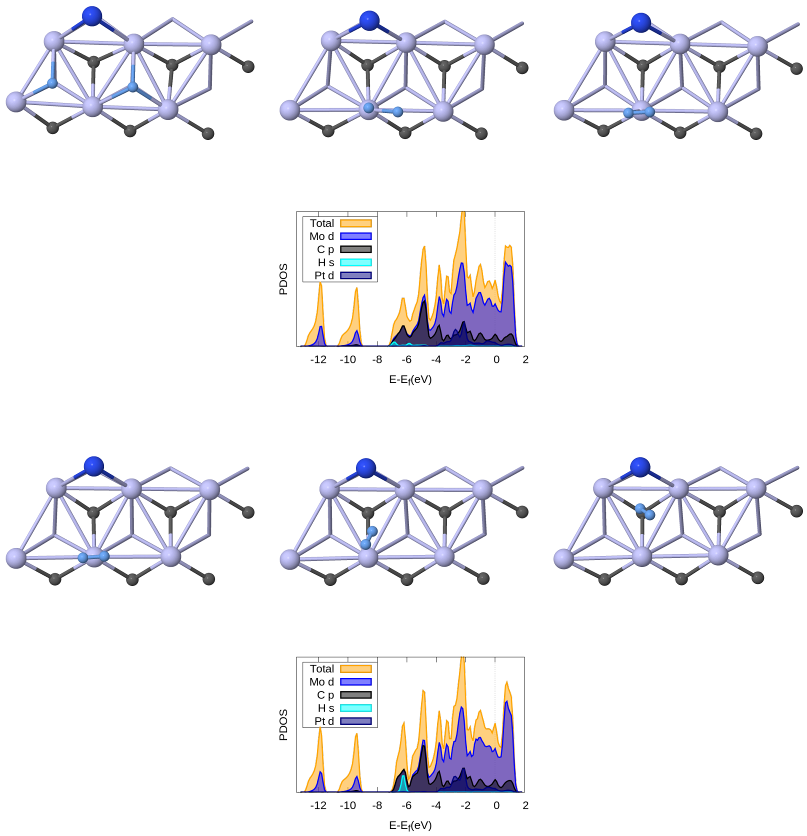
Total
Mo d
C p
H s
Pt d
PDOS
-12 -10 -8 -6 -4 -2 0 2
E-E$_f$(eV)
Total
Mo d
C p
H s
Pt d
PDOS
-12 -10 -8 -6 -4 -2 0 2
E-E$_f$(eV)

initial transition final

Figure 3.14: H_2-formation fist and second steps with promoter

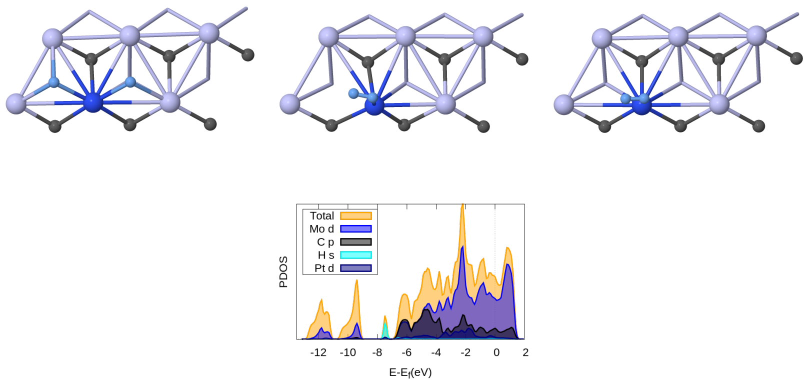
Total
Mo d
C p
H s
Pt d
PDOS
-12 -10 -8 -6 -4 -2 0 2
E-E$_f$(eV)

initial transition final

Figure 3.15: H_2-formation fist and second steps without using promoter and dopant

obtained them, the dissociation of CO molecule is investigated by performing NEB method in order to calculate activation barriers. With this aim, first, the dissociation energy was worked out on bare surface with additives, which are Pt, Au, K . We consider only Mo1 terminated slab for computing the energy barriers. Mo2 and C terminated slabs do not need to be used in such calculations, due to the fact that these terminations with mentioned additives do not favor the adsorption energies of the CO molecule when compared to Mo1 termination.

The dissociation barrier is found as 2.01 eV on clean unpromoted surface. In order to examine the influence of the promoters on the catalytic activity, we study the same reaction with promoted surfaces. The promoter used in this reactions are Pt, Au, K. The activation barrier is 1.74 eV with preadsorbed Pt atom indicating that it improves the activation. This result is ascribed to that hybridization of the d states of the Pt with d states of Mo atoms on the surface according to PDOS results. Same calculations are considered for CO activation with Au and K. The energy barrier is calculated as 1.57 eV which is even lower than Pt promoted surface. The better stabilization of transition state for the slab with K results in decrease in barrier. Finally the reaction barrier is found as 2.07 eV with Au additive, which is larger than case of bare and Pt, K promoted slabs.

CHAPTER 4

EFFECT OF THE PLATINUM AS DOPANTS ON METHANOL DEHYDROGENATION ON THE GOLD SURFACES

4.1 Introduction

When alcohols are exposed to oxygen, a combustion reaction takes place, giving rise to CO_2 and H_2O. Combustion reactions produce industrially valuable chemicals such as esters, ketons, carboxylic acits and aldehydes which are widely used in food, polymer, pharmaceutical industries. Being one of the several intermediate steps in combustion reactions, selective oxidation provides a way to interrupt the reaction at the desired level to extract the product of interest. The size and variety of such products is highly dependent on the environment and the catalyst used. It was experimentally demonstrated that selective oxidation process is catalyzed by metal surfaces. In this chapter, methanol (CH_3OH) is used as a representative molecule due to its basic structure and valuable side products in the oxidation process. During the oxidation of the CH_3OH molecule, depending on the reaction conditions, O-CH_3, ester, methylformate, CH_2O and similar products can be obtained. These side products in turn react amongst each other or with the parent alcohol to produce new other species. As a result, the variety and size of the products are increased. This phenomenon is called as self-coupling.

The adsorption and decomposition of the CH_3OH molecule on coinage metals have been studied in great depth due to its enormous use in industry. This method can be utilized in internal combustion engines when CH_3OH is mixed with petrolium source. It has a great potential as hydrogen source for fuel cells. Additionally, it is used as a feed stock for the production of many chemicals.

In consequence of all these advantages of CH_3OH, the study of adsorption, decomposition process and its reaction with catalysts have become important. The CH_3OH has three kinds of bonds namely C-H, O-H and C-O, which makes the decomposition process to proceed via a variety of pathways. One group of studies consider the adsorption and decomposition of CH_3OH on many surfaces only regarding the initial type of bond scission. C. J Zhang and co-workers investigated the CH_3OH decomposition pathway on Pd(111) through the O-H and C-O bonds breaking by first principle techniques [61]. They studied the two reaction pathways separately by calculating the activation barrier for the former case in which CH_3OH decomposes to CH_3O and H and the latter case in which it composes to CH_3 and OH. They found that the initial O-H bond scission, with lower activation barrier, was more favorable than the C-O bond scission for the relevant reaction. Besides methanol, ethanol can be used in many important applications in industry. One study by Lie et al. presents the ethanol decomposition on Pd(111) surface by DFT calculations [62]. They observe that the energy barriers are gradually decreased going along the decomposition pathway for the scissions of C-C, C-H and O-H bonds, respectively . Another similar study by Cui-Yu Niu et al. was related to the reaction mechanism of CH_3OH decomposition on different type of Pt based catalysis [63]. In their work, all possible CH_3OH dissociation pathways mentioned above were examined in detail by calculating the energy barrier. These calculations revealed that CH_3OH decomposes via O-H bond breaking with lower activation barrier than the other reaction pathways namely C-H and C-O bond scissions. Another similar study investigates the complete decomposition of CH_3OH over Pt(111) surface via O-H bond scission [64]. In this study, the adsorption energies of CH_3OH, CH_3O and CH_2O and other such molecules and atoms involving in this reaction are calculated to define the most stable sites. The construction of initial and final geometries are chosen for reactants according to stable configurations determined in this manner. They first examine the reaction path of decomposition of CH_3OH to CH_3O and H followed by sequential abstraction of H atom from CH_3O molecule resulting in many intermediates which are also analyzed. Similarly, a DFT study examined the CH_3OH decomposition over Pt(111) surface [65]. They consider two kinds of initial decomposition path which are C-H and O-H bonds breaking. The binding energies of the resulting intermediates, depending on which type of bond breaks, are calculated to define their favorable sites by regarding their coverages on the surface. They found that CH_3OH molecule weakly bonds to the surface through van der Waals interaction when compared to other intermediates such as hydroxymethyl, methoxide etc.. Their results suggest that the activation of C-H bond breaking are more favorable than the O-H bond breaking. Additionally, they found that the cleavage of C-H bond reactions are exothermic, while the O-H bond breaking reactions are endothermic.

Gold in bulk form had been considered as chemically inert metal till Haruta et al.demonstrated that CO oxidation was enhanced by Au nanoparticles at low temperatures [66]. After this study, Au has attracted great interest as a catalyst in many reactions including WGS reaction [67], selective oxidation of alcohols [68, 69, 70], and hydrocarbons [71]. Many studies have been conducted on Au based catalysts due to their activity and selectivity at lower temperature. The first experimental study by Koel and his team showed that selective oxidation of methanol molecule on clean and oxygen precovered Au(111) surfaces under ultra high vacuum conditions [72]. Interestingly, it is experimentally known that the decomposition of methanol molecule is not observed at cyrogenic and even elevated temperatures on clean coinage metals [73, 74]. However, on surfaces precovered with O add atoms, methanol dissociates through O-H and C-H bond breaking during heating [75, 76, 77, 78]. Both experimental and theoretical studies suggest that precovered oxygen on the gold surface activates the hydrogen in the hydroxyl group in alcohols [79, 80, 81]. Gold-supported catalysts enhance the oxidation of alcohols resulting in the production of carbonyl like chemicals. This is an environmentally friendly process which can replace the usage of heavy metal salts as oxidising agents [82]. There is ongoing interest for the process of oxidation of alcohols in order to reduce the energy waste, to diminish the production of environmental pollutants in recent years. Gold based catalysts are a promising candidate in this process.

A study by Chen et al. investigates the adsorption and dissociation of methanol on clean Au(111) surfaces based within the periodic DFT framework. They first calculate the adsorption energies of the molecules of methanol, methoxy, formaldehyde by considering their Mulliken charges and vibrational frequencies. A detailed analysis of adsorption characteristics reveal that methanol and formaldehyde are weakly bonded to the surface whereas the methoxy has higher adsorption energy. The possible dissociation path is initiated by O-H bond scission in order to form the CH_3O, followed by O-C bond breaking to produce HCHO. This is the final step of the reaction that is found as the rate determining of the decomposition process. HCHO was found to be the main product of CH_3OH oxidation [83]. Another very similar study conducted by Wang and his co-workers examine the methanol dehydrogenation on O and OH covered Au(111) surface [84]. They compare the activation energies obtained on O and OH covered surfaces with the those on clean Au(111) surface. Two dissociation pathways are investigated. The first decomposition pathway proceeds via the O-H bond cleavage and the corresponding calculated energy barrier is 2.00 eV. The second pathway involves the C-H bond scission with an energy barrier of 2.20 eV. In addition, the adsorption energies of CH_3OH molecule is found to increase with precovered O atom. Furthermore, in the presence O atom, the activation barrier for methanol dissociation was observed to decrease to 0.27 eV. Other reaction steps in the complete decomposition process were also analyzed by means of calculating the activation barriers for various coverages of atomic O which is readily on the surface. Hussam and his team study the CH_3OH adsorption and dissociation on Au(100) and Au(310) surfaces by DFT [85]. They also consider the presence of the O atom on the O-H and C-H bond scissions of the CH_3OH molecule. Both Au(100) and Au(310) were found to be incapable of CH_3OH and CH_2O adsorption and dissociation when surfaces are clean. However, CH_3OH was seen to decompose to CH_3O and OH easily on the surfaces in the presence of O atoms. The general conclusion that can be drawn from this substantial body of work is that O adatoms play a crucial role in the activation of alcohols.

However, the decoration of clean Au surfaces with atomic oxygen is not an easy task. The side products are toxic for the environment and the procedure is cost. Hence, in this chapter, we explore the potential promoting effect of Pt atoms in different concentrations in order to decrease the reaction barrier of the decomposition of the CH_3OH molecule without using O on the surfaces. The adsorption energies of the all molecules and atoms, which are CH_3OH, CH_3O, OH, O, H, are calculated on Pt-doped Au(111) surfaces in order to define the most stable adsorption sites. Once the most likely geometries of the reactants and products are identified, the activation energy calculations are performed for slabs with different doping concentrations.

4.2 Computational Details

All DFT calculations were performed using the Quantum Espresso simulation package [47]. The generalized gradient approximation (GGA) of Perdew-Wang(PW-91) exchange correlation functional was used for calculation of the energies and geometries [23]. The BZ of the gold surface was sampled by Monkhorst-Pack of 4x4x1 k-point mesh [26]. The kinetic energy cut-off for the planewave functions and for charge density were 40 Ry and 400 Ry, respectively. The criteria for convergence of the force threshold was set 0.001 eV/A°. In order to reduce the interactions between the successive slabs, a vacuum layer is set to be 14 A° . The charges on the adsorbate and surface are defined by the Bader charge analysis [50, 51] . The Nudged Elastic Band (CI-NEB) [30] calculation was performed to obtain activation energies for reactions and to define transition states. The XCrysden and Jmol programs were used for visualization of the figures.

4.3 DFT Calculations

4.3.1 Bulk Structure and the (111) Surface of the Au Crystal

Au has a face centered crystalline structure with a lattice parameter of 4.08 A° [86]. In order to obtain theoretical value of the lattice constant, total energies are calculated by single point DFT calculation as a function of various lattice constants. The theoretical lattice constant corresponding to minimum of these energies is 4.16 A° with an error 1.96 % with respect to the experimental value.

The (111) surface of Au is constructed as a slab model by using 3x3 unit cells and four layers in ABCABC... stacking . The two layers at the bottom are held fixed, while the others are allowed to relax during the geometry optimization to mimic the bulk behavior. There are several adsorption sites on the Au(111) surface namely, fcc hollow, hcp hollow bridge and on top sites. The bridge site connects the fcc and hcp hollow sites. The on-top site, as the name implies, is the top of the any Au atoms. These high symmetry adsorption sites are summarized in Figure 4.1.

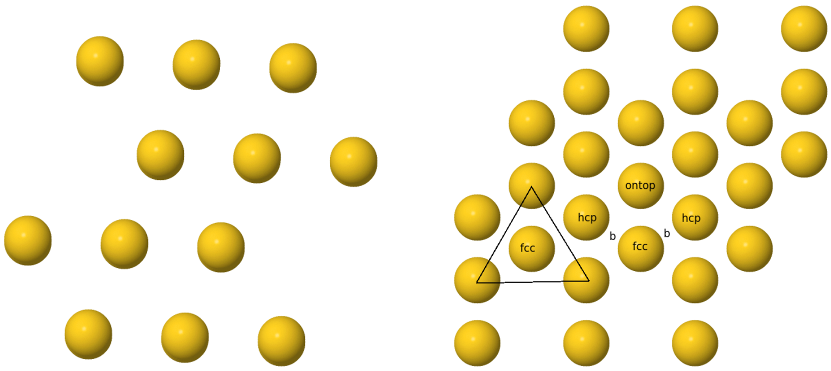

(a) (b)

Figure 4.1: The side view (a) and the top view (b) of the 3x3x4 surface slab of the Au. The labels on the right figure represents the different adsorption sites on the Au surface.

4.3.2 Adsorption Energy Calculations

The adsorption energies for CH_3OH, CH_3O, OH molecules, H and O atoms are calculated by using the formula,

$$E_{ads} = E_{Au+adsorbate} - (E_{Au} + E_{adsorbate}) \tag{4.1}$$

where $E_{Au+adsorbate}$ is the total energy of the surface with adsorbate, E_{Au} is the total energy of the gold surface only, and the last term represents the total energy of the adsorbate in gas the phase. In order to obtain the energies of the gas phase of molecules and single atoms, we use a large simulation box and conduct BZ integration at the γ point while keeping all other calculation parameters the same. According to our definition, the more negative the adsorption energies the more stronger adsorption. After obtaining the binding energies for bare surface, we also examine the effect of the Pt atom as a surface dopant on the binding energies. First the binding energies are calculated on the Au(111) surface with a single substitutional Pt dopant, then the number of dopant atoms are increased to two and three. Finally, to gain more insight into the optimum amount of Pt needed, the top layer and the sublayer of the top layer is fully doped with Pt atoms, and the adsorption energy calculations are repeated.

4.3.2.1 Adsorption Energies of the CH_3OH on the clean and Pt-doped Au (111) surface

As described above sections, the decomposition of CH_3OH on the Au surface takes place through the O-H bond scission to CH_3O and H, hence adsorption of this molecule is first investigated on the bare surface to define the stable sites. With this aim, the molecule is placed on the clean surface by considering four distinct adsorption sites. The calculated adsorption energies are given in Table 4.1 and geometry optimized structure with PDOS profiles for the most stable sites are given in the Figure 4.2. One can see from this table that CH_3OH is weakly bound to the Au surface and the binding energies for all sites are almost the same, implying that all sites are equivalent. These results are in good agreement with the previous works [84, 83]. However, the hcp hollow site is used as a reference stable site [87] for our activation barrier calculations. There is no significant change observed in the bond lengths of the C-H, O-H and C-O bonds in the adsorbate.

Table 4.1: Adsorption energies (in eV) of molecular adsorption of the CH_3OH on bare Au(111) and surface and Au(111) surface with different magnitude of dopant atoms of Pt.

	Au	Au/Pt	Au/2Pt	Au/3Pt
hcp-hollow	-0.10	-0.11	-0.13	-0.14
fcc-hollow	-0.09	-0.12	-0.13	-0.13
bridge	-0.10	-0.10	-0.12	-0.13
ontop	-0.11	-0.12	-0.13	-0.27

The effect of the the substitution of the Pt atom at different concentrations on adsorption energies is also examined. For this study, one of the surface Au atom is extracted from the topmost layer and replaced by Pt. The same operation is employed for two and three Pt atoms. The slabs with different amount of doped atoms are referred to as Au/Pt, Au/2Pt, and Au/3Pt, respectively. The surfaces prepared in this manner with the adsorbed CH_3OH molecules can be seen in Figure 4.2. The adsorption energies are calculated once again using the same formula of 4.1. The results shown in Table 4.1 states that CH_3OH is adsorbed weakly but there is a slight increase in binding energies when the number of the dopant atoms is increased. Again the bonds in CH_3OH

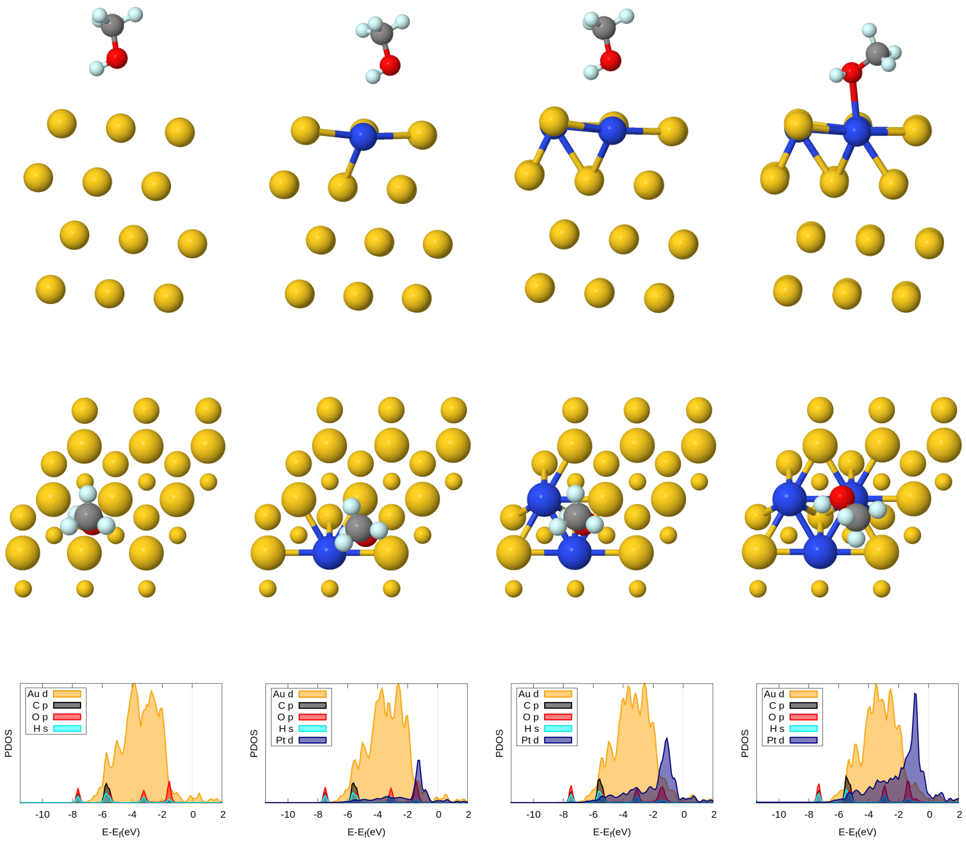

(a) (b) (c) (d)

Figure 4.2: The first row represents the side view of the adsorption of CH_3OH molecule on bare, Au/Pt, Au/2Pt and Au/3Pt surfaces. The second row shows same for ontop views. The last row represents the corresponding PDOS profiles. In the figures, Au atoms are in yellow,H atoms are in turquoise, C are in grey and O atoms are in red.

remain almost the same after geometry optimization.

The Table 4.2 presents the adsorption energies of CH_3O and H. The adsorption energies for CH_3O on the bare surface is relatively high when compared to case of CH_3OH, and the fcc site is the preferred site. Pt atom as dopant has no significant effect on the adsorption energies of CH_3O. For the H atom, the adsorption energies are high and the presence of the Pt atoms improves the adsorption energies to some extent. The binding energies calculated for hcp and fcc are also very close to each other indicating that both sites can be used as final states in the NEB calculations. The same observation is seen for the surface with different magnitude of Pt atom.

Table 4.2: Adsorption energies (in eV) of molecular adsorption of the CH_3O and H atom on bare Au(111) and Au(111) surface with different concentrations of dopant atoms of Pt.

	CH_3O				H			
	Au	Au/Pt	Au/2Pt	Au/3Pt	Au	Au/Pt	Au/2Pt	Au/3Pt
hcp-hollow	-1.70	-1.88	-1.87	-1.85	-3.15	-3.45	-3.74	-3.84
fcc-hollow	-1.75	-1.73	-1.70	-1.91	-3.18	-3.45	-3.74	-3.83
bridge	-1.67	-1.87	-1.87	-1.85	-3.13	-3.46	-3.74	-3.84
ontop	-1.69	-1.66	-1.58	-1.92	-3.01	-2.98	-2.99	-3.65

Many studies have been conducted by considering the effect of the precovered O atom on Au surface on the dissociation of CH_3OH which is previously stated. These studies reveal that O atom which is readily on the surface have a positive effect on the high activation barrier making it to hope easily. Hence, the O atom and OH molecule, formed by precovered O atom and H atom coming from CH_3OH activation, as they are important species in the oxidation process, adsorptions are elucidated also. Table 4.3 , as being below , reports the adsorption energies of both O and OH molecule on bare and doped surfaces, respectively. The O atom tends to favor both bridge and fcc sites with same adsorption energy value of 5.07 eV. At these sites, O makes a bond with surface atoms with an average bond length of 2.13 A°. A modest increase is observed for binding energies of O atom in the presence of Pt atoms, which however has no impact upon the place of the most favorable sites.The magnitude of the increase approximately correlates with Pt concentration, but always remains under 0.4 eV. The OH molecule prefers to anchor on fcc adsorption site through its O atom with a larger energy value of -2.66 eV on the bare surface when compared to other adsorption sites. As shown in Table 4.3, similarly to the case of O and OH adsorption energy increases with Pt coverage. The Figure 4.4 gives the most stable adsorption of the O and OH with PDOS profiles. We conclude from the PDOS plots that the energy of the d states of the Pt atom approaches towards the Fermi level.

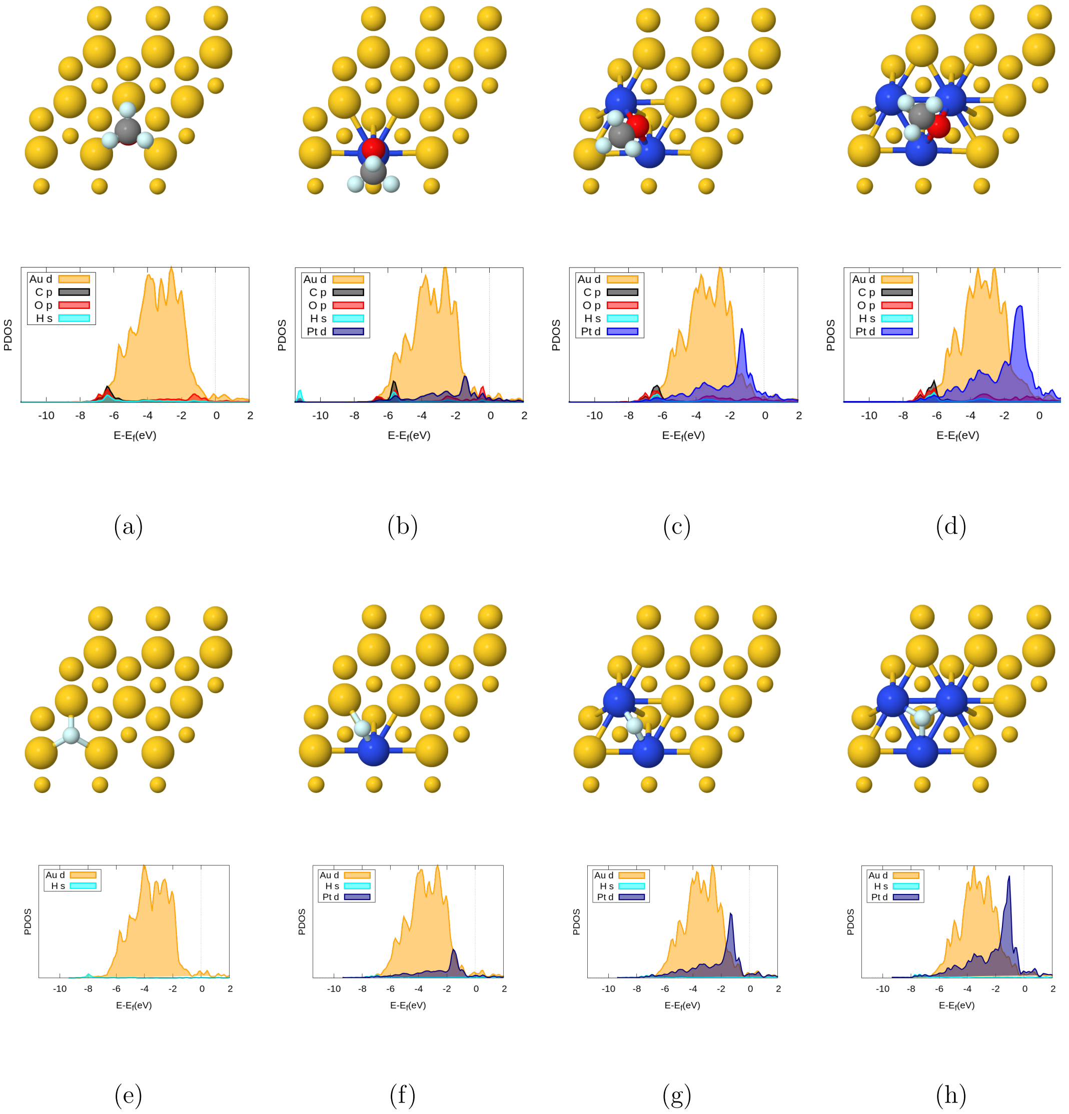

(a) (b) (c) (d)

(e) (f) (g) (h)

Figure 4.3: The first row represents the ontop views of most stable sites of the adsorption of CH_3O molecule on bare, Au/Pt, Au/2Pt and Au/3Pt surface, respectively. The second row shows the corresponding PDOS profiles for them . The third row represents the those for the H atom adsorption with most stable configurations. The last row displays the PDOS profiles for the adsorption of H . In the figures, Au atoms are in yellow, H atoms are in turquoise, C are in grey and O atoms are in red.

Table 4.3: Adsorption energies (in eV) of O atom and OH molecule on bare Au(111) and surface and Au(111) surface with different magnitude of dopant atoms of Pt.

	O				OH			
	Au	Au/Pt	Au/2Pt	Au/3Pt	Au	Au/Pt	Au/2Pt	Au/3Pt
hcp-hollow	-4.85	-5.00	-5.17	-5.36	-2.53	-2.73	-2.79	-2.77
fcc-hollow	-5.07	-5.24	-5.43	-5.40	-2.66	-2.61	-2.80	-2.83
bridge	-5.07	-5.23	-5.43	-5.40	-2.60	-2.66	-2.80	-2.82
ontop	-4.84	-4.84	-4.74	-5.31	-2.41	-2.35	-2.27	-2.76

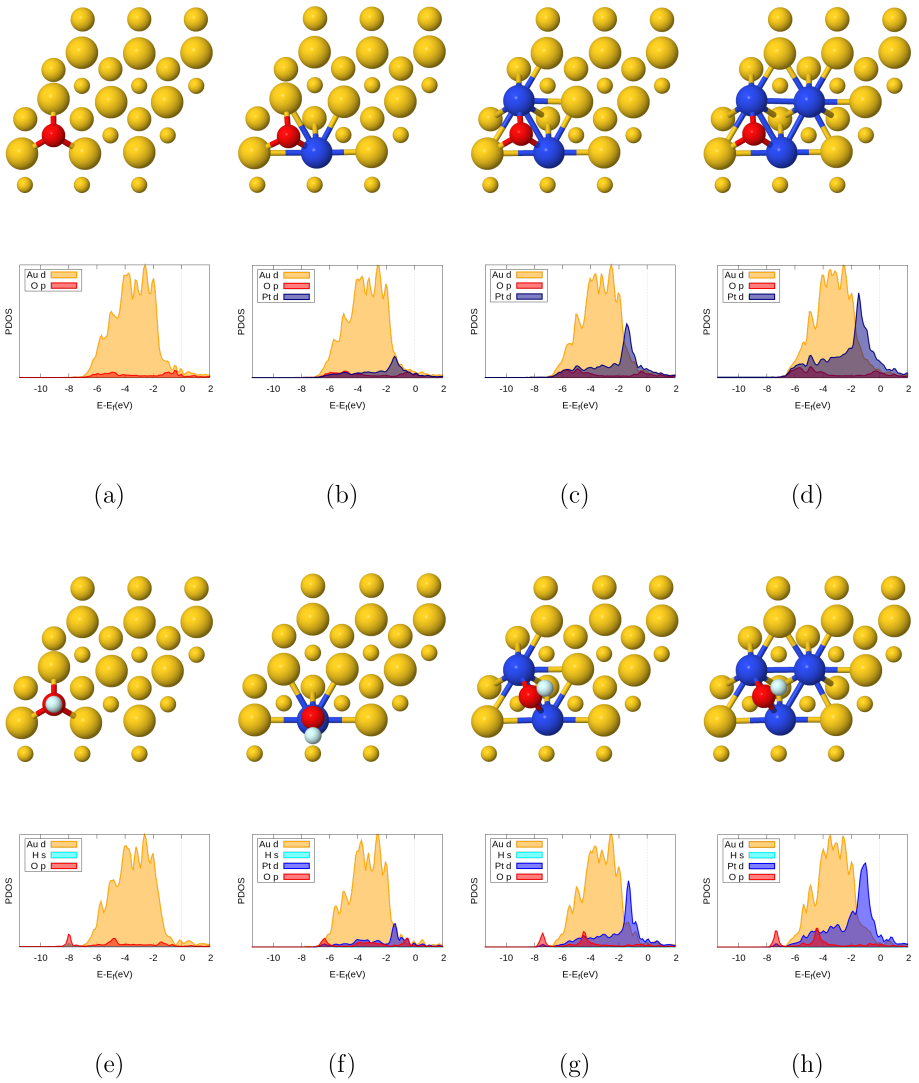

(a) (b) (c) (d)

(e) (f) (g) (h)

Figure 4.4: The first row represents the ontop views of most stable sites of the adsorption of O atom on bare, Au/Pt, Au/2Pt and Au/3Pt surface. The second row shows the corresponding PDOS profiles for O . The third row represents the those for the OH atom adsorption with most stable configurations. The last row displays the PDOS profiles for the adsorption of OH. In the figures, Au atoms are in yellow,H atoms are in turquoise,C are in grey and O atoms are in red.

4.3.2.2 Molecular adsorption on the full Pt top layer and sublayers

The results in the previous section suggest that the binding energies are somewhat improved with increasing dopant concentration. To explore the limits of doping, and search for stable sites for the same adsorbates was repeated. Throughout this chapter, we shall refer to this surface as named the Au/9Pt slab.

The CH_3OH molecule as seen from the Table 4.4 is weakly bound to Au/9Pt slab. There is a slight increase in the binding energies when compared to those on bare surface, except for the ontop site. However the results are very similar to those obtained for the Au/2Pt and Au/3Pt surfaces as seen in Table 4.1. According to the values illustrated in Table 4.4, the hcp hollow, fcc hollow and bridge sites yield approximately the same adsorption energies, whereas the ontop site is the most energetically stable site with a binding energy of -0.38 eV. During the geometry optimization the bond lengths in the CH_3OH molecule slightly increae by about 0.02 A°. Additionally, this molecule on the top site changes its initial position radically by rotating around the molecular axis.

Table 4.4: Adsorption energies (in eV) of the CH_3OH (the left one) and CH_3O (the right one) molecules on Au/9Pt type of slab.

	CH_3OH Au/9Pt	CH_3O Au/9Pt
hcp-hollow	-0.13	-2.09
fcc-hollow	-0.13	-2.24
bridge	-0.15	-2.09
ontop	-0.38	-1.95

The energetics of CH_3O on the Au/9Pt surface is also studied. The adsorption energies and the optimized structure of the molecule given in the Table 4.4 and Figure 4.5. Fcc hollow site is the most stable site with a binding energy of -2.24 eV, and the ontop site is identified as the least favorable site according to our results. Overall, the Pt top layer enhances the binding energies when compared to Table 4.2. There is a slight elongation observed in bond lengths for the molecule.

A similar analysis is performed for the OH molecule and H and O atoms. Table 4.5 reports the calculated binding energies of the OH molecule. The fcc hollow site is identified as the most stable site. Adsorption energies do not significantly with respect to the single, double and triple dopants. The results are very close to each other obtained from previous calculations at Table 4.3 and one can conclude that the number of dopant atoms have almost no effect on the binding energies of OH molecule.

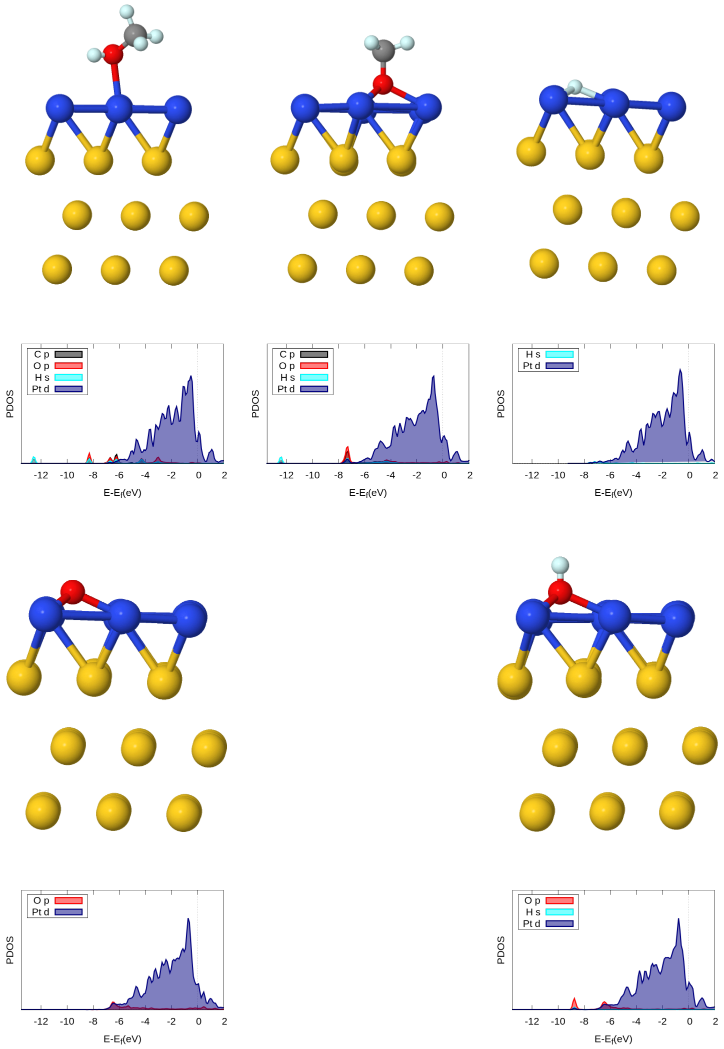

Figure 4.5: The first row represents the side views of most stable sites of the adsorption of CH_3OH, CH_3O, and H with corresponding PDOS profiles given in second row. The third row shows the same for the O atom and OH molecule along with corresponding PDOS profiles given in fourth row. In the figures, Au atoms are in yellow,H atoms are in turquoise,C are in grey, Pt atoms are in navy and O atoms are in red.

The fcc hollow and bridge sites have same adsorption energy value for O binding at Au/9Pt surface and these sites most favorable sites for this atom. Again binding energies are not improved when increase the number of dopant concentration as seen from the results in Table 4.5, and 4.3 . The adsorption energies are smaller for the H atom on Au/9Pt slab. Fcc hollow and bridge sites share the same adsorption values which are also favorable sites for H binding. Additionally, H atom which is initially located at bridge site migrates to the fcc hollow site.

Table 4.5: Adsorption energies (in eV) of the OH moecule (the left panel), O (the middle panel) and H (the right panel) atoms on Au/9Pt type of slab.

	OH	O	H
	Au/9Pt	Au/9Pt	Au/9Pt
hcp-hollow	-2.40	-4.45	-2.99
fcc-hollow	-2.65	-4.67	-3.04
bridge	-2.44	-4.67	-3.04
ontop	-2.27	-4.45	-2.65

Next, we turn our attention to subsurface slab. This type of slab will be referred to as Au/sub in the rest of this chapter. The binding energy values of the species studied thus far are tabulated in Tables 4.6 and 4.7, additionally geometry optimized configurations with their PDOS profiles of the most stable sites are given in the Figure 4.6.

Table 4.6: Adsorption energies (in eV) of the CH_3OH (the left one) and CH_3O (the right one) molecules on Au/sub type of slab.

	CH_3OH	CH_3O
	Au/sub	Au/sub
hcp-hollow	-0.11	-1.64
fcc-hollow	-0.10	-1.77
bridge	-0.11	-1.66
ontop	0.12	-1.54

Table 4.7: Adsorption energies (in eV) of the OH molecule (the left panel), O (the middle panel) and H (the right panel) atoms on Au/sub type of slab.

	OH	O	H
	Au/sub	Au/sub	Au/sub
hcp-hollow	-1.96	-3.12	-2.26
fcc-hollow	-2.19	-3.46	-2.26
bridge	-2.15	-3.46	-2.26
ontop	-1.98	-3.125	-2.14

As seen from the table, all adsorption energies corresponding to the CH_3OH molecule are energetically almost equivalent, therefore; no site is favorable with respect to any

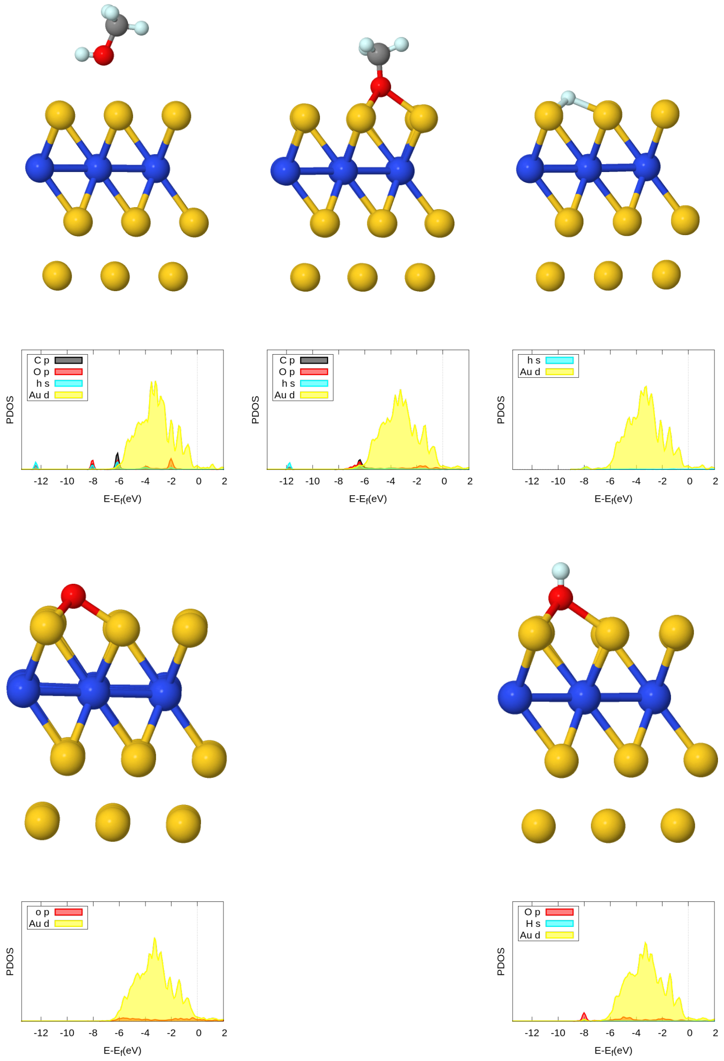

Figure 4.6: The first row represents the side views of most stable sites of the adsorption of CH_3OH, CH_3O, and H with corresponding PDOS profiles given in second row. The third row shows the same for the O atom and OH molecule along with corresponding PDOS profiles given in fourth row. In the figures, Au atoms are in yellow,H atoms are in turquoise,C are in grey, Pt atoms are in navy and O atoms are in red.

other. When these values are compared to results given in Table 4.1,it is evident that the sublayer substitution does not improve the binding energies. In addition, Au/Pt and Au/sub results also very similar. For this molecule, there a slight increase is observed in bond when it is adsorbed on Au/sub. The fcc hollow site is the most stable adsorption site for CH_3O molecule. The presence of the once again fails to enchance the adsorption energies when compared to the Table 4.6 and Table 4.2. Additionally the results corresponding to sublayer doping is even less than those for the bare surface. Similar results are observed for the adsorption of OH molecule and O and H atoms. The binding energies are given in Table 4.7.

4.3.3 Coadsorption Energies

In the previous sections, the adsorption energies of the molecules on bare and doped surfaces were examined individually. While the CH_3OH molecule is adsorbed by itself on gold surface, before the reaction, the products CH_3O and H will be found simultaneously on the surfaces. Therefore the coadsorption energy calculations will be performed in order to study how these molecules and atoms influence each other on the slab. Due to the fact that Au/sub type of slab does not dramatically change the binding energies of the molecules and atoms involving in reaction process, we perform any coadsorption energy calculations on this termination.

With this aim, first the coadsorption of CH_3O and H will be examined on bare Au(111), Au(111)/Pt, Au(111)/2pt, Au(111)/3Pt and Au(111)/9Pt . In our NEB calculations, we also calculate activation barriers on the oxygen precovered surface; hence, the coadsorption of CH_3OH with O and CH_3O with OH will also be explored.

4.3.3.1 Coadsorption of the CH_3O, and H

After dissociation of CH_3OH through O-H bond breaking, the CH_3O and H are found on the surfaces at the same time. Therefore it is worth calculating the binding energies of both adsorbents. In order to achieve this, the CH_3O molecule is placed at its most stable site which was previously obtained, then the H atom is placed at different adsorption sites in the neighborhood of the CH_3O molecule. The coadsorption energies are evaluated by using the formula,

$$E_{ads} = E_{tot}^{(Au-slab+\mathrm{CH_3O}+\mathrm{H})} - \left(E^{(Au-slab+\mathrm{H})} + E^{\mathrm{CH_3O}}\right) \tag{4.2}$$

where $E_{tot}^{(Au-slab+\mathrm{CH_3O}+\mathrm{H})}$ is the total energy of the Au-slab with CH_3O and H, $E^{(Au-slab+\mathrm{H})}$ gives the total energy of the H on Au-slab which is previously obtained, and the last term defines the total energy of the CH_3O molecule itself. The results are given in the Table 4.8. In that Table the notation of site/H represents the place of the H atom on the corresponding slab.

Table 4.8: Coadsorption energies (in eV) of molecular adsorption of the CH_3O with H on bare Au(111) and doped surfaces.

	Au	Au/Pt	Au/2Pt	Au/3Pt	Au/9Pt
hcp-hollow/H	-1.76	-1.64	-1.28	-1.55	-2.11
fcc-hollow/H	-1.73	-2.91	-1.66	-1.54	-2.06
bridge/H	-1.67	-2.89	-2.48	-2.56	-2.06
ontop/H	-1.87	-1.88	-1.83	-1.73	-2.18

The geometry optimized structure of coadsorption of CH_3O with H is given in Figures 4.7,4.8. When CH_3O molecule is on bare surface without H atom, the most favorable site is fcc hollow with an adsorption energy of -1.75 eV according to Table 4.2. The same molecule on this site with the H, the adsorption energy values decrease for the case of H atom at fcc hollow and bridge sites. However, the H atom at the ontop site improves the binding energy of CH_3O by about -1.87 eV. The H atom does not affect the bond lengths in CH_3O molecule. During the geometry optimizations the H atom initially placed at hcp hollow, fcc hollow and ontop sites migrates to the fcc hollow, ontop and hcp hollow sites, respectively.

On the Au/Pt surface, without H, the hcp hollow is the most energetically favorable site for CH_3O molecule corresponding to an adsorption energy of -1.88 eV. The H atom increases the binding energy values by about 1 eV for the fcc hollow/H , bridge/H. There is a slight increase observed for ontop/H configurations. When the H atom is placed on the bridge and fcc hollow sites, it recombined with adsorbed CH_3O to form CH_3OH. This configurations are shown in Figure 4.7.

Similar trends are obtained for these adsorbates on Au/2Pt and Au/3Pt. The adsorption energies of CH_3O molecule decreases in the presence of the H atom except for bridge sites on both surface terminations. Geometry optimized structure of those configurations, H joins to CH_3O molecule that may results in the larger binding energies.

The most favorable site is for CH_3O when it is by itself on the Au/9Pt surface is fcc hollow. However, on the same termination with the H atom, the most energetically stable site is shifted to ontop site with a lower binding energy value of -2.18 eV

. The results listed in Table 4.4, the binding energies do not recovered much with H atom except for H atom at ontop site when compared to Tables 4.8. Only those figures for the most stable sites of the CH_3O molecule with H atom on the surfaces are presented in Figure 4.8. No significant change is observed in the bond lengths in CH_3O molecule on the Au/9Pt slab.

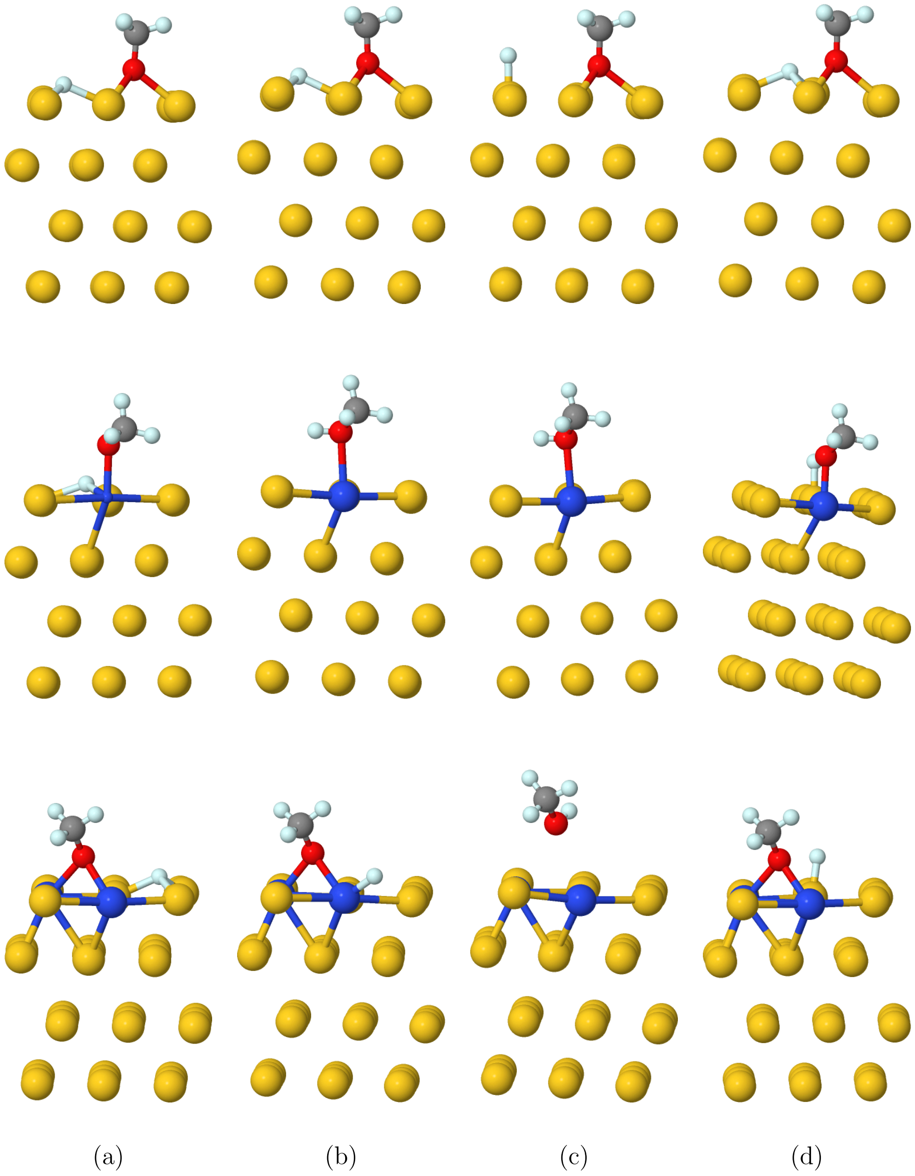

Figure 4.7: The top, middle and bottom panels show the geometry optimized structures of CH_3O adsorption on the bare, Au/Pt, Au/2Pt slabs with H atom and first, second, third and fourth columns represent the H at hcp, fcc, bridge and ontop positions on the mentioned slabs, respectively. In the figures, Au atoms are in yellow,H atoms are in turquoise,C are in grey, O atoms are in red and Pt atoms are in navy.

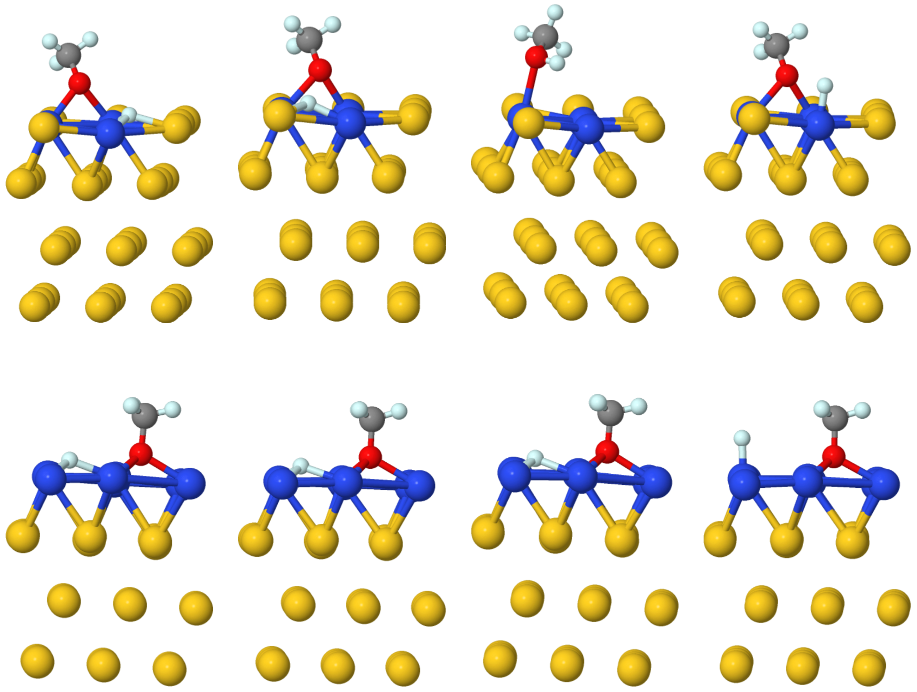

(a) (b) (c) (d)

Figure 4.8: The top and bottom panels show the geometry optimized structures of CH_3O adsorption on the Au/3Pt, Au/9Pt slabs with H atom and first, second, third and fourth columns represent the H at hcp, fcc, bridge and ontop positions on the mentioned slabs, respectively. In the figures, Au atoms are in yellow,H atoms are in turquoise,C are in grey, O atoms are in red and Pt atoms are in navy.

4.3.3.2 Coadsorption Energies of the CH_3O, and OH

As indicated in the introduction part, preadsorbed O atom decreases the activation barrier of the methanol oxidation reaction drastically. After breaking the O-H bond, the H atom selectively makes bond with O on the surface, giving rise to the final products the CH_3O and OH. Therefore, it is important to examine the coadsorption energies of these molecules. We employ the following process: CH_3O molecule is placed first at its stable sites on each surfaces and OH molecule is sequentially adsorbed on four distinct binding sites around the CH_3O molecule. The adsorption energies are calculated by using the formula

$$E_{ads} = E_{tot}^{(Au-slab+\mathrm{CH_3O+OH})} - (E^{(Au-slab+\mathrm{OH})} - E^{\mathrm{CH_3O}}). \qquad (4.3)$$

Table 4.9: Coadsorption energies (in eV) of CH_3O molecule with OH molecule on bare Au(111) and doped surfaces Au(111) surfaces.

	Au	Au/Pt	Au/2Pt	Au/3Pt	Au/9Pt
hcp-hollow/OH	-1.79	-1.95	-1.45	-2.25	-2.30
fcc-hollow/OH	-1.65	-2.07	-1.65	-2.20	-1.83
bridge/OH	-1.77	-1.72	-1.65	-1.97	-2.10
ontop/OH	-1.82	-2.08	-1.99	-1.81	-2.32

On bare surface without the OH molecule, the fcc hollow site is the most stable site for CH_3O molecule with binding energy value of -1.75 eV. The adsorption energies corresponding hcp hollow, bridge sites are healed with OH molecule when compared the Tables 4.9 and 4.2. During the structure optimization, the OH molecule initially at hcp site migrates to ontop site and becomes almost parallel to the surface. Similar trends are observed for the sites of fcc, bridge and ontop sites. The bond length of OH molecule slightly shortens for all sites, whereas the bond lengths in CH_3O molecule are remained unchanged.

According to results given in the Table 4.9, on the Au/Pt surface, all adsorption energies increase with OH molecule, the ontop site corresponds to the stable site with a larger binding energy value of -2.08 eV when compared to the Table 4.9. During geometry optimization process, OH bond length increases except for OH molecule at the bridge site. Again there is no change is observed for bond lengths in CH_3O molecule. For all configurations, the OH molecule becomes tilted on the surfaces as given in Figure 4.9.

The OH molecule improves only the binding energy of the ontop site on the Au/2Pt surface. The other adsorption energy values are lower than the results reported inTable 4.2. With the OH molecule, the strongest adsorption site for CH_3O molecule is ontop site. When CH_3O molecule without OH on Au/2Pt surface, the hcp hollow correspond to largest binding energy value; however, with OH molecule this site yields the lowest adsorption energy value. The geometry optimized structures reveal that the OH molecule initially perpendicularly placed at fcc hollow, bridge and ontop sites becomes tilted.

Au/3Pt surface with OH yields larger adsorption energy values and adsorption at the hcp hollow site is stronger on this surface with value of -2.25 eV. According to geometry optimized structures, the OH molecule is elongated and is once tilted with respect to the surface.

We also consider the same calculations for the surface on Au/9Pt. On this surface, without the OH molecule, the fcc hollow sites is the most favorable site, whereas same surface with OH gives the lowest adsorption value. The strongest adsorption geometry corresponds to the configuration of OH molecule at the ontop site corresponding value of -2.32 eV.

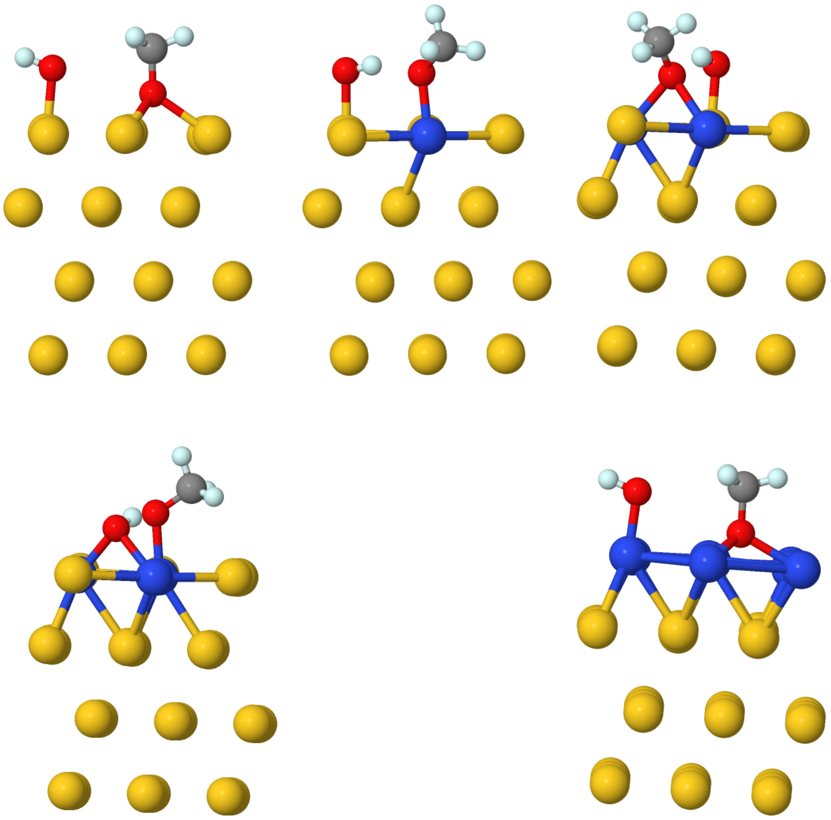

Figure 4.9: The first panel shows the geometry optimized structures of CH_3O adsorption on the bare, Au/Pt, Au/2Pt slabs with OH atom and second one represents the same for Au/3Pt and Au/9Pt , respectively. In the figures, Au atoms are in yellow,H atoms are in turquoise,C are in grey, O atoms are in red and Pt atoms are in navy.

4.3.3.3 Coadsorption of the CH_3OH, and O

Before the dissociation of CH_3OH to CH_3O and H, on the O-precovered surfaces, the CH_3OH and O atom exist on the surface together. Therefore, the coadsorption energies of CH_3OH and O are also studied. We follow the same process described for the other coadsorption studies .

Table 4.10: Coadsorption energies (in eV) of CH_3OH molecule with O on bare Au(111) and doped surfaces.

	Au	Au/Pt	Au/2Pt	Au/3Pt	Au/9Pt
hcp-hollow/O	-0.13	-0.04	+0.30	+0.11	-0.12
fcc-hollow/O	-0.38	-0.39	-0.38	-0.47	-0.37
bridge/O	-0.40	-0.38	+0.57	-0.47	-0.14
ontop/O	-0.36	-0.69	-0.37	-0.35	-0.11

All results are presented in Table 4.10 . According to these data, on bare surface with O atom, the adsorption energies range from -0.13 to -0.40. The most favorable adsorption site corresponds to the configuration where the O atom is at the bridge site. A comparison of this table to Table 4.1 reveals that all binding energies are improved in the presence of atomic O. During structure optimization, CH_3OH molecule on all sites has a tendency to rotate while approaching to surface.

Adsorption at the ontop is stronger on the on Au/Pt surface with O atom for CH_3OH . The other adsorption energies also increase except for hcp site which corresponds to the lowest adsorption energy value of -0.04 eV. The CH_3OH molecule dissociates spontaneously to CH_3O and H for the ontop configuration during the geometry optimization.

The adsorption energies for the O atom at hcp hollow and bridge sites on Au/2Pt surface take positive values indicating unstable adsorption according to Table 4.10. The adsorption energy values corresponding to fcc hollow and ontop site are almost equivalent, therefore these two sites can be defined as energetically favorable configurations for the CH_3OH molecule.

O atom at the hcp hollow site on the Au/3Pt surface yields positive adsorption energy value of +0.11 eV. according to Table 4.10. With the O atom, the all binding energies for CH_3OH increase. On the Au/9Pt surface, the adsorption energies do not change except for fcc hollow site which is the most energetically favorable site for CH_3OH molecule in the presence of the O atom.

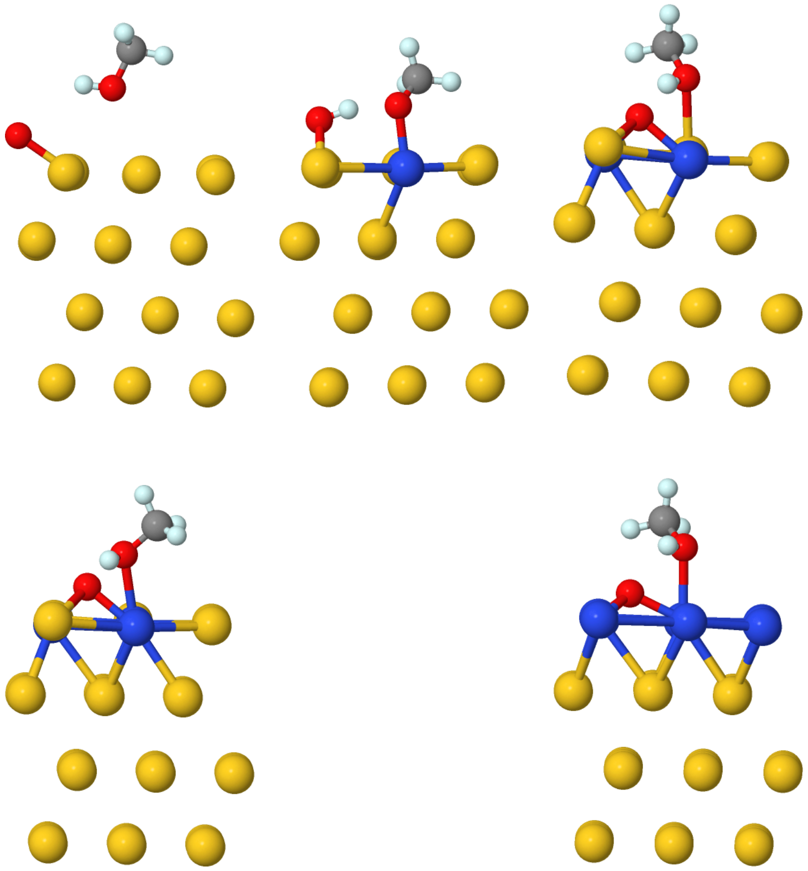

Figure 4.10: The first panel shows the geometry optimized structures of CH_3OH adsorption on the bare, Au/Pt, Au/2Pt slabs with O atom and second one represents the same for Au/3Pt and Au/9Pt , respectively. In the figures, Au atoms are in yellow,H atoms are in turquoise,C are in grey, O atoms are in red and Pt atoms are in navy.

4.4 Activation Energies

4.4.1 Activation Energies of the CH_3OH oxidation

In order to see the influence of the of the Pt atom on the activation energies, the reaction is studied using CI-NEB first over clean Au(111) surface. The dissociation reaction of methanol to CH_3O and H through O-H bond cleavage is examined by considering the most favorable geometries on Au(111) surface based on the calculations of the previous section. For this calculation, the same surface model is used as in the case of the surface on which the binding energies are calculated. During the calculation the two bottom layers are fixed, then the two top layers are are allowed to fully relax. The reaction path is divided into 7 images. For the initial geometry, the CH_3OH molecule is first placed onto hcp site on bare surface, whereas CH_3O and H are placed on the adjacent fcc sites on clean Au surface for final geometry. Both configurations are subjected to optimization process. The other stages of the reaction path are defined by program by NEB method.

The activation barrier for clean surface is calculated to be 1.76 eV and the transition state corresponds to 5 th image. As seen from the Figure 4.11 at transition state, the dissociation happens by breaking the O-H bond and CH_3O molecule and H start to move towards their final locations.

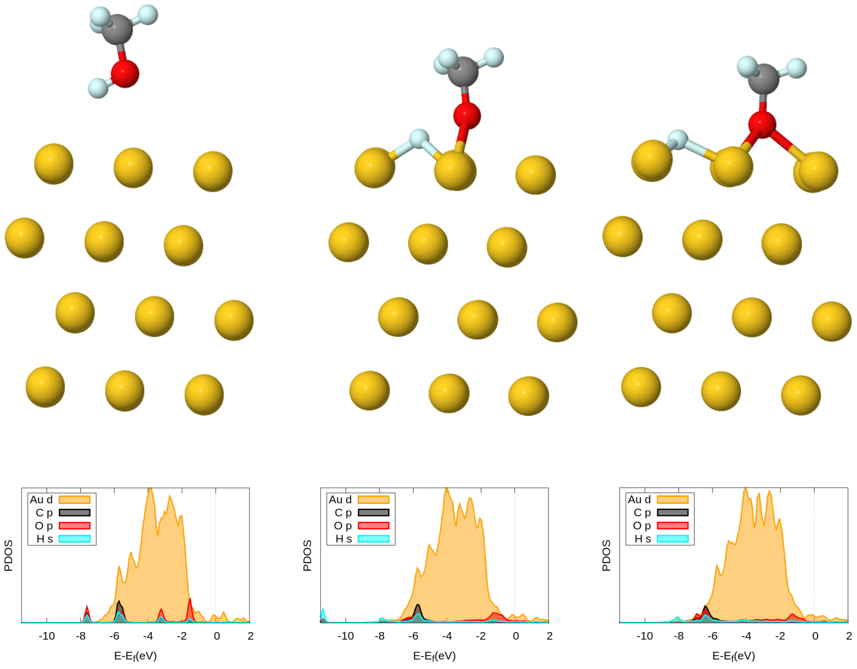

(a)

(b)

(c)

Figure 4.11: The dissociation of CH_3OH molecule to CH_3O and H on the clean Au(111) surface along with PDOS profiles of initial, transition and final configurations. In the figures, Au atoms are in yellow,H atoms are in turquoise,C are in grey and O atoms are in red.

The activation barriers for doped surfaces with different concentrations of Pt on the surface is also investigated. In order to compare activation energies obtained from doped surfaces and the value of found from the bare surface case , the same symmetrical sites are used for initial and final configurations of adsorbates. The reaction path is again divided into 7 images, but for some calculations we use 9 images for higher accuracy. The presence of one Pt atom as dopant on the surface which is referred to as Au/Pt reduces the activation energy to 1.18 eV which is a decrease of 0.6 eV in comparison to reaction on the clean surface. The corresponding initial, transition and final stages with their PDOS profiles are given for the reaction on Au/Pt (111) surface.

The surface with two and three dopant atoms are first investigated and the corresponding surfaces are named as before Au/2Pt and Au/3Pt, respectively . The reaction barriers 1.26 eV for Au/2Pt and 1.28 eV for Au/3Pt. Finally the activation barrier for full substitutional Pt layer is 0.79 eV. The PDOS profiles and initial, transition and final stages are given Figures 4.12, and 4.13

In previous sections, the adsorption energies were examined on the Au/sub type of slab and the energies were found to be considerably lower than the others surfaces we consider. But even so, dehydrogenation of CH_3OH molecule is also investigated on it. The activation barrier is calculated as 1.70 eV which is very close to the value obtained on the clean surface. It can be inferred from these results that the configuration of Au/sub does not improve the binding energies of molecules and atoms involving the dissociation process; additionally, it does not decrease the activation barriers. The initial, transition, final states with PDOS plots of the reaction on Au/sub surface is given in the Figure 4.14.

Table 4.11: The all activation barrier results on the surfaces in eV.

	Activation barrier (in eV)
Au/bare	1.76
Au/Pt	1.18
Au/2Pt	1.26
Au/3Pt	1.28
Au/9Pt	0.79
Au/sub	1.70

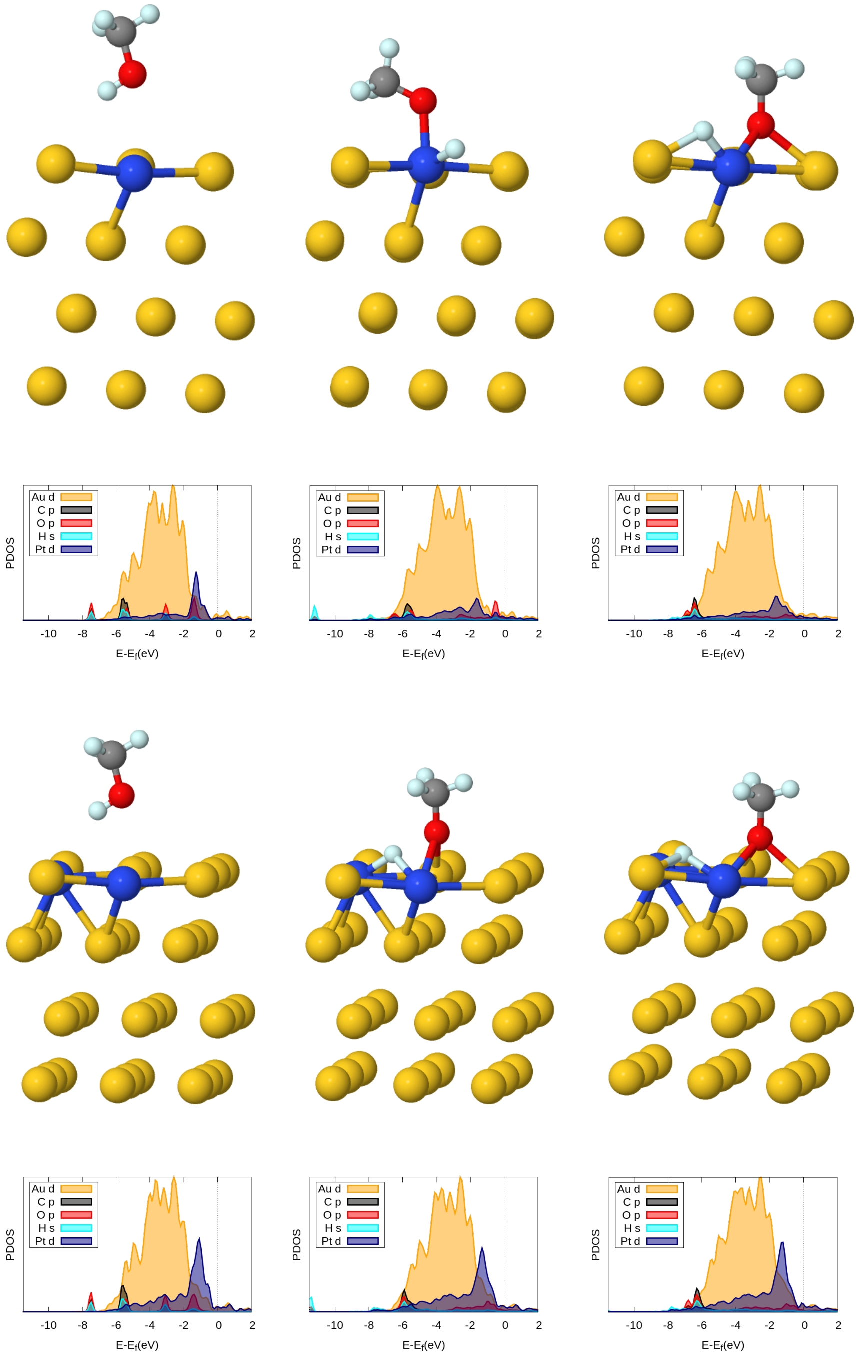

Figure 4.12: The first and second rows represent the dissociation of CH_3OH molecule to CH_3O and H on the Au/Pt (111) surface along with PDOS profiles of initial, transition and final configurations. The third and fourth rows represent the those for Au/2Pt (111) surface. In the figures, Au atoms are in yellow, Pt atoms are in blue, H atoms are in turquoise, H atoms are in turquoise, C are in grey and O atoms are in red.

The all activation barrier results are summarized in Table 4.11. Our results indicate that activation energy decreases even for the case where only one Pt atom is placed

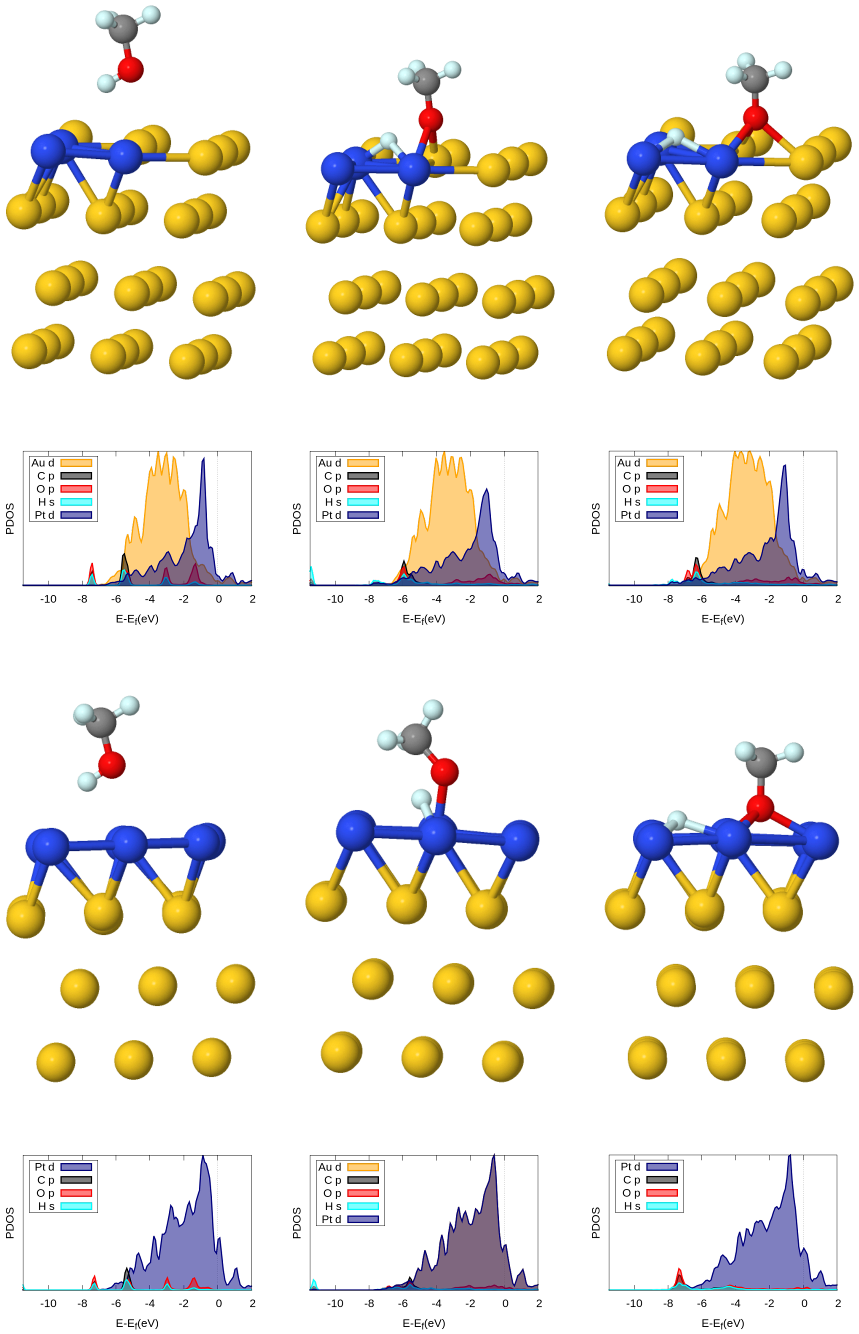

Figure 4.13: The first and second rows show the dissociation of CH_3OH molecule to CH_3O and H on the Au/3Pt (111) surface along with PDOS profiles of initial, transition and final configurations.The third and fourth rows represent the those for last layer doping of Au (111) surface. In the figures, Au atoms are in yellow, Pt atoms are in blue, H atoms are in turquoise, C are in grey and O atoms are in red.

on the surface. One can also see that increasing the number of Pt atoms to 2 or 3, corresponding surface structures Au/2Pt and Au/3Pt, gives the almost same value of

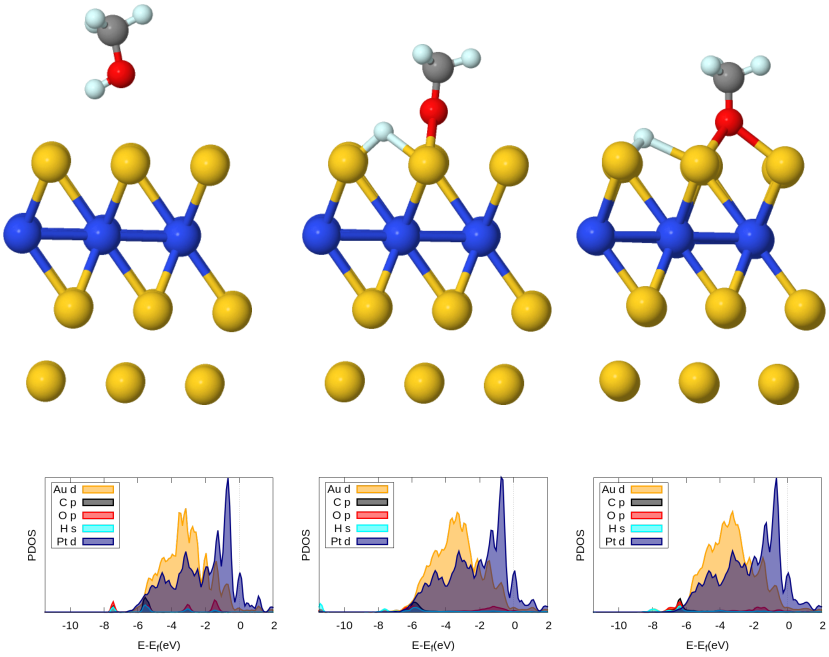

initial stage transition stage final stage

Figure 4.14: The figures represent the initial, transition and final stages of the dissociation of CH_3OH on Au/sub type of slab . In these figures, Au atoms are in yellow, H atoms are in turquoise, C are in grey, Pt are in navy and O atoms are in red.

for activation energy. Remarkably, when the whole surface is coated with Pt atoms (Au/9Pt), the activation barrier takes a value lower than the case of one Pt atom on the surface.

4.4.2 Activation Energies of the Dissociation of CH_3OH on O precovered surfaces

In the introduction part, it was stated that the precovered O atom on the surface activates the H atom in alcohol group and enhances the dissociation process according to many studies. In this section, we verify these findings for our Pt-enhanced surfaces. O and CH_3OH are reactants at the initial stage as seen from the Figure 4.15; then during the process, the H atom ,coming from the CH_3OH, makes a bond with O atom to form OH molecule. The activation barrier is 0.22 eV which is much less than the value obtained for the clean surface.

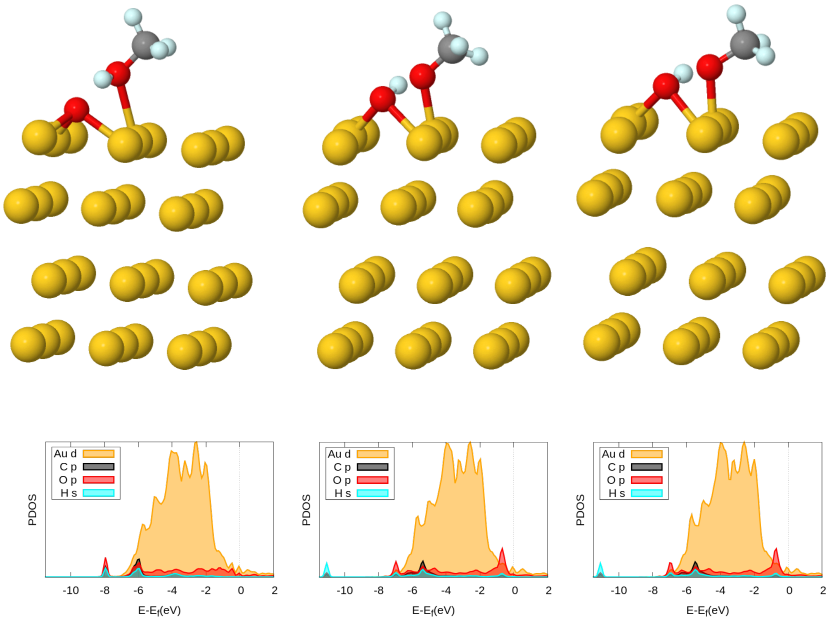

initial stage transition stage final stage

Figure 4.15: The figures represent the initial, transition and final stages of the dissociation of CH_3OH on Au(111) surface with the precovered O atom. In these figures, Au atoms are in yellow, H atoms are in turquoise, C are in grey and O atoms are in red.

Table 4.12: The all activation barrier results (in eV) on surfaces both with O add atoms and dopant atoms.

	Activation barrier (in eV.)
Au/bare	1.76
Au/bare with O	0.22
Au/Pt with O	0.25
Au/2Pt with O	0.68
Au/3Pt with O	0.09

In the previous sections, the activation barriers for the relevant reaction are decreased with the increasing number of dopant atoms, and the activation barrier significantly reduces on the surface with O add atom. We additionally examine how the reaction barriers changes both with dopant atoms and O add atom on the Au(111) surface. The presence of both on the surface decrease the activation barrier when compared the activation barrier on the clean surface according to results listed in Table 4.12.

Only for the surface of Au/3Pt with O atom, the activation barrier is remarkably decreased to 0.09 eV which is even less than the Au(111) surface with precovered O atom. Interestingly, the dissociation on O covered Au/2Pt surface yields larger energy barrier. There is a tendency for the OH molecule to rotate on this type of slab as seen from the Figure 4.16, which is attributed to the higher value in activation energy.

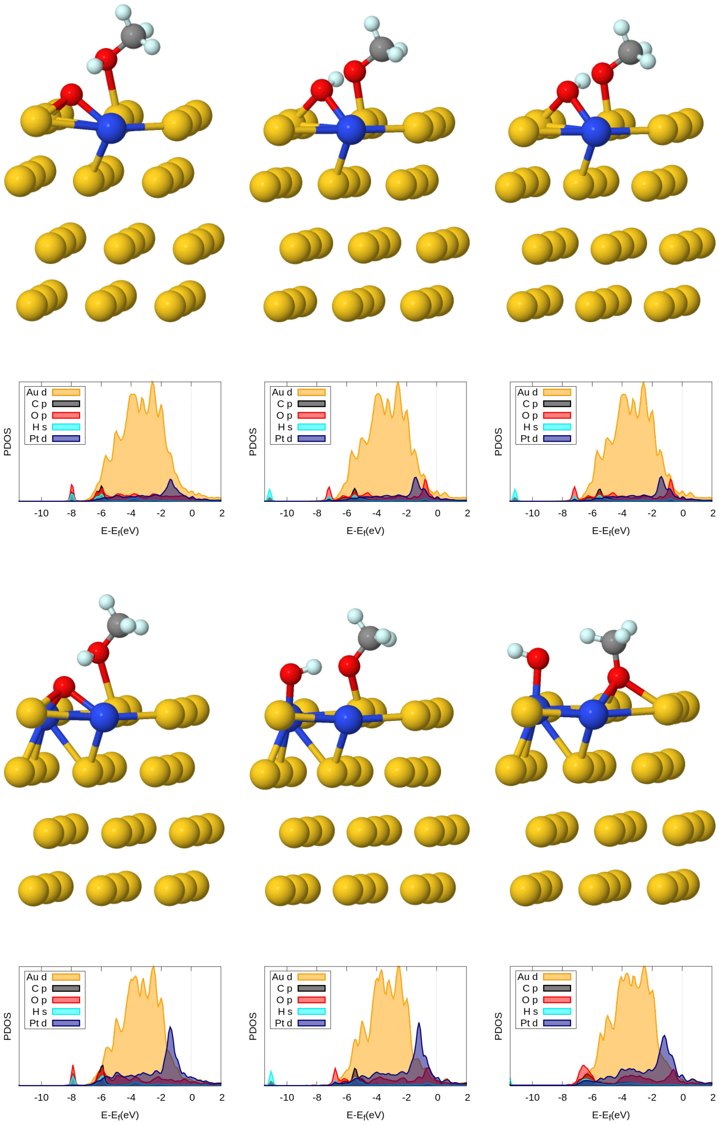

Figure 4.16: The figures represent the initial, transition and final stages of the dissociation of CH_3OH on Au/Pt and Au/2Pt surfaces with the precovered O atom. In these figures, Au atoms are in yellow, H atoms are in turquoise, C are in grey and O atoms are in red.

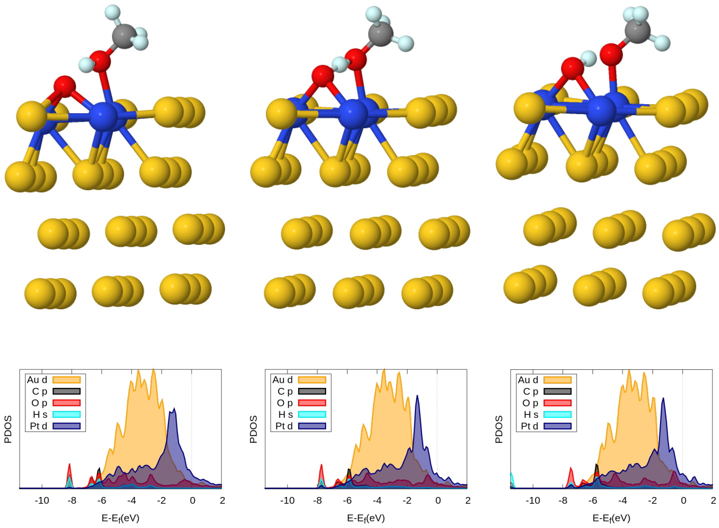

Figure 4.17: The figures represent the initial, transition and final stages of the dissociation of CH_3OH on Au/3Pt surface with the precovered O atom. In these figures, Au atoms are in yellow, H atoms are in turquoise, C are in grey and O atoms are in red.

4.5 Conclusion

In this chapter, we studied the decomposition of CH_3OH molecule to CH_3O and H on the clean, Pt doped, precovered O and both doped and precovered Au (111) surfaces via DFT calculations. The dissociation of CH_3OH molecule takes place through the O-H bond breaking; therefore, we examine the adsorption energies of CH_3OH, CH_3O, and H on the Au(111) surfaces for determining the most stable sites for all species involved. We also examined the effect of the precovered O atom on Au surface on the activation barriers, hence OH molecule was selectively formed. Besides, the adsorption energies of O and OH molecule were also calculated. Our adsorption energy calculations reveal that the CH_3OH molecule was weakly bound to the clean Au surface. A slight increase was observed for binding energies of CH_3OH molecule on the doped surfaces. On the contrary, CH_3O molecule strongly interacts with surface. Pt atoms as dopant have no significant effect on the adsorption energies of CH_3O molecule.The adsorption energies of H atom on the clean and doped surfaces were relatively high when compared to CH_3OH and CH_3O molecules. A substantial increase was obtained for adsorption energies of the O atom on the surface of Au/Pt, Au/2Pt, and Au/3Pt. Interestingly, the energies were not improved further on the

Au/9Pt surface. The adsorption energies of OH molecule was finally examined, and no significant changes in the adsorption energies were observed for the doped surfaces. The general outcome for the molecules and atoms on Au/sub slab is that the adsorption energies do not change dramatically with respect to the clean surfaces.

After examining individually the binding energies of molecules and atoms, coadsorption energies were also considered on clean, Au/Pt, Au/2Pt, Au/3Pt and Au/9Pt surfaces. The coadsorption energies of CH_3OH with O, CH_3O with H, and CH_3O with OH were calculated in order to study how these molecules and atoms influence each other on the slabs.

Finally the activation barriers of the dissociation process were computed. We observed that the reaction barrier was notably decreased when Pt dopant atoms were introduced on the surfaces. The smallest activation barrier was found on the Au/9Pt slab corresponding to value a of 0.79 eV. The decomposition of CH_3OH molecule was studied also on the O precovered surfaces and the activation barrier was found as 0.22 eV. When doped and O precovered surfaces are compared in terms of their activation energies, Au/9Pt surfaces are found to have a larger value but having much lower than the value obtained in the clean surface.

CHAPTER 5

ULTRAFAST 3D LASER MICROMACHINING FOR SOLAR CELLS

5.1 INTRODUCTION

Solar cells based on crystalline silicon is the most dominant technology in photovoltaic industry; however, there are still some difficulties. The main one is that the thickness of silicon wafers are in the range of 180-250 μm while the active region of these wafers is only in the domain of 2-10 μm depending on the amount of doping. On the other hand, materials such as amorphous silicon (a-Si), cadmium telluride (CdTe) and copper indium gallium di-selenium (CIGS) with high absorption are used in thin film solar cells technology. However, the efficiency of thin film solar cells produced from these materials is lower than that of thick crystalline Si solar cells [88, 89, 90]. Additionally, the quantities of the Te and In are limited on earth affecting negatively the future of CdTe and CIGS solar cells [91, 92]. III-V based semiconductors are another alternative as solar cells, which are very expensive for large-scale applications [93, 94].

The production of thin silicon wafers is not realized by the standard thin film production methods. New techniques must be developed in order to produce thinner wafers. Many research groups in the world have developed new techniques for the production of crystal Si thin films. One important technique is called *smart cut* in which H ions are implanted to the Si crystal surface and then heated to form H bubbles. These bubbles allow the upper layer to be easily separated from the main body [95]. Another method, called *slim cut* relies on the stress created by the metal film coated on Si to remove the thin Si film [96]. There are many other techniques for the production of Si thin films and in this chapter we will present DFT calculations which shed light on the details of a new technique which was developed recently at METU Physics

Department.

In this technique, the goal is to produce thinner silicon wafers of about 1.55 μm using femtosecond lasers. A planar section below the surface of a silicon wafer will be processed completely by applying femtosecond pulses at 1.55 μm. Laser makes the region on which it is focussed amorphous. It is followed by a chemical etchant treatment, resulting in mechanical separation of the wafer along the processed plane since the amorphous part is sensitive to etchant solution. Having extracted this amorphous region, the thinner wafers are obtained. This process is depicted in the Figure 5.1

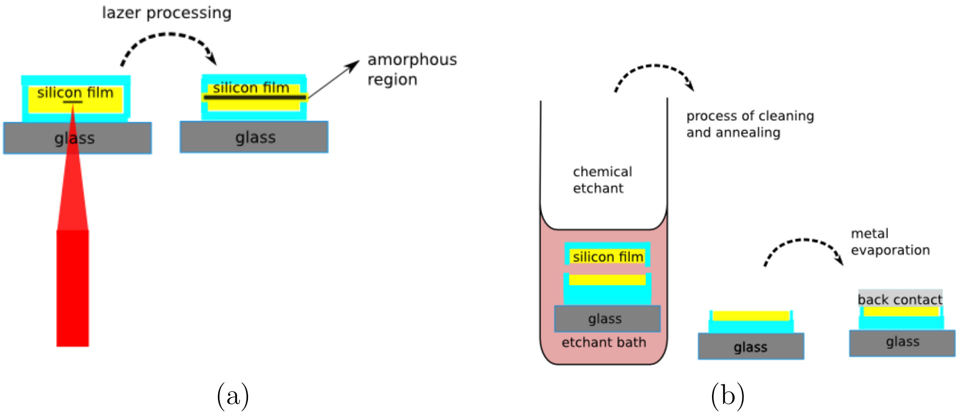
lazer processing
silicon film
glass
silicon film
glass
amorphous region
process of cleaning and annealing
chemical etchant
silicon film
glass
etchant bath
glass
metal evaporation
back contact
glass
(a) (b)

Figure 5.1: Lazer processing of Si films (a) and the chemichal etchant treatment (b).

With the DFT based calculations, the interaction between the amorphous silica, crystal Si, oxidized crystal Si surfaces and ions of different types of etchants is examined by considering their binding energies on these surfaces. Since the etchant solution contains HF and Cu ions, we explore the adsorption energies only these ions and the surfaces.

5.2 Computational and Structural Details

All first principle calculations based on DFT were performed using Quantum Espresso suite [47] within the GGA of Perdew-Wand (PW-91) exchange correlation functional [23]. The vacuum value is chosen to be 14 Å during the all geometry optimization.

SiO_2 can occur in several crystal structures which are quartz, α-tridymite, β-tridymite, α-cristobalite and β-cristobalite [97, 98, 99, 100]. A common property of the crystal silica polymorphs is that around each Si atom there are four O atoms in the shape of a pyramid with triangular base. In different polymorphs, the structures of these pyramids remain the same, but their angle and orientation change with respect to each other [101]. In addition, one of the defining properties of crystal silicate is the closed rings consisting of -Si-O-Si-O- chains given in the Figure 5.2. Amorphous silica is a glassy structure and can easily be obtained by heating crystal silane [102]. Amorphous silica possesses many structural characteristic properties that are reminiscent of crystalline silica. The above-mentioned pyramid shapes and closed rings are among these properties. However, the porous structure of the system introduces a variation in the angle and orientation between the pyramids. It is important to correctly describe the properties of the amorphous silica in theoretical studies, especially in calculations using periodic models. In the studies on amorphous systems, the most commonly used method is to equilibrate randomly placed atoms stoichiometrically in a simulation cell by employing molecular dynamics at high temperatures [103]. In this method, periodic or free boundary conditions [104] can be used. Considering the difficulty of modelling relatively complex amorphous systems in a small simulation cell, it is necessary to perform various statistical analyses for good accuracy of these calculations. As mentioned in the work of Roder et. al., local atomic density, pair distribution function and ring length analysis are among the methods that can be used [104]. In this chapter, the interaction of hydrofluoric acid (HF), which is a part of the etchant used in our experimental studies, with the amorphous silica surface was studied by using DFT.

Amorphous silica coordinates are taken from a previous study obtained by molecular dynamics method [105]. There are 3000 atoms in this simulation cell. In our DFT calculations, a smaller appropriate simulation cell with 12x12x12 (in Å) consisting of Si atoms of 36 and O atoms of 72 is extracted. The mass density of this cell is calculated to be 2.1 g/cm^3, very close to the experimental value which is 2.2 g/cm^3. The created cell is subjected to geometric optimization and all atoms are allowed to relax during this process. The coordinates of the atoms in the cell obtained from minimization procedure can be seen in the Figure 5.2 . In order to validate the model we use, the pair distribution function $g(r)$ is calculated which is consistent with the previous cases reported Bondi et al. [106] given in the Figure 5.2. The result of this analysis is in with the work previously stated work by Bondi and his team.

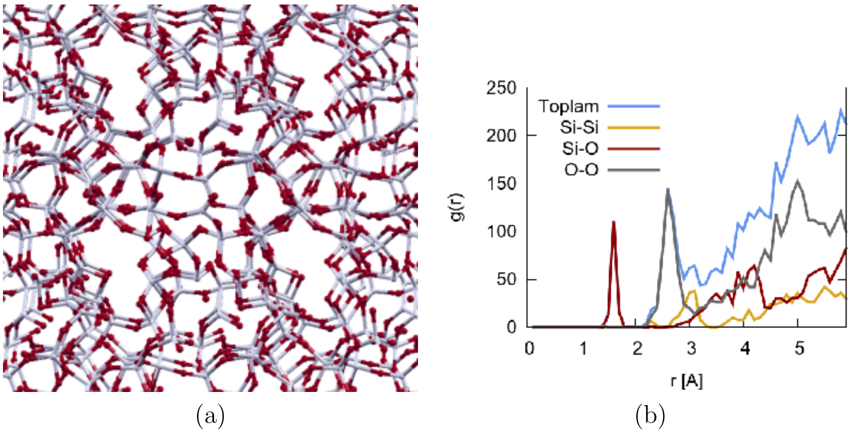

(a) (b)

Figure 5.2: Illustration of the amorphous silica (in a) with their pair distribution (in b). Red spheres refer to O atoms, white ones refer Si.

We also consider the same calculations mentioned in the introduction part on the bare and oxidized surface of Si (100) crystal. Before constructing it, first optimized lattice constant value is found. Si has diamond crystal structure in bulk form and theoretical lattice constant value is calculated as 5.48 Å. The surface of Si (100) with consisting of 48 atoms is constructed by using this value.

5.3 Interaction of Amorphous Surface with Etchants

In order to analyze the interaction between different etchants and the silica surface the binding energies are calculated as

$$E_{ads} = E_{SiO_2+adsorbate} - (E_{SiO_2} + E_{adsorbate}) \tag{5.1}$$

where $E_{SiO_2+adsorbate}$ is the total energy of the SiO_2 surface with adsorbate, E_{SiO_2} is the total energy of the clean surface, and $E_{adsorbate}$ is the energy of the adsorbate. With this definition, stable adsorption geometries have negative adsorption energy values.

First the binding energy of the ions of H and F of the etchant HF is considered on SiO_2 surface. The H ion is placed over one of the O atoms on the surface whereas the F ion is located on the any of Si atoms on the surface. The adsorption energy is found as -1.35 eV, which is quite high, showing that there is a strong interaction between surface and HF acid. The Bader charges are also computed. The charges on the H

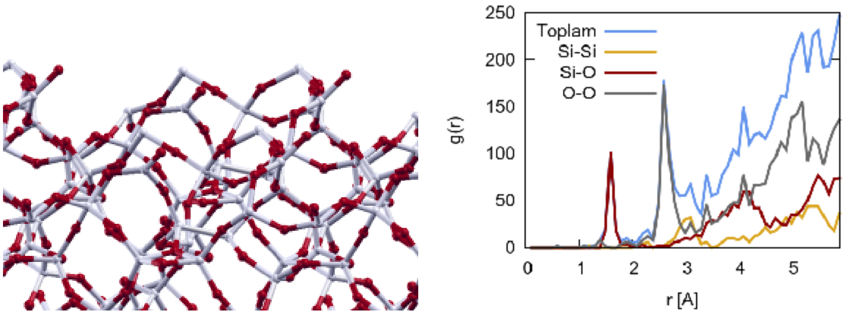

(a) (b)

Figure 5.3: Illustration of the 010 surface of SiO_2. Red spheres refer to O atoms, white ones refer Si.

atom and F atom are +1.00 e and -1.03 e, respectively. The length of the H-O bond is 0.98 Å and the length of the F-Si bond is 1.63 Å . The geometry optimized structure is given in the Figure 5.4.

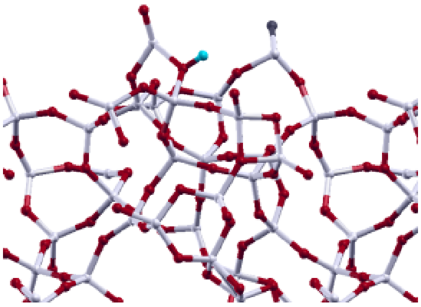

Figure 5.4: Illustration of the H and F ions on 010 surface of SiO_2. Red spheres refer to O atoms, white ones refer Si and blue ones refer H.

The another ion in the etchant solution is Cu therefore the binding energies of the Cu atom on the surface are examined next. There are several sites available on the surface. The, Cu atom is placed on top of the Si atom with coordination number 3 and the binding energies are calculated as -1.93 eV corresponding Bader charge on it found as +0.26 |e|. We consider also adsorption of Cu atom on Si atom with coordination number 2 and the binding energy is found as -1.50 eV. The charge on Cu in this configuration is -0.04 |e|. Finally Cu is placed on top of the O atom which is located between the two Si atoms and the binding energy is obtained as -1.80 eV. The Bader charge value on the Cu atom for this structure is -0.04 |e|. The geometry optimized structures are given in Figure 5.5.

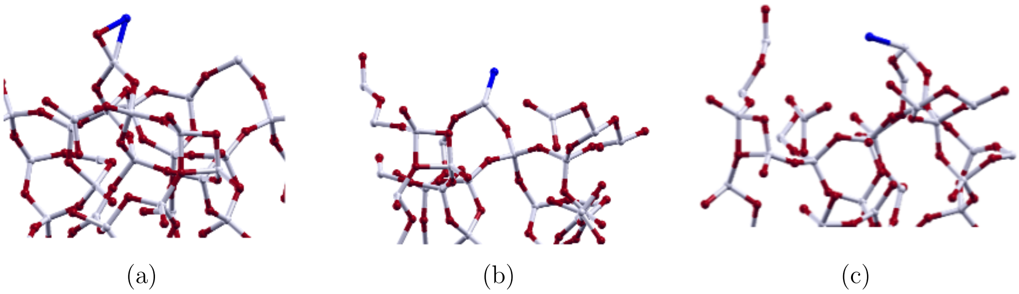
(a) (b) (c)

Figure 5.5: Illustration of the Cu on amorphous surface of SiO_2 (010). (a) represents the Cu atom on Si atom with coordination number 3, (b) represents Cu atom on Si atom with coordination number 2 and (c) represents Cu atom on top of the O atom which is located between the two Si atoms. Red spheres refer to O atoms, white ones refer Si and navy ones refer Cu.

5.4 Interaction of Si(100) Crystal Surface with Etchants

Finally, the interaction of bare surface of the Si(100) crystal and the oxidized Si(100) crystal surface with the same ions of etchant solutions will be investigated in this section. When this structure is subjected to the geometric optimization process, the surface goes to a minimum energy in a different form which is called reconstruction. The bottom two layers are fixed in all surface models to mimic bulk structure. After obtaining the optimized reconstructed surface , the interactions of this surface with the HF etchants are investigated by calculating the binding energies and the Bader charges. Since HF is in solution, it is assumed that H and F are bound to the surface separately as ions. H and F ions are placed different sites on the surface of Si as depicted in the Figure 5.6 and the bonding energies of H and F ions attached to the Si surface are -13.27 eV , -13.44 eV , -13.27 eV , -13.29 eV following the order in this figure. These binding energies, which are quite high, show that the surface strongly interacts with the acid. Bader charges are almost similar for all configurations and the charges on H is -1.03 e, while the load on F is -1.06 e. The approximately equivalent charges on the ions confirm that the almost same binding energies.

The same procedure is repeated to study the interaction between the surface and the Cu ion. Cu ion is placed on the reconstructed Si(100) surface at two different locations to calculate binding energies. The adsorption energies are calculated to be -3.28 eV

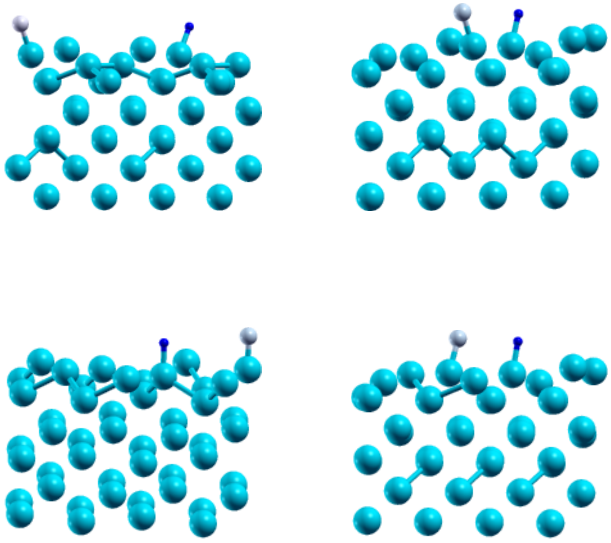

Figure 5.6: llustration of the interaction between the reconstructed Si surfaces with H, and F ions. In this figure, Si atoms are light, blue H atoms are navy and F atoms are grey.

and -3.30 eV as given in the Figure 5.7. The values are very low when compared to that for H and F ions. One can conclude with these results that H and F ions interact more with the surface.

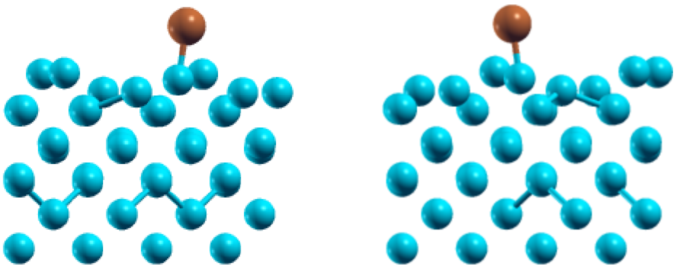

Figure 5.7: Illustration of the interaction between the reconstructed Si surfaces with Cu atoms. In this figure, Si atoms are light and blue Cu atoms are brown.

5.5 Interaction of Oxygenated Si(100) Crystal Surface with Etchants

During the experimental process, the Si surfaces are oxidized; therefore, the same calculations are repeated on the oxygenated Si(100) surface. Oxidized surfaces are obtained by bonding as many O atoms as half of the number of the atoms at top layer. The interaction of the oxidized surfaces with the H and F ions is examined by calculating the binding energies. The adsorption energies are corresponding the configurations given in the Figure 5.8 -9.35 eV, -13.67 eV, and -13.65 eV. The binding energy of the Cu atom on the oxidized surface is -5.03 eV which is higher than the value obtained for the case of non-oxidized surface. During the geometry optimization Cu atom, which is initially placed at top of the O atom, migrates between two O atoms forming bond with them given in the Figure 5.8.

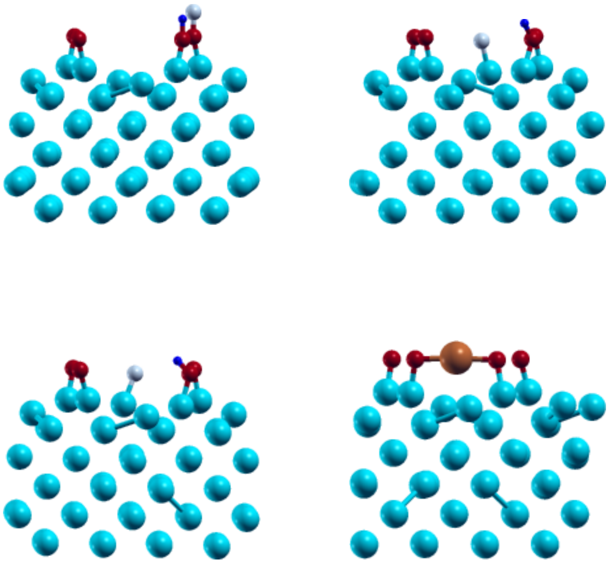

Figure 5.8: Illustration of the interaction between the reconstructed oxidized Si surfaces with H and F ions, Cu atoms. In this figure, Si atoms are light and blue Cu atoms are brown.

5.6 Conclusion

In general, with the help of the adsorption energy results, the interaction between ions and amorphous surface are weaker than the reconstructed bare and oxydized Si surfaces. The adsorption energies are quite high for H and F ions on the reconstructed Si(100) surface. When the presence of the O atoms on the surface, the adsorption energy values are not improved. However, for Cu ions the adsorption energy is improved with precovered O atom on the Si surface. However, Cu ions etch the surface more when compared to H and F ions which shows that Cu interacts with the surface more according to experimental results. Therefore, it is not possible to reach a concrete conclusion by focusing only the adsorption energies of the etchants with the surface. Additionally, the activation energies for the etchant process should be calculated for a better understanding.

CHAPTER 6

CONCLUSION

In the present thesis three different topics are investigated in detail by using the DFT. First, we explored the surface chemistry of the Mo_2C in the absence and presence of the promoters in order to examine the WGS reaction in Chapter 3. Then ,the effect of the Pt as dopants on CH_3OH dehydrogenation on the gold surfaces was examined in Chapter 4. Finally, the interaction between different kinds of slabs which are amorphous silica, crystal Si(100) and oxygenated Si(100) and the H,F ions and Cu ions was studied in Chapter 5.

In Chapter 3, the adsorption energies of the molecules and atoms involved in the WGS reaction were examined on Mo1, Mo2 and C terminated slabs. Subsequently, the adsorption of CO molecule with preadsorbed Pt, Au, and K atoms was studied. The coadsorption energies with K atom as an alkali promoter were much larger than the values obtained for Pt and Au atoms. Finally, activation barrier of the CO dissociation was investigated in order to see the effects of the promoter on the reaction. This reaction was only considered on Mo1 type of termination due to the fact that it yields much larger coadsorption energies when compared to Mo2 and C termination.

The activation barrier was calculated first on unpromoted Mo1 termination by NEB method, and the value was found as -2.01 eV. The same calculation was repeated on the Pt promoted Mo1 terminated slab. The dissociation energy is 1.74 eV, which is smaller than the value obtained for the bare case. This decrease in the barrier indicates that Pt as promoter enhances the dissociation of CO molecule. In order to examine how Pt atom decrease the reaction barrier, PDOS analysis was first performed for the transition state. According to the Figure 3.11, the hibridization between the d states of the Pt atom and Mo atoms weakens the bonding of CO molecule and Mo terminated surface, which is attributed to the decrease in the activation barrier. Additionally, the CO molecule on the unpromoted surfaces has a total charge of -2.10 |e| during the dissociation. The electronic charge of this molecule decreases on Pt promoted surfaces, which also favors the dissociation barrier. The activation energy was calculated for K promoted surfaces and the value was found as 1.57 eV, which is even lower than the value for Pt promoted surfaces. There was not strong hybridization between the promoter and surface atoms; therefore, hybridization was not the reason for the lower value in the activation barrier according to Figure 3.12. This result is attributed to the better stabilization of the transition state of reaction with K as promoter when compared to the others given in the Figure 3.12. The activation energy was calculated for Au promoted surface and the value was found as 2.07 eV, which was even larger than the value obtained for the unpromoted surface. As a result, the precence of K atom as an alkali promoter enhances the the dissociative CO adsorption.

As was stated in the introduction part of the Chapter 4, the presence of the atomic O on the gold surfaces reduces the activation barrier of the CH_3OH dissociation. However, it is difficult to obtain atomic O on the gold surfaces and by products formed during this process are extremely harmful for the environment. Therefore; in Chapter 4, the potential promoting effect of Pt atom as dopants was studied for different concentrations on the gold surfaces, which is on the reaction barrier of CH_3OH dissociation, without using O atom. With this aim, the adsorption energies of the atoms and molecules involving the dissociation process were calculated on the bare and doped surfaces in order to define their stable sites. According to the adsorption energy results, the methanol molecule is weakly bound the bare surface. Different concentrations of Pt atom as dopant on the surfaces almost never changes the adsorption energies of the this molecule. On the contrary, the CH_3OH molecule is more strongly bound to the surface. The Pt doped surfaces do not change binding energies of the CH_3O molecule significantly. The adsorption energy of H atom were greater than both CH_3OH and CH_3O molecules. A substantial increase was observed for the adsorption energies of the O atom on the surface of Au/Pt, Au/2Pt, and Au/3Pt. On the contrary, the binding energies are not improved on the Au/9Pt surface. Finally OH molecule adsorption was examined on bare and doped surfaces and Pt atom does not significantly affect the adsorption energies of this molecule. The general result for the molecules and atoms on Au/sub slab is that the adsorption energies do not dramatically change with respect to the clean surface. Additionally, the coadsorption energies of the CH_3OH with O, CH_3O with H and CH_3O with OH were calculated in order for examining how these molecules and atoms change their adsorption energies.

After obtaining everything related to the adsorption process, the activation barriers were computed for the dissociation of CH_3OH molecule by NEB method. It was observed that the activation barrier decreases when the Pt atom is introduced as dopant on the surfaces. The minimum activation energy was obtained on the Au/9Pt slab with the value of 0.79 eV. In order to check the results, the CH_3OH decomposition was considered also on O precovered gold surfaces. The activation barriers were found less than the case on the clean Au and doped surfaces. When activation barriers corresponding to doped and precovered surfaces are compared, Au/9Pt type of slab yields a larger value, but it is much lower than the value obtained in the clean surface. The general result is that Au/9Pt decoration can be used in order to decrease the activation barrier of the CH_3OH decomposition through the O-H bond scission instaed of using O atom on the surfaces.

In Chapter 5, the interaction between different kinds of slabs, which are amorphous silica, crystal Si(100) and oxygenated Si(100), and the etchant solution, which was used in experimental part of this study, were examined by calculating the binding energies of etchant ingredients on slabs. The etchant solution includes HF and Cu ions; therefore, the interaction between amorphous SiO_2 surface with HF and Cu ion were analyzed first. HF and Cu ions were placed various sites on the slab by considering different coordination number of Si atoms. The adsorption energy of the HF ions was found as -1.35 eV, while the adsorption energy values for Cu ions are between -1.50 eV and -1.93 eV. With these results, one can conclude that Cu ion interacts more strongly than HF ions. The other phase of Si based surfaces detected in the experimental procedure were crystal Si and oxygenated crystal Si surfaces. Therefore, the interaction between the etchant ions and these type of slabs were studied. H and F ions were placed different sites on the reconstructed Si(100) surface and the adsorption energy values were varied from -13.27 eV to -13.44 eV. These values are quite high, indicating that there is a strong interaction between slabs and ions. The same procedure was repeated for adsorption energies of Cu ions on the same slab.

The adsorption energies were calculated to be -3.28 eV and -3.30 eV, which are quite low relative to the H and F ions. Finally, all of the same calculations were carried out on oxygenated Si (100) surfaces. The adsorption energies for H and F ions were found as -9.35 eV, -13.65 eV and -13.67 eV, while for Cu ion on oxygenated surface it was found as -5.30 eV. Again it is observed that H and F ions strongly interact with the oxygenated slabs when compared to the Cu ion. However, Cu ions etch the surface more when compared to H and F ions, which shows that Cu interacts with the surface more according to experimental results. Therefore, it is not possible to reach a concrete conclusion by focusing only the adsorption energies of the etchants with the surface. Additionally, the activation energies for the etchant process should be calculated for a better understanding.

REFERENCES

[1] Jose A Rodriguez, Jaime Evans, Jesús Graciani, Joon-Bum Park, Ping Liu, Jan Hrbek, and Javier Fdez Sanz. High water- gas shift activity in tio2 (110) supported cu and au nanoparticles: Role of the oxide and metal particle size. *The Journal of Physical Chemistry C*, 113(17):7364–7370, 2009.

[2] Joon B Park, Jesus Graciani, Jaime Evans, Dario Stacchiola, Sanjaya D Senanayake, Laura Barrio, Ping Liu, Javier Fdez Sanz, Jan Hrbek, and José A Rodriguez. Gold, copper, and platinum nanoparticles dispersed on ceo x/-tio2 (110) surfaces: High water-gas shift activity and the nature of the mixed-metal oxide at the nanometer level. *Journal of the American Chemical Society*, 132(1):356–363, 2009.

[3] Mayank Shekhar, Jun Wang, Wen-Sheng Lee, W Damion Williams, Seung Min Kim, Eric A Stach, Jeffrey T Miller, W Nicholas Delgass, and Fabio H Ribeiro. Size and support effects for the water–gas shift catalysis over gold nanoparticles supported on model al2o3 and tio2. *Journal of the American Chemical Society*, 134(10):4700–4708, 2012.

[4] Junji Nakamura, Joseph M Campbell, and Charles T Campbell. Kinetics and mechanism of the water-gas shift reaction catalysed by the clean and cs-promoted cu (110) surface: A comparison with cu (111). *J. Chem. Soc., Faraday Trans.*, 86(15):2725–2734, 1990.

[5] Paraskevi Panagiotopoulou and Dimitris I Kondarides. Effects of alkali promotion of tio 2 on the chemisorptive properties and water–gas shift activity of supported noble metal catalysts. *Journal of Catalysis*, 267(1):57–66, 2009.

[6] Ching-Shiun Chen, Wu-Hsun Cheng, and Shou-Shiun Lin. Study of reverse water gas shift reaction by tpd, tpr and co 2 hydrogenation over potassium-promoted cu/sio 2 catalyst. *Applied Catalysis A: General*, 238(1):55–67, 2003.

[7] Frank M Gottschalk and Graham J Hutchings. Cobalt manganese oxide: a novel high activity water gas shift catalyst. *Journal of the Chemical Society, Chemical Communications*, (2):123–124, 1988.

[8] RB Levy and M Boudart. Platinum-like behavior of tungsten carbide in surface catalysis. *science*, 181(4099):547–549, 1973.

[9] J_J Liao, RC Wilcox, and RH Zee. Structures and properties of the mo mo 2 c system. *Scripta Metallurgica et Materialia*, 24(9):1647–1652, 1990.

[10] Henry H Hwu and Jingguang G Chen. Surface chemistry of transition metal carbides. *Chemical reviews*, 105(1):185–212, 2005.

[11] Jennifer A Nelson and Michael J Wagner. High surface area nanoparticulate transition metal carbides prepared by alkalide reduction. *Chemistry of materials*, 14(10):4460–4463, 2002.

[12] Jeremy Patt, Dong Ju Moon, Cory Phillips, and Levi Thompson. Molybdenum carbide catalysts for water–gas shift. *Catalysis Letters*, 65(4):193–195, 2000.

[13] Dong Ju Moon and Jong Woo Ryu. Molybdenum carbide water–gas shift catalyst for fuel cell-powered vehicles applications. *Catalysis letters*, 92(1-2):17–24, 2004.

[14] Max Born and Robert Oppenheimer. Zur quantentheorie der molekeln. *Annalen der Physik*, 389(20):457–484, 1927.

[15] Douglas R Hartree. The wave mechanics of an atom with a non-coulomb central field. part i. theory and methods. In *Mathematical Proceedings of the Cambridge Philosophical Society*, volume 24, pages 89–110. Cambridge University Press, 1928.

[16] Vladimir Fock. Näherungsmethode zur lösung des quantenmechanischen mehrkörperproblems. *Zeitschrift für Physik A Hadrons and Nuclei*, 61(1):126–148, 1930.

[17] John C Slater. Note on hartree's method. *Physical Review*, 35(2):210, 1930.

[18] Llewellyn H Thomas. The calculation of atomic fields. In *Mathematical Proceedings of the Cambridge Philosophical Society*, volume 23, pages 542–548. Cambridge University Press, 1927.

[19] Enrico Fermi. Eine statistische methode zur bestimmung einiger eigenschaften des atoms und ihre anwendung auf die theorie des periodischen systems der elemente. *Zeitschrift für Physik*, 48(1-2):73–79, 1928.

[20] Pierre Hohenberg and Walter Kohn. Inhomogeneous electron gas. *Physical review*, 136(3B):B864, 1964.

[21] Walter Kohn and Lu Jeu Sham. Self-consistent equations including exchange and correlation effects. *Physical review*, 140(4A):A1133, 1965.

[22] David M Ceperley and BJ Alder. Ground state of the electron gas by a stochastic method. *Physical Review Letters*, 45(7):566, 1980.

[23] John P Perdew and Yue Wang. Accurate and simple analytic representation of the electron-gas correlation energy. *Physical Review B*, 45(23):13244, 1992.

[24] Charles Kittel. *Introduction to solid state physics*. Wiley, 2005.

[25] Bo Li, Eckehard Schöll, and Matthias Scheffler. *Density-functional theory and quantum chemistry studies on" dry" and" wet" NaCl (001)*. PhD thesis, Technische Universität Berlin, 2008.

[26] Hendrik J Monkhorst and James D Pack. Special points for brillouin-zone integrations. *Physical review B*, 13(12):5188, 1976.

[27] Peter E Blöchl, Ove Jepsen, and Ole Krogh Andersen. Improved tetrahedron method for brillouin-zone integrations. *Physical Review B*, 49(23):16223, 1994.

[28] Si Zhou. *Density functional theory study of oxidized epitaxial graphene*. PhD thesis, Georgia Institute of Technology, 2014.

[29] Graeme Henkelman and Hannes Jónsson. Improved tangent estimate in the nudged elastic band method for finding minimum energy paths and saddle points. *The Journal of chemical physics*, 113(22):9978–9985, 2000.

[30] Graeme Henkelman, Blas P Uberuaga, and Hannes Jónsson. A climbing image nudged elastic band method for finding saddle points and minimum energy paths. *The Journal of chemical physics*, 113(22):9901–9904, 2000.

[31] MV Twigg. *Catalyst Handbook, 1989*. 1989.

[32] Michael Estrella, Laura Barrio, Gong Zhou, Xianqin Wang, Qi Wang, Wen Wen, Jonathan C Hanson, Anatoly I Frenkel, and José A Rodriguez. In situ characterization of cufe2o4 and cu/fe3o4 water- gas shift catalysts. *The Journal of Physical Chemistry C*, 113(32):14411–14417, 2009.

[33] MS Spencer. The role of zinc oxide in cu/zno catalysts for methanol synthesis and the water–gas shift reaction. *Topics in Catalysis*, 8(3-4):259–266, 1999.

[34] Amit A Gokhale, James A Dumesic, and Manos Mavrikakis. On the mechanism of low-temperature water gas shift reaction on copper. *Journal of the American Chemical Society*, 130(4):1402–1414, 2008.

[35] NA Koryabkina, AA Phatak, WF Ruettinger, RJ Farrauto, and FH Ribeiro. Determination of kinetic parameters for the water–gas shift reaction on copper catalysts under realistic conditions for fuel cell applications. *Journal of Catalysis*, 217(1):233–239, 2003.

[36] Yue Li, Qi Fu, and Maria Flytzani-Stephanopoulos. Low-temperature water-gas shift reaction over cu-and ni-loaded cerium oxide catalysts. *Applied Catalysis B: Environmental*, 27(3):179–191, 2000.

[37] Takafumi Shido and Yasuhiro Iwasawa. Regulation of reaction intermediate by reactant in the water-gas shift reaction on ceo 2, in relation to reactant-promoted mechanism. *Journal of catalysis*, 136(2):493–503, 1992.

[38] Viviane Schwartz, Victor Teixeira da Silva, and S Ted Oyama. Push–pull mechanism of hydrodenitrogenation over carbide and sulfide catalysts. *Journal of Molecular Catalysis A: Chemical*, 163(1):251–268, 2000.

[39] S Ted Oyama, C Charles Yu, and S Ramanathan. Transition metal bimetallic oxycarbides: synthesis, characterization, and activity studies. *Journal of Catalysis*, 184(2):535–549, 1999.

[40] Ki Yeop Park, Won Kyu Seo, and Jae Sung Lee. Selective synthesis of light olefins from syngas over potassium-promoted molybdenum carbide catalysts. *Catalysis letters*, 11(3-6):349–356, 1991.

[41] Xue-Rong Shi, Jianguo Wang, and Klaus Hermann. Co and no adsorption and dissociation at the b-mo2c (0001) surface: A density functional theory study. *The Journal of Physical Chemistry C*, 114(32):13630–13641, 2010.

[42] Jun Ren, Chun-Fang Huo, Jianguo Wang, Yong-Wang Li, and Haijun Jiao. Surface structure and energetics of oxygen and co adsorption on α-mo 2 c (0001). *Surface science*, 596(1):212–221, 2005.

[43] Carolina Pistonesi, María Estela Pronsato, László Bugyi, and A Juan. The adsorption of co on potassium doped molybdenum carbide surface: An ab-initio study. *Catalysis today*, 181(1):102–107, 2012.

[44] Hiroyuki Tominaga and Masatoshi Nagai. Density functional theory of water-gas shift reaction on molybdenum carbide. *The Journal of Physical Chemistry B*, 109(43):20415–20423, 2005.

[45] Tao Wang, Yong-Wang Li, Jianguo Wang, Matthias Beller, and Haijun Jiao. High coverage co adsorption and dissociation on the orthorhombic mo2c (100) surface. *The Journal of Physical Chemistry C*, 118(6):3162–3171, 2014.

[46] Tao Wang, Xinxin Tian, Yong Yang, Yong-Wang Li, Jianguo Wang, Matthias Beller, and Haijun Jiao. Coverage dependent adsorption and co-adsorption of co and h 2 on the cdi 2-antitype metallic mo 2 c (001) surface. *Physical Chemistry Chemical Physics*, 17(3):1907–1917, 2015.

[47] Paolo Giannozzi, Stefano Baroni, Nicola Bonini, Matteo Calandra, Roberto Car, Carlo Cavazzoni, Davide Ceresoli, Guido L Chiarotti, Matteo Cococcioni, Ismaila Dabo, Andrea Dal Corso, Stefano de Gironcoli, Stefano Fabris, Guido Fratesi, Ralph Gebauer, Uwe Gerstmann, Christos Gougoussis, Anton Kokalj, Michele Lazzeri, Layla Martin-Samos, Nicola Marzari, Francesco Mauri, Riccardo Mazzarello, Stefano Paolini, Alfredo Pasquarello, Lorenzo Paulatto, Carlo Sbraccia, Sandro Scandolo, Gabriele Sclauzero, Ari P Seitsonen, Alexander Smogunov, Paolo Umari, and Renata M Wentzcovitch. Quantum espresso: a modular and open-source software project for quantum simulations of materials. *Journal of Physics: Condensed Matter*, 21(39):395502, 2009.

[48] Anton Kokalj. Computer graphics and graphical user interfaces as tools in simulations of matter at the atomic scale. *Computational Materials Science*, 28(2):155–168, 2003.

[49] Jmol: an open-source java viewer for chemical structures in 3d.

[50] RFW Bader. Atoms in molecules oxford science publications oxford, 1990.

[51] Edward Sanville, Steven D Kenny, Roger Smith, and Graeme Henkelman. Improved grid-based algorithm for bader charge allocation. *Journal of computational chemistry*, 28(5):899–908, 2007.

[52] C Pistonesi, A Juan, AP Farkas, and F Solymosi. Effects of potassium on the adsorption of methanol on β-mo 2 c (001) surface. *Surface Science*, 604(11):914–919, 2010.

[53] T Epicier, J Dubois, C Esnouf, G Fantozzi, and P Convert. Neutron powder diffraction studies of transition metal hemicarbides m 2 c 1- x—ii. in situ high temperature study on w 2 c 1- x and mo 2 c 1- x. *Acta Metallurgica*, 36(8):1903–1921, 1988.

[54] Jeong Woo Han, Liwei Li, and David S Sholl. Density functional theory study of h and co adsorption on alkali-promoted mo2c surfaces. *The Journal of Physical Chemistry C*, 115(14):6870–6876, 2011.

[55] Jeong Woo Han, Liwei Li, and David S Sholl. Density functional theory study of h and co adsorption on alkali-promoted mo2c surfaces. *The Journal of Physical Chemistry C*, 115(14):6870–6876, 2011.

[56] ME Pronsato, C Pistonesi, A Juan, AP Farkas, L Bugyi, and F Solymosi. Density functional theory study of methyl iodide adsorption and dissociation on clean and k-promoted β-mo2c surfaces. *The Journal of Physical Chemistry C*, 115(6):2798–2804, 2011.

[57] Tao Wang, Xingwu Liu, Shengguang Wang, Chunfang Huo, Yong-Wang Li, Jianguo Wang, and Haijun Jiao. Stability of β-mo2c facets from ab initio atomistic thermodynamics. *The Journal of Physical Chemistry C*, 115(45):22360–22368, 2011.

[58] Hiroyuki Tominaga, Yusuke Aoki, and Masatoshi Nagai. Hydrogenation of co on molybdenum and cobalt molybdenum carbides. *Applied Catalysis A: General*, 423-424:192–204, 2012.

[59] Tao Wang, Xinxin Tian, Yong Yang, Yong-Wang Li, Jianguo Wang, Matthias Beller, and Haijun Jiao. Coverage dependent adsorption and co-adsorption of co and h2 on the cdi2-antitype metallic mo2c(001) surface. *Physical Chemistry Chemical Physics*, 17:1907–1917, 2015.

[60] E Rudy, St Windisch, AJ Stosick, and J Ro Hoffman. Constitution of binary molybdenum–carbon alloys. Technical report, Aerojet-General Corp., Sacramento, Calif., 1967.

[61] CJ Zhang and P Hu. A first principles study of methanol decomposition on pd (111): mechanisms for o–h bond scission and c–o bond scission. *The Journal of Chemical Physics*, 115(15):7182–7186, 2001.

[62] Ming Li, Wenyue Guo, Ruibin Jiang, Lianming Zhao, and Honghong Shan. Decomposition of ethanol on pd (111): a density functional theory study. *Langmuir*, 26(3):1879–1888, 2009.

[63] Cui-Yu Niu, Jiao Jiao, Bin Xing, Gui-Chang Wang, and Xian-He Bu. Reaction mechanism of methanol decomposition on pt-based model catalysts: A theoretical study. *Journal of computational chemistry*, 31(10):2023–2037, 2010.

[64] Jeff Greeley and Manos Mavrikakis. A first-principles study of methanol decomposition on pt (111). *Journal of the American Chemical Society*, 124(24):7193–7201, 2002.

[65] Sanket K Desai, Matthew Neurock, and K Kourtakis. A periodic density functional theory study of the dehydrogenation of methanol over pt (111). *The Journal of Physical Chemistry B*, 106(10):2559–2568, 2002.

[66] Masatake Haruta, Tetsuhiko Kobayashi, Hiroshi Sano, and Nobumasa Yamada. Novel gold catalysts for the oxidation of carbon monoxide at a temperature far below 0 c. *Chemistry Letters*, 16(2):405–408, 1987.

[67] Qi Fu, Adam Weber, and Maria Flytzani-Stephanopoulos. Nanostructured au–ceo2 catalysts for low-temperature water–gas shift. *Catalysis Letters*, 77(1):87–95, 2001.

[68] Silvio Carrettin, Paul McMorn, Peter Johnston, Ken Griffin, Christopher J Kiely, and Graham J Hutchings. Oxidation of glycerol using supported pt, pd and au catalysts. *Physical Chemistry Chemical Physics*, 5(6):1329–1336, 2003.

[69] Alberto Abad, Patricia Concepción, Avelino Corma, and Hermenegildo García. A collaborative effect between gold and a support induces the selective oxidation of alcohols. *Angewandte Chemie International Edition*, 44(26):4066–4069, 2005.

[70] Alberto Abad, Avelino Corma, and Hermenegildo García. Catalyst parameters determining activity and selectivity of supported gold nanoparticles for the aerobic oxidation of alcohols: The molecular reaction mechanism. *Chemistry-a European Journal*, 14(1):212–222, 2008.

[71] Mathew D Hughes, Yi-Jun Xu, Patrick Jenkins, Paul McMorn, Philip Landon, Dan I Enache, Albert F Carley, Gary A Attard, Graham J Hutchings, Frank King, et al. Tunable gold catalysts for selective hydrocarbon oxidation under mild conditions. *Nature*, 437(7062):1132–1135, 2005.

[72] Mark A Lazaga, David T Wickham, Deborah H Parker, George N Kastanas, and Bruce E Koel. Reactivity of oxygen adatoms on the au (111) surface. ACS Publications, 1993.

[73] Hans G Jenniskens, Paul WF Dorlandt, Malcolm F Kadodwala, and Aart W Kleyn. The adsorption of methanol on ag (111) studied with tds and xps. *Surface science*, 357:624–628, 1996.

[74] JN Russell Jr, S M_ Gates, and JT Yates Jr. Reaction of methanol with cu (111) and cu (111)+ o (ads). *Surface science*, 163(2-3):516–540, 1985.

[75] Duane A Outka and Robert J Madix. Broensted basicity of atomic oxygen on the gold (110) surface: reactions with methanol, acetylene, water, and ethylene. *Journal of the American Chemical Society*, 109(6):1708–1714, 1987.

[76] Ch Ammon, A Bayer, G Held, B Richter, Th Schmidt, and H-P Steinrück. Dissociation and oxidation of methanol on cu (1 1 0). *Surface science*, 507:845–850, 2002.

[77] AK Chen and Rich Masel. Direct conversion of methanol to formaldehyde in the absence of oxygen on cu (210). *Surface Science*, 343(1-2):17–23, 1995.

[78] L Zhou, S Günther, D Moszynski, and R Imbihl. Reactivity of oxidized copper surfaces in methanol oxidation. *Journal of catalysis*, 235(2):359–367, 2005.

[79] Bhushan N Zope, David D Hibbitts, Matthew Neurock, and Robert J Davis. Reactivity of the gold/water interface during selective oxidation catalysis. *Science*, 330(6000):74–78, 2010.

[80] Bingjun Xu, Xiaoying Liu, Jan Haubrich, Robert J Madix, and Cynthia M Friend. Selectivity control in gold-mediated esterification of methanol. *Angewandte Chemie International Edition*, 48(23):4206–4209, 2009.

[81] Angelo Bongiorno and Uzi Landman. Water-enhanced catalysis of co oxidation on free and supported gold nanoclusters. *Physical review letters*, 95(10):106102, 2005.

[82] Serena Biella and Michele Rossi. Gas phase oxidation of alcohols to aldehydes or ketones catalysed by supported gold. *Chemical communications*, (3):378–379, 2003.

[83] Wen-Kai Chen, Shu-Hong Liu, Mei-Juan Cao, Qian-Gu Yan, and Chun-Hai Lu. Adsorption and dissociation of methanol on au (1 1 1) surface: A first-principles periodic density functional study. *Journal of Molecular Structure: THEOCHEM*, 770(1):87–91, 2006.

[84] Lei Wang, Chaozheng He, Wenhua Zhang, Zhenyu Li, and Jinlong Yang. Methanol-selective oxidation pathways on au surfaces: A first-principles study. *The Journal of Physical Chemistry C*, 118(31):17511–17520, 2014.

[85] A Hussain and SH Shah. Mment> computational study of complete methanol dehydrogenation on au (100) and au (310) surfaces: Dominant role of atomic oxygen. *Surface Science*, 620:30–37, 2014.

[86] Charles Kittel, Paul McEuen, and Paul McEuen. *Introduction to solid state physics*, volume 8. Wiley New York, 1996.

[87] Shuping Liu, Peng Jin, Donghui Zhang, Ce Hao, and Xueming Yang. Reaction mechanism for methanol oxidation on au (111): A density functional theory study. *Applied Surface Science*, 265:443–451, 2013.

[88] J Britt and C Ferekides. Thin-film cds/cdte solar cell with 15.8% efficiency. *Applied Physics Letters*, 62(22):2851–2852, 1993.

[89] Anne Simon Moffat. New solar cells seem to have power at the right price. *Science*, 272:21, 1996.

[90] Arvind Shah, Pedro Torres, Reto Tscharner, Nicolas Wyrsch, and Herbert Keppner. Photovoltaic technology: the case for thin-film solar cells. *science*, 285(5428):692–698, 1999.

[91] Miguel A Contreras, Brian Egaas, K Ramanathan, J Hiltner, A Swartzlander, F Hasoon, and Rommel Noufi. Progress toward 20% efficiency in cu (in, ga) se2 polycrystalline thin-film solar cells. *Progress in Photovoltaics: Research and applications*, 7(4):311–316, 1999.

[92] Martin A Green. Improved estimates for te and se availability from cu anode slimes and recent price trends. *Progress in photovoltaics: research and applications*, 14(8):743–751, 2006.

[93] XY Lee, Mark Goertemiller, Misha Boroditsky, Regina Ragan, and Eli Yablonovitch. Thin film gaas solar cells on glass substrates by epitaxial liftoff. In *AIP Conference Proceedings*, volume 394, pages 719–727. AIP, 1997.

[94] GJ Bauhuis, P Mulder, EJ Haverkamp, JCCM Huijben, and JJ Schermer. 26.1% thin-film gaas solar cell using epitaxial lift-off. *Solar Energy Materials and Solar Cells*, 93(9):1488–1491, 2009.

[95] F Henley, A Brailove, A Lamm, T Heerwagen, E Sauar, M Nese, R Steeman, and B Hammel. Kerf-free silicon wafering equipment configurations using beam-induced cleave technology. In *23 European Photovoltaic Solar Energy Conference*, 2008.

[96] Frederic Dross, Aurelien Milhe, Jo Robbelein, Ivan Gordon, Pierre-Olivier Bouchard, Guy Beaucarne, and Jef Poortmans. Stress-induced lift-off method for kerf-loss-free wafering of ultra-thin (50 μm) crystalline si wafers. In *Photovoltaic Specialists Conference, 2008. PVSC'08. 33rd IEEE*, pages 1–5. IEEE, 2008.

[97] George A Lager, JD Jorgensen, and FJ Rotella. Crystal structure and thermal expansion of α-quartz sio2 at low temperatures. *Journal of Applied Physics*, 53(10):6751–6756, 1982.

[98] JJ Pluth, JV Smith, and J Faber Jr. Crystal structure of low cristobalite at 10, 293, and 473 k: Variation of framework geometry with temperature. *Journal of Applied Physics*, 57(4):1045–1049, 1985.

[99] AF Wright and MS Lehmann. The structure of quartz at 25 and 590 c determined by neutron diffraction. *Journal of solid state chemistry*, 36(3):371–380, 1981.

[100] Kuniaki Kihara, Takeo Matsumoto, and Moritaka Imamura. Structural change of orthorhombic-i tridymite with temperature: A study based on second-order thermal-vibrational parameters. *Zeitschrift für Kristallographie-Crystalline Materials*, 177(1-4):27–38, 1986.

[101] RWG Wyckoff. Crystal structures; re krieger pub. *Co.: Malabar, FL*, 2:362, 1982.

[102] RC Chittick, JH Alexander, and HF Sterling. The preparation and properties of amorphous silicon. *Journal of the Electrochemical Society*, 116(1):77–81, 1969.

[103] Evgueni Chagarov, James B Adams, and John Kieffer. Application of design of experiments methodology to optimization of classical molecular dynamics generation of amorphous sio2 structure. *Modelling and Simulation in Materials Science and Engineering*, 12(2):337, 2004.

[104] Alexandra Roder, Walter Kob, and Kurt Binder. Structure and dynamics of amorphous silica surfaces. *The Journal of Chemical Physics*, 114(17):7602–7614, 2001.

[105] Sébastien Le Roux and Valeri Petkov. Isaacs–interactive structure analysis of amorphous and crystalline systems. *Journal of Applied Crystallography*, 43(1):181–185, 2010.

[106] Robert J Bondi, Sangheon Lee, and Gyeong S Hwang. First-principles study of the mechanical and optical properties of amorphous hydrogenated silicon and silicon-rich silicon oxide. *Physical Review B*, 81(19):195207, 2010.

CURRICULUM VITAE

PERSONAL INFORMATION

Surname, Name: Merve Demirtaş
Nationality: Turkish (TC)
Email: mrvdmrtas@gmail.com, merved@metu.edu.tr

EMPLOYMENT

2010-2018 Teaching Assistant, Department of Physics, Middle East Technical University, TURKEY

COMPUTER SKILLS

Octave programing Language for numerical computations
Quantum Espresso For calculations of electronic structure and material modelling
Xcrysden, Vesta and Jmol For visualization of crystal structures

PUBLICATIONS

1 "Effect of Platinum, Gold, and Potassium Additives on the Surface Chemistry of CdI_2-Antitype Mo_2C ", M. Demirtas, H. Ustunel, D. Toffoli, ACS Omega 2.11 (2017): 7976-7984.

2 "Instability of Non-crystalline NaO_2 film in Na-O_2 Batteries: the Controversial Effect of RuO_2 Catalyst", M. F. Tovini, M. Hong, J. Park, M. Demirtas, D. Toffoli, H. Ustunel, H. R. Byon, E. Yılmaz, The Journal of Physical Chemistry C (2018).

3 "Methanol dehydrogenation reaction through the O-H bond breaking on Au(111) surface with Pt atom doping", M. Demirtas, H. Ustunel, D. Toffoli, (**to be submitted soon**)

ORAL PRESENTATIONS

Nano-TR, Ankara, Turkey, 2015 Performance of a Mo_2C as a catalyst for the Water-Gas Shift Reaction: A Density Functional Theory Study